

Control and manipulation of nanoparticles for fabrication of metal matrix composites

by

Mina Bastwros

A dissertation submitted to the graduate faculty
in partial fulfillment of the requirements for the degree of

DOCTOR OF PHILOSOPHY

Major: Mechanical Engineering

Program of Study Committee:
Gap-Yong Kim, Major Professor

Ganesh Balasubramanian

Wei Hong

Alan Russell

Pranav Shrotriya

The student author and the program of study committee are solely responsible for the content of this dissertation . The Graduate College will ensure this dissertation is globally accessible and will not permit alterations after degree conferred.

Iowa State University

Ames, Iowa

2017

Copyright © Mina Bastwros, 2017. All rights reserved.

DEDICATION

This dissertation is dedicated to my parents,
Mr. Mikhail Bastwros and Mrs. Marina Charobime
For their invaluable support and encouragement,

And

my loving wife,

Sarah Wahba,

my precious son and daughter, Mark and Hannah Bastwros,
for their support, encouragement, and understanding throughout the study

TABLE OF CONTENTS

DEDICATION	ii
LIST OF FIGURES.....	vi
LIST OF TABLES	x
ACKNOWLEDGEMENTS.....	xi
ABSTRACT	xii
CHAPTER 1 INTRODUCTION.....	1
1.1 Motivation	1
1.2 Research framework and objectives.....	4
1.2.1 Effect of ball milling on graphene reinforced Al6061 composite fabricated by semi-solid sintering	4
1.2.2 Ultrasonic spray deposition of sic nanoparticles for laminate metal composite fabrication.....	4
1.2.3 Fabrication of pattern reinforced AZ31 multilayer composite using ultrasonic spray deposition	5
1.2.4 Magnetic field assisted deposition of nanoparticles in pattern structures	5
1.3 Dissertation organization.....	6
CHAPTER 2 EFFECT OF BALL MILLING ON GRAPHENE REINFORCED AL6061 COMPOSITE FABRICATED BY SEMI-SOLID SINTERING	7
2.1 Introduction	7

2.2	Material and methods	8
2.3	Results and discussion.....	11
2.4	Conclusions	23
CHAPTER 3 ULTRASONIC SPRAY DEPOSITION OF SIC NANOPARTICLES FOR LAMINATE METAL COMPOSITE FABRICATION		24
3.1	Introduction	24
3.2	Experimental procedures.....	26
3.3	Results and discussion.....	30
3.4	Conclusions	46
CHAPTER 4 FABRICATION OF PATTERN REINFORCED AZ31 MULTILAYER COMPOSITE USING ULTRASONIC SPRAY DEPOSITION		48
4.1	Introduction	48
4.2	Experimental procedures.....	50
4.3	Results and discussion.....	54
4.3.1	Nanoparticle deposition.....	54
4.3.2	Composite consolidation	61
4.3.3	Reinforcement phase properties	66
4.3.4	Small punch test	69
4.4	Conclusions	70

CHAPTER 5	MAGNETIC FIELD ASSISTED DEPOSITION OF FERROMAGNETIC NANOPARTICLES	72
5.1	Introduction and motivation	72
5.2	Experimental setup	75
5.3	Results and discussions	78
5.4	Conclusions	95
CHAPTER 6	SUMMARY AND CONTRIBUTIONS.....	97
6.1	Summary	97
6.1.1	Effect of ball milling on graphene reinforced Al6061 composite fabricated by semi-solid sintering	97
6.1.2	The ultrasonic spray deposition of sic nanoparticles for laminate metal composite fabrication.....	98
6.1.3	Fabrication of pattern reinforced AZ31 multilayer composite using ultrasonic spray deposition	99
6.1.4	Magnetic field assisted nanoparticle deposition.....	100
6.2	Scientific Contributions.....	101
6.3	Recommendation for future work	102
6.4	Acknowledgement.....	103
APPENDIX A:	SAFE HANDLING OF NANOPARTICLES	104
REFERENCES.....		106

LIST OF FIGURES

Figure 2.1 Experimental setup for semi-solid sintering.....	10
Figure 2.2 TEM image of few-layers graphene	11
Figure 2.3 SEM images of the milled Al6061-1.0 wt.% graphene powder at different milling times: (a, b) milled for 30 min, (c, d) milled for 60 min, (e, f) milled for 90 min.....	12
Figure 2.4 Raman spectra of the milled Al6061-2.0 wt.% graphene powder at different milling times and as-received graphene	13
Figure 2.5 Flexural stress–strain curves of Al6061-1.0 wt.% graphene.....	16
Figure 2.6 XRD analysis of the Al6061-1.0 wt.% graphene samples at different milling times .	18
Figure 2.7 SEM images of fracture surfaces of the Al6061-1.0 wt.% graphene composites prepared at different milling times: (a, b) 10 min, (c, d) 30 min, (e, f) 60 min, and (g, h) 90 min	19
Figure 2.8 SEM images of fracture surfaces: (a) Al6061-1.0 wt.% graphene milled for 90 min, and (b) Al6061 unalloyed milled for 90 min	20
Figure 2.9 SEM images of fracture surface of Al6061-1.0 wt.% graphene composite milled.....	21
Figure 2.10 Images of graphene clusters: (a) BSEC detector SEM image of a graphene cluster embedded in the Al6061 matrix, (b) ETD detector SEM image, (c) BSEC detector SEM image of a graphene cluster attached to the surface, (d) ETD detector SEM imaging, and (e) higher magnification of the graphene layers	22
Figure 3.1 Ultrasonic spray deposition system.....	27
Figure 3.2 (a) Schematic overview of the spraying process and (b) spraying path.....	28
Figure 3.3 The effect of SiC loading and particle size on the surface tension of ethanol-SiC suspension system.....	32
Figure 3.4 (a) Prediction of the atomization droplet size, and (b) prediction of the droplet size from the atomization using different atomization frequencies	33
Figure 3.5 An atomized droplet deposited by a single pass experiment.....	34
Figure 3.6 Effect of flow rate on the deposition structure (a, b) 0.25 ml/min, (c, d) 0.5 ml/min, and (e, f) 1.0 ml/min	36
Figure 3.7 Effect of temperature on the deposition structure, (a, b) 140°C, (c, d) 220°C, and (e, f) 255°C	38

Figure 3.8 Effect of air pressure on the deposition structure, (a, b) 0.5 kPa and (c, d) 1.0 kPa ...	39
Figure 3.9 Effect of SiC loading on the flexural stress – strain curves of Al6061-SiC composites.....	41
Figure 3.10 SEM images of SiC reinforcement layer on the fracture surfaces of (a, c) Al6061-0.3 wt.% SiC composite; (b, d) Al6061-0.6 wt.% SiC composite.....	42
Figure 3.11 SEM images of Al6061 layer on the fracture surfaces of (a) Al6061-0.3 wt.% SiC composite; (b) Al6061-0.6 wt.% SiC composite	43
Figure 3.12 SEM images of reinforcement layer on the fracture surfaces of (a, c) Al6061-0.3 wt.% SiC composite; (b, d) Al6061-0.6 wt.% SiC composite.....	44
Figure 3.13 Flexural stress-strain curves of the consolidated AZ31-SiC composites	45
Figure 4.1 (a) Schematic overview of the spraying process, (b) patterned mask, and (c) spraying path.....	52
Figure 4.2 Small punch test (a) small punch test setup, (b) cross sectional view of the SPT.....	54
Figure 4.3 Effect of flow rate change on the deposition structure with spraying condition at T=190 °C, D=25 mm, and P=0.25 kPa.....	55
Figure 4.4 Effect of temperature change on the deposition structure with spraying condition at Q=0.25 ml/min, D=25 mm, and P=0.25 kPa	56
Figure 4.5 Effect of air pressure change on the deposition structure with spraying condition at T=190 °C, Q=0.25 ml/min, and D=25 mm	57
Figure 4.6 Effect of spraying distance change on the deposition structure with spraying condition at T=190 °C, Q=0.25ml/min, and P=0.25 kPa	58
Figure 4.7 Effect of spraying speed on the deposition structure, (a, b) 1 mm/s, (c, d) 5 mm/s, and (e, f) 10mm/s	59
Figure 4.8 (a) SEM image of AZ31 substrate sprayed with SiC/Al6061 particles, (b) EDS map of Al distribution, (c) EDS map of the Mg distribution, and (d) EDS map of the Si distribution	60
Figure 4.9 Flexural stress-strain curves of the consolidated samples.....	61
Figure 4.10 Patterned composite fracture surface (a, b) SEM image of fracture surface, (c) EDS map of the Mg distribution of SEM image “b”, and (d) EDS map of the Si distribution of SEM image “b”	63

Figure 4.11 Fracture surface (a) higher magnification of the reinforcement phase, (b) EDS map of the Mg distribution, (c) EDS map of the Si distribution, and (d) EDS map of Al distribution.	65
Figure 4.12 SEM image of the reinforcement layer attached to the AZ31 sheet.....	65
Figure 4.13 EDS line scan across the interface between two AZ31 foils, and elemental diffraction intensity along the line scan with respect to the position on the scanned line.....	67
Figure 4.14 AFM images of the surface topography before and after indentation: (a) AZ31 zone before indentation, (b) interface zone before indentation, (c) AZ31 after indentation, and (d) interface after indentation.....	68
Figure 4.15 SPT load – displacement curves.....	70
Figure 5.1 Machined iron disk attached to a magnetic source.....	76
Figure 5.2 Micro-line protrusion on the iron disc: (a) 65 μm , (b) 100 μm , and (c) 200 μm	76
Figure 5.3: laser machined line protrusions on iron disc with linewidth of, (a) 10 μm , (b) 25 μm , (c) 50 μm , (d) 75 μm , and (e) 100 μm	77
Figure 5.4 Fe nanoparticle deposition corresponding to different line protrusion sizes, (a, b, and c) 65 μm , (d, e, and f) 100 μm , and (h, i, and j) 200 μm	79
Figure 5.5 EDS line scan of the deposited Fe particles corresponding to 65 μm protrusion	80
Figure 5.6 Major and total deposition widths of the Fe nanoparticle depositions.....	80
Figure 5.7 Fe+SiC nanoparticle deposition (weight ratio of 1:1) corresponding to protrusion sizes (a) 65 μm , (b) 100 μm , and (c) 200 μm	82
Figure 5.8 Areas between the deposition lines	82
Figure 5.9 Major and total deposition widths of the Fe (25 nm) + SiC (80 nm) nanoparticle (weight ratio 1:1).....	83
Figure 5.10 SEM image of the Fe + SiC deposition corresponding to the 65 μm protrusion and the EDS maps of the Si and Fe elements (R= 1:1).....	84
Figure 5.11 Fe + SiC nanoparticle deposition corresponding to protrusion size 65 μm with different Fe:SiC particle weight ratio, (a) 1:1, (b) 1:5, (C) 1:10, and (d) 1:20	85
Figure 5.12 Major and total deposition widths of the Fe (25 nm) + SiC (80 nm) nanoparticle with different deposition weight ratios	85

Figure 5.13 Areas in between the deposition lines for different R, (a) 1:1, (b) 1:5, (C) 1:10, and (d) 1:20	87
Figure 5.14 SEM image of the Fe + SiC deposition corresponding to the 65 μm protrusion and the EDS maps of the Si and Fe elements of different R, 1:1, 1:5, 1:10, and 1:20	88
Figure 5.15 Fe + SiC nanoparticle deposition (1:1 weight ratio) corresponding to protrusion size 65 μm with different SiC particle sizes, (a, b, c, and d) 80 nm, (e, f, g, and h) 800 nm, and (i, j, k, and l) 5 μm	90
Figure 5.16 areas in between the deposition lines of Fe + SiC (1:1) deposition with different SiC particle sizes, (a) 800 nm and (b) 5 μm	90
Figure 5.17 The effect of SiC particle size on the van der Waals force	91
Figure 5.18 SEM image of SiC (5 μm) particle , (a) deposited in between the deposition lines and (b) SiC particle deposited at the periphery of the deposition area	91
Figure 5.19 Major and total deposition widths of the Fe (25 nm) + SiC (80 nm) nanoparticle with different deposition weight ratios	92
Figure 5.20 SEM image of the Fe + SiC deposition corresponding to the 65 μm protrusion and the EDS maps of the Si and Fe elements of different SiC particle sizes, 80 nm, 800 nm, and 5 μm	93
Figure 5.21 Fe + SiC nanoparticle deposition (weight ratio of 1:1) corresponding to protrusion sizes and spacings of (a) 100 μm and (b) 75 μm	94
Figure 5.22 Fe + SiC nanoparticle deposition (weight ratio of 1:1) corresponding to 50 μm protrusion size (a) corresponding deposition line and (b) higher magnification	95

LIST OF TABLES

Table 2.1 Chemical composition of Al6061	9
Table 2.2 Raman data of the milled Al6061-2.0 wt.% graphene particles	13
Table 3.1 Summary of the spraying parameters and their values	29
Table 3.2 Chemical composition of AZ31 alloy.....	30
Table 4.1 Summary of the spraying parameters and their values	51
Table 4.2 Summary of the spraying parameters and their values for composite fabrication.....	53
Table 5.1 Summary of nanoparticle size, suspension concentration, and mixing parameters.....	78
Table 5.2 The number of SiC particles transferred by a single Fe particle for different R	86

ACKNOWLEDGEMENTS

I would like to thank my advisor, Professor Gap-Yong Kim, for his guidance throughout the academic program. This work would not have been possible without his support and encouragements. I also thank Professor Ganesh Balasubramanian, Professor Wei Hong, Professor Alan Russell, and Professor Pranav Shrotriya for their invaluable advices and numerous discussions throughout the study.

I greatly acknowledge the financial support from the sponsor of the research, the Defense Advanced Research Projects Agency and the National Science Foundation.

I am grateful to all my colleagues, Can Zhu, Jie Wang, Adam Witthauer, Saeed Mousa, Miao Liu, Nathan Scheirer, and Nicholas Orlofsky for their help and support throughout the program. Finally, I would like to give special thanks to my loving wife, Sarah Wahba, my beloved children, Mark and Hannah Bastwros, my Parents, Mikhail Batswros and Marina Charobime, and my mom in law, Hoda Barsoum, for their support, encouragement, and understanding throughout my PhD Program.

ABSTRACT

The mechanical properties of composite materials are mainly determined by their microstructures that depend on comprising phases and their properties, the shape and size of those phases, and their distribution. By controlling and optimizing the various aspects of the microstructure, composites with improved mechanical properties can be created. One of the challenges, however, is the lack of scalable fabrication method capable of making complex structures. The conventional fabrication techniques for MMCs have been limited to fabricating simple structures with homogeneous dispersion of constituents. In this work, various fabrication approaches that can control the microstructure in metal matrix reinforced with nanoparticles have been studied. Mechanical alloying (ball milling) was used to control the dispersion of graphene sheets in homogeneous reinforced aluminum composites. Spray assisted deposition of nanoparticles was used to fabricate layered composites with uniformly and hierarchically reinforced interfaces. Magnetic field assisted deposition was studied to manipulate and deposit nanoparticles into micro-patterns that can be used to create hierarchically layered composites.

Homogeneously reinforced aluminum alloy (Al6061) reinforced composites with graphene have been synthesized using mechanical alloying followed by semisolid sintering. The ball milling was used to control the dispersion as well as the cluster size of the graphene within the matrix. The effect of ball milling time on the fabricated composites was studied. A significant enhancement in the mechanical properties of the graphene reinforced composites was observed compared with the matrix material processed at the same condition.

Layered composites, which are uniformly or hierarchically reinforced at the interfaces, have been synthesized by implementing two processing concepts: spray assisted deposition and metallurgy (semi-solid sintering). Ultrasonic spray deposition creates nano-/micro-/meso-scale

patterns on metallic sheets, which are then stacked together, densified, and synthesized into a composite through pressure assisted semi-solid sintering process. Silicon carbide (SiC) nanoparticle reinforced lightweight alloys (i.e. Magnesium Alloy (AZ31) and Al6061) have been synthesized. The synthesized composites showed an improvement in the strength with minor decrease on the total elongation.

Magnetic field directed manipulation of nanoparticles was demonstrated to self-assemble and deposit nanoparticles into user-defined micro-patterns on Al substrate for potential use in synthesis of hierarchically structure layered composites. The magnetic field was modulated by machining (e.g. micro-milling and laser machining) user-defined pattern of protrusions on the magnetic source surface. The deposition of magnetic particles as well as mixtures of magnetic and nonmagnetic nanoparticles was studied.

CHAPTER 1 INTRODUCTION

1.1 Motivation

The outstanding mechanical behaviors of natural biological materials, such as wood, bones, dentin enamels, shells, bird beak, etc., have attracted the interests of many researchers. The properties of these biological composites are often superior to the theoretically averaged properties of its constituents due to several characteristics: their complex multiscale structures, structured interfaces, and the nanostructure of its constituent phases. Fabricating a composite with one or more of those characteristics may yield a combination of favorable properties in strength, hardness, damage control, and fracture toughness, which cannot be obtained in simple structure composites. Numerical testing and modeling work have been conducted to evaluate, optimize, and investigate hierarchical composite structures [1-5]. Mishnaevsky et al. have conducted a numerical testing study on composites reinforced with hard brittle inclusions with various complex and simple configurations [6]. It was found that clustered and layered microstructures resulted in high fracture energy compared with rather simple structures. In their recent work on the computational micromechanical analysis of the nano-engineered interfaces in biocomposite materials and artificial composites [7], they concluded that nanostructured interfaces is a promising approach to tailor the material deformation and mechanical properties. Most of prior experimental research on mimicking the complex structure of biomaterials has been implemented through polymer matrix systems [8-12]. However, very limited progress has been made on metallic matrix systems [13]. Li et al. (2015) fabricated graphene/aluminum composites with bioinspired nanolaminated structure by using suspension mixing, sedimentation, and then pressing followed by extrusion [13].

Metal matrix composites (MMCs) produced nowadays, however, have been limited to rather simple structures of dispersing reinforcing particles or fibers in the matrix phase by powder sintering, filling of preform by infiltrate casting, graded structures by centrifugal casting, or alignment of fibers by secondary processes like extrusion. The traditional fabrication routes for MMCs, such as milling and blending [14-18], powder metallurgy [19-23], melt processing [24-26], and others [27, 28], are not capable of creating complex structures. A more versatile, flexible, scalable manufacturing method is needed to realize such sophisticated designs in MMCs [29]. In this study, novel fabrication approaches have been investigated to fabricate MMCs with controlled and custom designed structures.

In this work, mechanical alloying was used to control the dispersion and clustering of the graphene within the aluminum matrix (Al6061). MMCs reinforced with graphitic structure elements (CNT, graphene, etc.) have increasingly attracted the interest of many researchers. One of major concerns in fabricating MMCs reinforced with graphitic structure elements has been dispersing the nanoparticles homogeneously within the matrix and the wetting between the reinforcement element and the metal phase. Various researchers have used mechanical alloying (ball milling) as an effective means to disperse the CNTs [15, 30-35]. Kim et al. [36], Esawi et al. [30, 37], and Wang et al. [38] have investigated the effects of the mechanical alloying time on the dispersion of CNTs in ball milling. Kim et al. have investigated the effects of milling time on the CNT structure, and it was reported that the length of CNTs shortened significantly with increasing milling time [36, 39]. Graphene, being the basic structural element for the CNT, also has a great potential as a reinforcing material but with a different form factor. The graphene is favored by excellent mechanical properties and high electrical and thermal conductivities [38]. Not much research, however, has been found on the synthesis of metal-graphene composites

using ball milling and on understanding the effect of graphene dispersion on mechanical properties. In this study, ball milling was used to fabricate Al6061-graphene nanocomposites followed by semi-solid consolidation.

Next, layered MMCs with uniform and hierarchical reinforcements at the interface with multiscale and multiphase structure have been fabricated. Two processing concepts have been used to fabricate the composite: spray assisted deposition and semi-solid sintering. Among different spraying techniques, ultrasonic spraying is favored by its narrow atomization droplet size distribution and its low spraying velocity (in the order of 1 m/s), which allows accurate control on the deposition rate and deposition morphology. Ultrasonic spraying techniques was used to deposit nanoparticles into micro-scale patterns on metallic sheets, which are then stacked together, densified, and synthesized into a composite through the pressure assisted semi-solid sintering.

Finally, magnetic field assisted deposition is another approach that was used to manipulate the nanoparticle deposition into user-defined patterns. Magnetic manipulation of nanoparticles can be a promising approach to selectively deposit nanoparticles if the applied magnetic field is precisely modulated. Conventionally, magnetically directed surface-patterning has been limited to magnetic particles [40-42]. In this work, a novel approach has been demonstrated to manipulate not only magnetic particles but also a mixture of magnetic and nonmagnetic particles.

1.2 Research framework and objectives

1.2.1 Effect of ball milling on graphene reinforced Al6061 composite fabricated by semi-solid sintering

High strength, high thermal properties, and tribological behavior make graphene a good candidate as a reinforcement material for MMCs. However, progress in fabrication MMCs reinforced with graphene has been rather slow due to the hard dispersion and clustering of graphene. In this section, graphene reinforced aluminum alloy 6061 (Al6061) composite was synthesized by mechanical alloying and semi-solid sintering. The effects of mechanical alloying time on the powder morphology, graphene dispersion, flexural strength, fracture surface, and composition of the Al6061-graphene composite were investigated. Raman spectroscopy has been used to evaluate the effect of ball milling on the graphene structure.

1.2.2 Ultrasonic spray deposition of sic nanoparticles for laminate metal composite fabrication

In this section, the deposition of SiC nanoparticles via ultrasonic spraying process was investigated for a potential application in synthesis of laminate metal composites. The main objective was to control the microstructure of the pattern deposited from ultrasonic spraying by understanding atomization, transport, and deposition of a liquid solution containing elements and/or chemicals that will form various reinforcement phase architectures. Governing parameters of the ultrasonic spraying process, which included suspension and spraying parameters, and their influence on the deposited structure have been analyzed. The potential of using ultrasonic spraying to fabricate laminate composites reinforced at the interfaces with nanoparticles have been investigated.

1.2.3 Fabrication of pattern reinforced AZ31 multilayer composite using ultrasonic spray deposition

Mimicking the unique hierarchical, multiscale structures of natural biological materials is a promising approach to create novel materials with outstanding properties. One of the challenges, however, is the lack of scalable fabrication methods capable of making such complex structures. In this section, a multilayer nanocomposite has been synthesized by incorporating an ultrasonic spray deposition technique and semi-solid sintering. The spray deposition system was used to deposit nanoparticles on substrate foils, which were consolidated to synthesize the multilayer composite. A patterned mask was used to create micro-patterns with nanoscale structures. A magnesium alloy, AZ31, foil was used as the matrix material. A mixture of nano-silicon carbide (nano-SiC) and aluminum alloy, Al6061, particles was used as the reinforcement phase in the deposited patterns. The main objectives were to create and control the pattern deposition using a mask, and to study the densification and consolidation behavior of the deposited patterns by compositional analysis and mechanical testing.

1.2.4 Magnetic field assisted deposition of nanoparticles in pattern structures

Magnetically directed surface-patterning has been a promising approach for direct assembly of nanoparticles in custom user-defined shapes. Conventionally, magnetically directed surface-patterning has been limited to magnetic particles only, which narrows the range of potential applications. In this section, novel approach is demonstrated to manipulate a mixture of magnetic and nonmagnetic particles using an external magnetic field to be self-assembled into micro-patterns on a substrate foil for potential application in synthesis hierarchical nanostructured composites. The main objective is to understand nanoparticles behavior (transfer, interaction, self-assembly) under the effect of modulated magnetic fields.

1.3 Dissertation organization

The rest of this thesis is divided into five chapters. In Chapter 2, fabrication of graphene reinforced Al6061 composites using ball milling was investigated. In Chapter 3, the implementation of ultrasonic spray deposition techniques to fabricate MMCs were assessed, and the governing parameters that controls the deposition structure were investigated. Chapter 4 presents a novel approach to fabricate hierarchical structure composites using ultrasonic spraying techniques. In Chapter 5, a novel technique that uses a modulated external magnetic field to manipulate and deposit a mixture of magnetic and nonmagnetic particles is presented. A summary and contributions are presented in chapter 6. Chapter 6 is followed by a complete list of bibliography.

CHAPTER 2 EFFECT OF BALL MILLING ON GRAPHENE REINFORCED AL6061 COMPOSITE FABRICATED BY SEMI-SOLID SINTERING

2.1 Introduction

Recently, MMCs reinforced with nano-elements have attracted the interest of many researchers [43-48]. Graphitic structured materials like carbon nanotubes (CNTs), graphite, and graphene have been among the more widely researched materials due to their exceptional mechanical [49], thermal [50, 51], electrical properties [52], and tribological behavior [53, 54]. Moreover, improved manufacturing techniques have made these nanomaterials more affordable [32, 36, 55-57].

Various studies can be found in which CNTs were used as a reinforcement phase with different base metals like copper [46, 58, 59], aluminum [30, 32, 37, 43, 44, 53, 57, 60], and their alloys [36, 55, 56, 61]. Graphene, being the basic structural element for the CNT, also has a great potential as a reinforcing material but with a different form factor. The graphene is favored by excellent mechanical properties and high electrical and thermal conductivities [38]. Not much research, however, has been found on synthesis of metal-graphene composites and on understanding the effect of graphene dispersion on mechanical properties. Wang et al. have fabricated graphene reinforced aluminum composites using flake powder metallurgy. The composite strength showed an enhancement in the tensile strength by 62% compared with unreinforced aluminum [38]. Bartolucci et al. fabricated 0.1 wt % graphene-aluminum composites fabricated using ball milling followed by sintering for 4 hours at 550°C. A degradation in the mechanical properties of the composite was reported due to the formation of large amount of carbide phases during sintering [45]. Perez-bustamante et al. fabricated graphene reinforced aluminum composites using ball milling and an enhancement in the

hardness values were observed [62]. Although some studies report significant mechanical property enhancement, however, dispersion the graphene within the matrix has been always a challenge. In this work, ball milling technique was used to disperse the graphene within the Al6061 matrix. In a recent study by Zhang et al. (2016) [63], ball milling was successfully used to disperse the graphene nanoplatelets within the al alloy matrix, reporting an increase in both the yield strength and the ultimate tensile strength by more than 50%.

In this study, graphene reinforced Al6061 composites were fabricated using ball milling techniques. The aluminum-graphene composite was synthesized in the semi-solid state of the aluminum alloy by pressure-assisted sintering. The effect of ball milling time on the dispersion of the graphene and its influence on mechanical properties and microstructure has been investigated.

2.2 Material and methods

Graphite was expanded to exfoliate graphene according to the modified Brodie's method. First, 10 g of graphite, 160 ml of nitric acid, and 85 g of sodium chlorate were mixed at room temperature. The mixture was kept for 24 hours under continuous stirring. Then it was washed with 5% hydrochloric acid and distilled water for four times. The intercalated graphite was achieved through sedimentation and finally was dried at 60°C. With the aid of ultrasonication, the intercalated graphite was exfoliated to monolayer or "few-layer" graphene oxide [64].

Aluminum alloy 6061 (Al6061) was used as the matrix phase, and its chemical composition is listed in Table 2.1. Mechanical alloying was performed using a SPEX 8000x ball milling machine to disperse the graphene into the Al6061 particles. The initial average sizes of Al6061 and graphene particles were 13.8 μm and 100 μm , respectively.

Table 2.1 Chemical composition of Al6061

Element	<i>Cr</i>	<i>Cu</i>	<i>Fe</i>	<i>Mg</i>	<i>Mn</i>	<i>Si</i>	<i>Ti</i>	<i>Zn</i>	<i>Al</i>
Amount (%)	0.09	0.28	0.27	1.03	0.03	0.52	0.01	0.06	Bal.

Al6061-1.0 wt.% graphene samples were prepared at various ball milling times: 10, 30, 60, and 90 minutes. In addition, a reference sample was prepared for each ball milling time with only Al6061 powder to isolate the strain hardening effect that came from the ball milling. The ball milling was performed in ambient conditions without any process controlling agents. 0.05 g of graphene was mixed with 4.95 g of Al6061 in a zirconia vial. Two zirconia balls, weighing 7.5 g each, were used in the mixing process, resulting in a ball to powder ratio (BPR) of 2.6. The ball mill was stopped for 30 minutes after every 10 minutes of operation, to prevent heating of the powder.

The experimental setup used for the composite synthesis is shown in Figure 2.1. The die was made of H13 tool steel and was lubricated by spraying a thin layer of boron nitride to prevent a potential reaction between the aluminum and the die at elevated temperatures. The consolidation was performed in two stages. First, a pre-compaction pressure of 50 MPa was applied to the alloyed powder at room temperature. Then, the powder compact was hot-pressed at 100 MPa for 10 minutes in the mushy zone (between the solidus and liquidus temperature of Al6061) at 630°C. The liquid phase fraction at this temperature is about 18%.

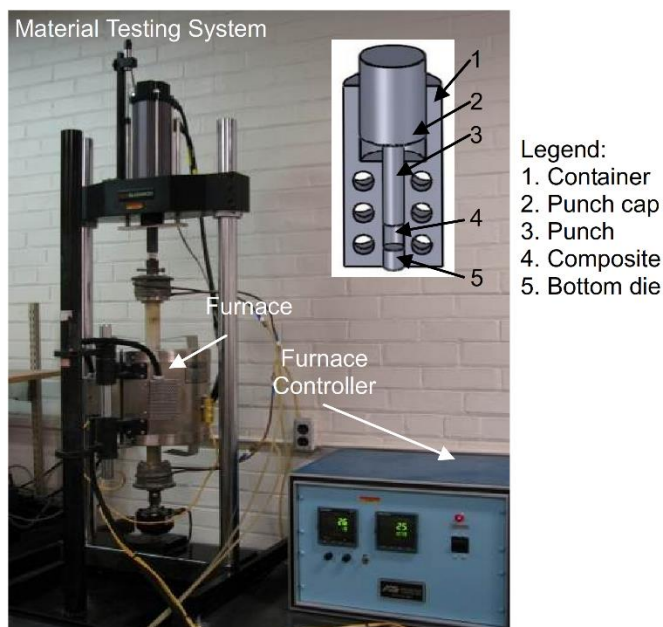


Figure 2.1 Experimental setup for semi-solid sintering

The obtained composites were cut using a low-speed diamond testing system. The fracture surfaces and the ball milled powder saw and were polished to the final dimensions (0.9 mm in thickness and 1.2 mm in width) needed to perform a three-point bend test. The flexural stress and flexural strain were recorded using the materials were examined using a scanning electron microscope, or SEM (FEI Quanta-250 field-emission scanning electron microscope). An XRD analysis was performed to check the carbide formation during consolidation. A Raman spectroscopy analysis was performed to study the effect of mechanical milling on the evolution of the graphene structure. Raman spectra of graphene were obtained using a confocal Raman spectrometer (Voyage, B&W Tek, Inc.). The laser beam ($\lambda = 532$ nm) was focused using a 50 \times objective lens before irradiating the samples. The laser energy was 2 mW and was uniformly distributed in space; this did not damage the samples. The laser spot size was 2 \times 4 μm^2 , and was determined by using a blade method.

2.3 Results and discussion

With the aid of sonication, the intercalated graphite was exfoliated to few-layer graphene, while some of them were in the monolayer state. A transmission electron microscopy (TEM) image of few-layer graphene is shown in Figure 2.2.

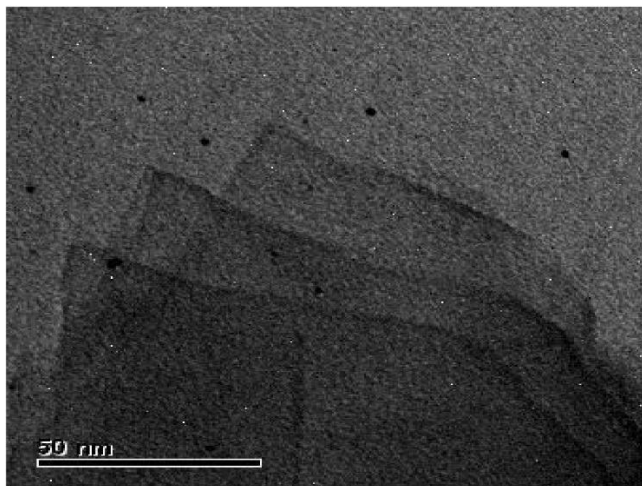


Figure 2.2 TEM image of few-layers graphene

A portion of the mechanically alloyed powder was extracted at the specified milling times (30, 60, and 90 minutes) for analysis under the SEM. As shown in Figure 2.3, the alloyed particle size increased with longer milling times. However, the graphene size decreased as the milling time increased. During mechanical alloying, cold welding and fracturing mechanisms compete with each other. Cold welding is dominant for the ductile Al6061 particles as they strain harden by the impact from the balls [30, 39]. On the other hand, the agglomerated graphene is fractured and delaminated. These fractured graphene flakes are repeatedly enclosed and embedded into the cold welded aluminum particles by ball milling. Comparing the alloyed powder at 30 minutes and again at 60 minutes in Figure 2.3, the overall particle size increased while the graphene flakes decreased in size. At 90 minutes, it was noticed that the composite particle shape had changed from platelet to particulate shape. It was also very difficult to locate

the graphene, which indicated that the majority of the graphene had been embedded into the aluminum particles by ball milling process.

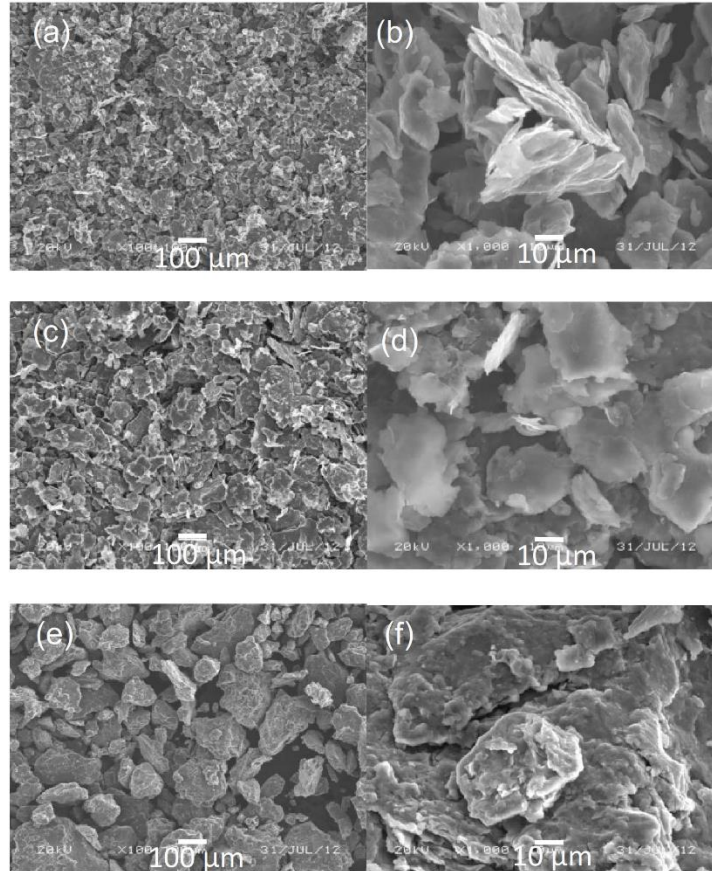


Figure 2.3 SEM images of the milled Al6061-1.0 wt.% graphene powder at different milling times: (a, b) milled for 30 min, (c, d) milled for 60 min, (e, f) milled for 90 min

Raman spectroscopy was employed to check the evolution of graphene structure during composite processing. Three samples were used: 1) as-received graphene; 2) Al6061 alloyed with 2.0 wt.% graphene particles ball milled for 90 minutes; and 3) Al6061 alloyed with 2.0 wt.% graphene particles ball milled for five hours. Samples with higher concentration of graphene (Al6061-2.0 wt.% graphene) were used to enhance the accuracy of the data collected during the Raman test. The higher the graphene concentration is, the higher the signal intensity

is. 90 minutes of milling time was the maximum milling time used to synthesize the samples used in this study. Prolonged milling time, however, was needed to provide insight into the progression of damage in the graphitic structure beyond the milling times used to make the composites. Therefore, Raman measurement data for the five hours of milling time sample were provided, which showed further changes in the graphitic structure that were not apparent. Figure 2.4 shows the Raman spectra of graphene samples. The integration time was 60 seconds. The Raman peaks are fitted with the Lorentz function to obtain the precise Raman intensity and wavenumber. The results are summarized in Table 2.2.

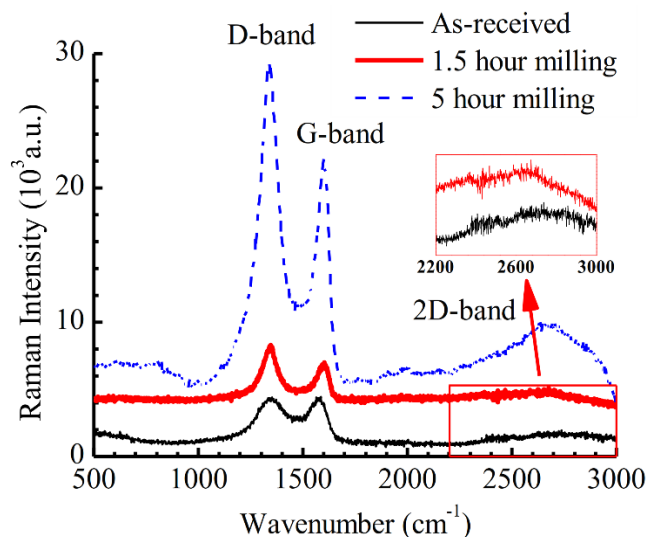


Figure 2.4 Raman spectra of the milled Al6061-2.0 wt.% graphene powder at different milling times and as-received graphene

Table 2.2 Raman data of the milled Al6061-2.0 wt.% graphene particles

State	I_D/I_G	I_G/I_{2D}	ω_G (cm ⁻¹)
As-received	1.08	0.65	1572.7
90 min milling	1.46	0.38	1593.9
5 hour milling	1.42	0.28	1594.0

The Raman spectrum of the as-received graphene oxide samples shows a D-band at 1349 cm^{-1} , a G-band at 1573 cm^{-1} , and a 2D-band at 2667 cm^{-1} . The G-band is the intrinsic vibration mode of a single graphite crystal. The D-band is related to the disorder in the graphene oxide and presence of sp^3 defects. The 2D-band is the overtone of the D-band, and is much smaller with respect to the D and G peaks.

The Raman spectra of graphene are related to the quality of the samples. The intensity ratio of D-band to G-band (ID/IG) indicates the disordering and defect density in the graphitic structures. After ball milling for 90 minutes, ID/IG increased from 1.1 to 1.4, which indicated disordering and defects in the graphene structure [65]. The amount of defects increased in the graphene after the ball milling because of the physical force applied during the process. In Table 2, the ratio of the ID/IG increased to 1.46 after 90 minutes of ball milling, which indicated that the ball milling introduced more defects and disorder to the graphene clusters. After further milling up to five hours, the ID/IG ratio did not change, which implied that there were no further defects introduced to the graphene structure. That could be attributed to the fact that the graphene sheets were embedded inside the Al6061 particles, which helped to protect them from further damage.

The ratio of integrated intensities $\text{IG}/\text{I}2\text{D}$ decreases as the number of layers decrease [66]. The ratio of $\text{IG}/\text{I}2\text{D}$ dropped from 0.65 to 0.38 after the sample was milled for 90 minutes. After further ball milling for up to five hours, the ratio decreased to 0.28. The number of graphene layers changed from four layers to two (bilayer), and finally reached a monolayer configuration according to the reference [66]. The number of graphene layers dropped due to the physical force introduced in the powder composite during the mechanical alloying, which helped to separate the graphene layers from each other.

The peak position of the G-band (ω_G) indicates the stress experienced in the graphene. When graphene is strained, the interatomic distances of the graphene change; hence the vibration frequency of the G-band changes, which leads to a wavenumber shift. When the strain is larger, so is the shift of the wavenumber. In the experiments, the wavenumber increased from 1573 cm⁻¹ (the as-received graphene) to 1594 cm⁻¹ after 90 minutes of ball milling. The interatomic distances in the graphene were reduced, and the residual compressive stresses increased in the samples. The wavenumber, however, increased a small amount (~ 0.1) between a milling time of 90 minutes and five hours of milling time, which indicated that the stress experienced by the graphene did not change significantly [67].

The flexural stress and strain were calculated from the measured force and displacement data using equations (1) and (2) [39].

$$\sigma_{fl} = 3PL / 2wh^2 \quad (1)$$

$$\varepsilon_{fl} = 6d_c h / L^2 \quad (2)$$

σ_{fl} and ε_{fl} are the flexural stress and flexural strain, respectively. P is the load, L is the support span, w and h are the width and depth of the specimen, respectively, and d_c is the deflection at the middle of the span.

The calculated flexural stress and strain curves of the Al6061-1.0 wt.% graphene composites are plotted in Figure 2.5 along with the reference Al6061 milled for the same duration. In general, the strength of the graphene-reinforced composite and the reference Al6061 increased as the mechanical alloying time increased, while the flexural strain to failure decreased [14]. The strengthening in the reference Al6061 can be attributed to strain hardening by ball milling [68]. The strength increase in the graphene-reinforced composite may come from three

main contributors: graphene addition [38]; strain hardening due to ball milling [30, 36, 39, 44, 60]; and carbide formation due to the reaction between the molten aluminum and defects at the graphitic planes [45]. By comparing the bend test results of the composite with the reference sample, strengthening due to strain hardening may be estimated.

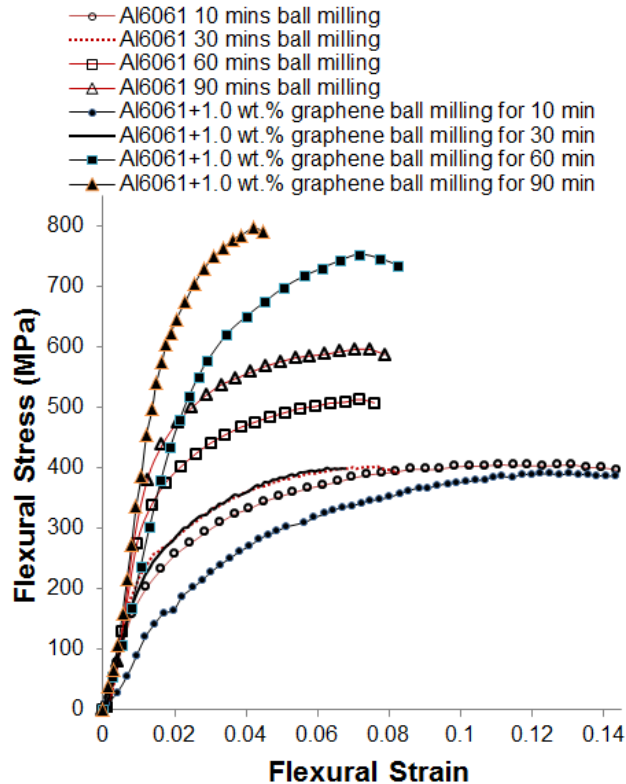


Figure 2.5 Flexural stress–strain curves of Al6061-1.0 wt.% graphene

In Figure 2.5, the addition of graphene did not improve the strength for Al6061-1.0 wt.% graphene composites made at 10 minute and 30 minute milling times when compared with the reference Al6061 consolidated under the same conditions. The milling times were not long enough to fully disperse the graphene into the Al6061 matrix particles [30, 39] resulting in degradation of mechanical properties. With only 10 minutes of milling, it was observed that the agglomeration of graphene significantly weakened the composite, to a point where the strength

was less than the reference Al6061 (without any graphene). This conglomeration interrupts the consolidation and results in producing defects in the composite [69-71]. As the milling time increased to 60 minutes and 90 minutes, the flexural strengths increased significantly to 760 MPa and 800 MPa, respectively. Compared with the corresponding Al6061 reference sample (milled for the same milling time), the strength increase was 47% and 34% for the 60-minute and 90-minute composites, respectively. The tensile strength of the monolayer graphene oxide (2D layer) reported in literature is about 130 ± 10 GPa [72]. The rule of mixture was applied and the lower and upper bound of the composite strength was calculated to be 1696 MPa and 404 MPa, respectively. The maximum reported strength in this study was around 800 MPa, which is laying within the upper and lower bound range. The composite strength was not close to the upper bound limit because of the presence of the graphene oxide in multilayer form and the graphene oxide particles are randomly oriented within the composites. Furthermore, the ball milling had introduced some defects to the graphitic structure as discussed earlier which contributed to the relative degradation of the graphene strength compared to the monolayer properties [73].

The strengthening may be due to the addition of 1.0 wt.% graphene and/or carbide that formed during the synthesis [36, 39]. Unfortunately, the individual contributions from the graphene and the carbide cannot be evaluated at this point. Figure 2.6 shows the XRD analysis results for the Al6061-1.0 wt.% graphene samples at various milling times. Aluminum carbide peaks were not detected, but this does not necessarily mean that no carbide was formed. The amount of carbide formation may be below the level of sensitivity of the XRD apparatus used, which is about 1.0 wt.%.

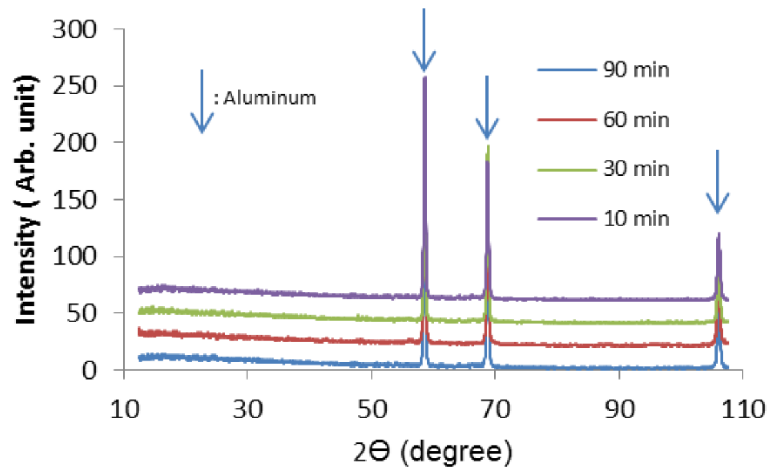


Figure 2.6 XRD analysis of the Al6061-1.0 wt.% graphene samples at different milling times

In Figure 2.7, SEM images of the fracture surfaces of the Al6061-1.0 wt.% graphene composites that were prepared at different milling times are presented. As shown in Figure 2.7, the plastic deformation, represented by the ductile fracture dimples, decreased as milling time increased. Comparing the 30-minute (Figure 2.7 (c, d)) and the 60-minute (Figure 2.7 (e, f)) milling time samples, a change in the morphology of the surface is observed. The dimples of the ductile fracture observed in the 30-minute sample diminished and numerous flat regions were detected on the 60-minute sample fracture surface. As the milling time increased, the sharp decrease in the size of the ductile dimples of the fracture surface indicated that the ductility of the composite had decreased significantly [39]. This change in the fracture surface was also accompanied by a change in the mechanical behavior as discussed and shown in Figure 2.5. As discussed earlier, 30 minutes of milling was not enough for the graphene to be uniformly dispersed throughout the Al6061 matrix, resulting in no enhancement in, or even deterioration of the mechanical properties [69].

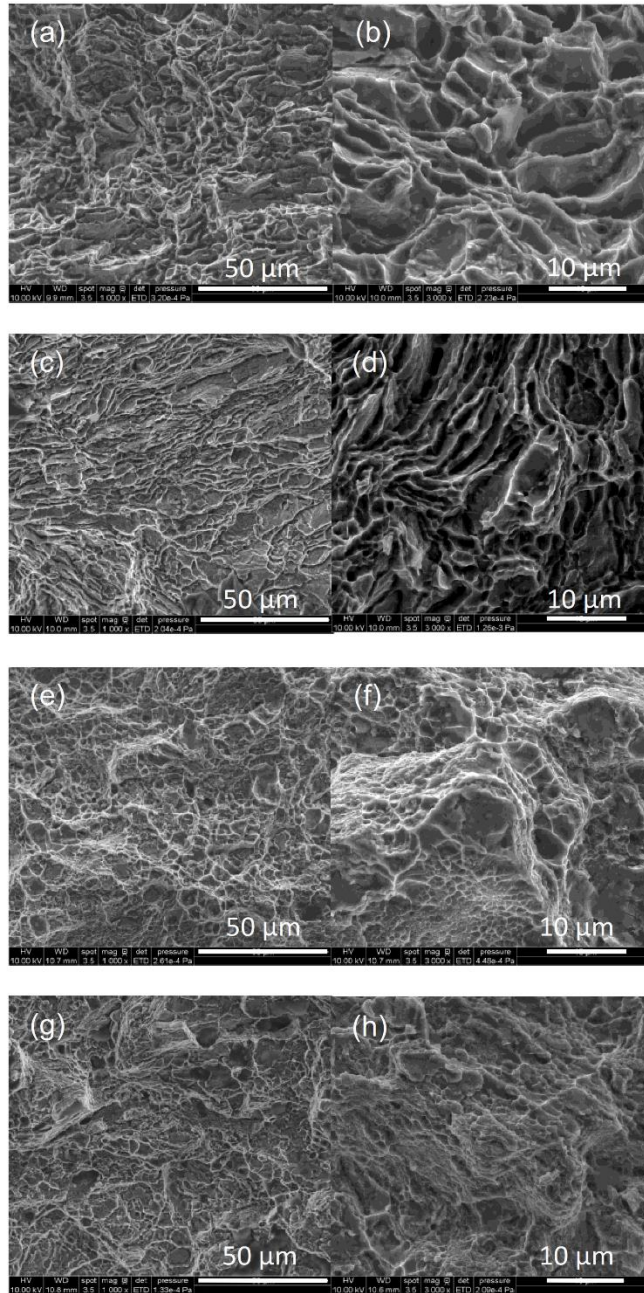


Figure 2.7 SEM images of fracture surfaces of the Al6061-1.0 wt.% graphene composites prepared at different milling times: (a, b) 10 min, (c, d) 30 min, (e, f) 60 min, and (g, h) 90 min

Figure 2.8 compares the fracture morphology of Al6061 (no graphene) and Al6061-1.0 wt.% graphene ball milled for 90 minutes. It is evident that the size of the ductile dimples

decreased significantly when graphene was added and dispersed within the matrix through ball milling. This indicates that the ductility decrease of the Al6061-1.0 wt.% graphene composite was most likely due to graphene addition and its dispersion rather than solely from the hardening effect from milling.

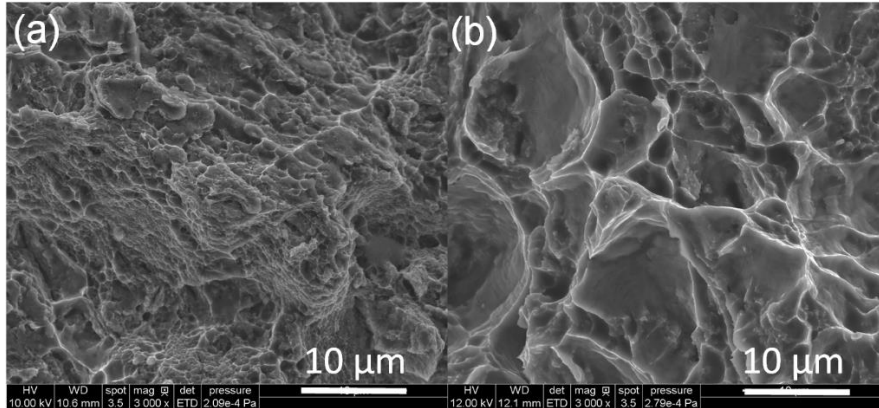


Figure 2.8 SEM images of fracture surfaces: (a) Al6061-1.0 wt.% graphene milled for 90 min, and (b) Al6061 unalloyed milled for 90 min

Figure 2.9 shows a crack on the fracture surface on the Al6061–graphene composite ball milled for 10 minutes. These large cracks were not visible on the fracture surfaces of other composites that were milled for more time (30, 60, and 90 minutes). They were formed due to the poor interface between the large graphene cluster and the matrix phase, which acted as a crack nucleation site. Under the bending load, these cracks propagated and grew, accounting for the inferior flexural strength of the Al6061-graphene sample when compared with the reference Al6061 sample. For longer milling times (30, 60, and 90 minutes), the dispersed graphene acted as bridges preventing and/or delaying micro-crack propagation paths [74].

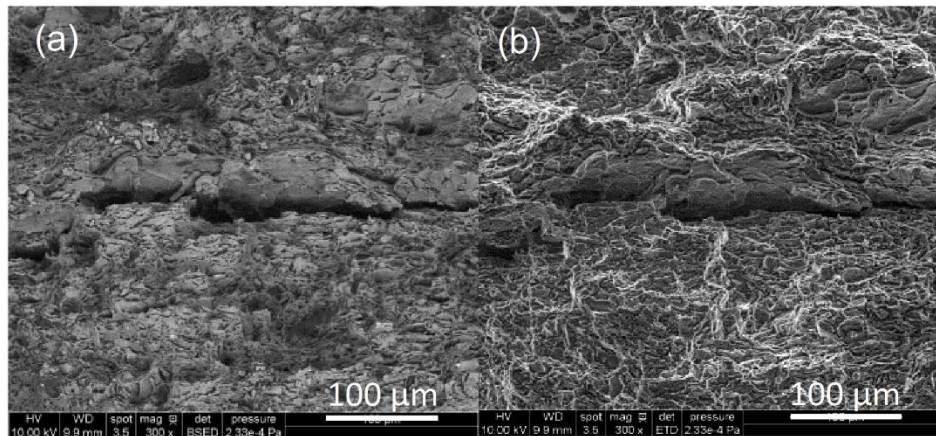


Figure 2.9 SEM images of fracture surface of Al6061-1.0 wt.% graphene composite milled

An exhaustive search for graphene was performed on all fracture surfaces. It was very difficult, however, to locate graphene for the 30-, 60-, and 90-minute milling time samples. For the 10 minute milling time sample, clusters of graphene layers were observed on the fracture surface as shown in Figure 2.10. Figure 2.10 (a and b) shows graphene cluster embedded into the matrix phase. In Figure 2.10 (a), a change in phase was observed between the clustered graphene and the matrix. Figure 2.10 (b) shows the topography of the graphene cluster. In Figure 2.10 (c, d, and e), a graphene cluster attached to the surface can be observed. For the graphene observed in this image, it was pulled normal to the fracture dimples in the direction of tensile loading caused by bend test. In Figure 2.10 (e), the layered graphene structure is clearly visible at high magnification.

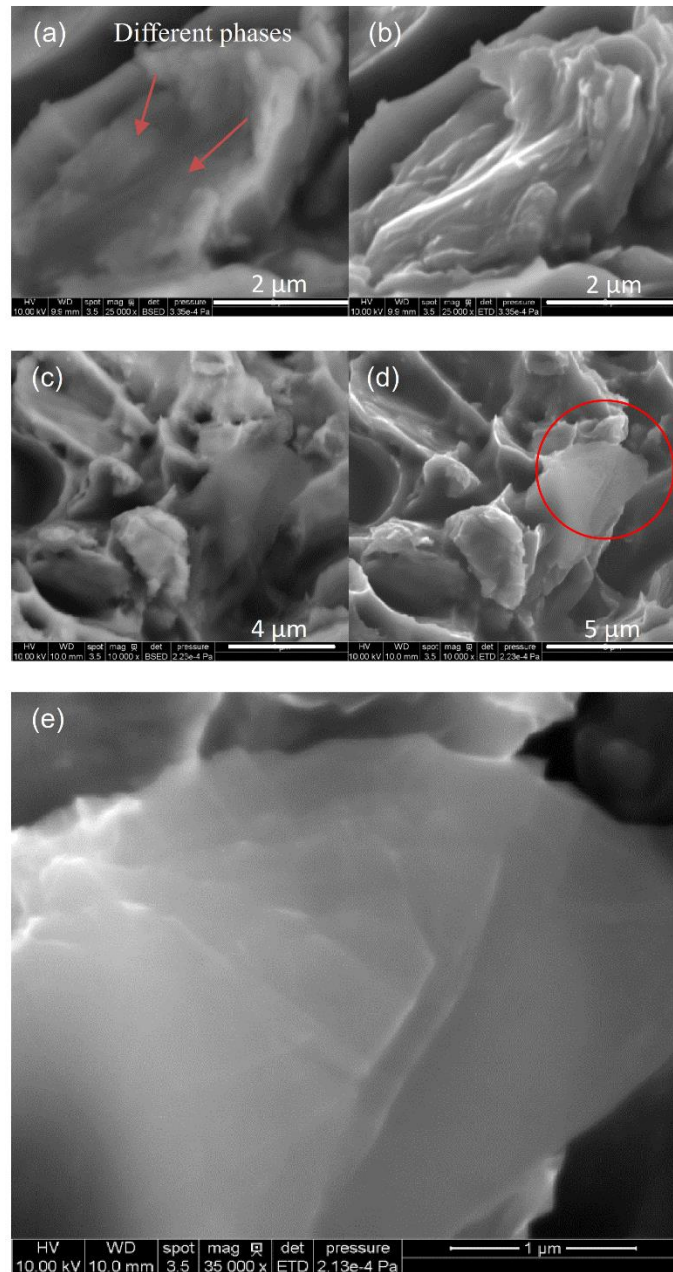


Figure 2.10 Images of graphene clusters: (a) BSEC detector SEM image of a graphene cluster embedded in the Al6061 matrix, (b) ETD detector SEM image, (c) BSEC detector SEM image of a graphene cluster attached to the surface, (d) ETD detector SEM imaging, and (e) higher magnification of the graphene layers

2.4 Conclusions

In this study, the Al6061-1.0 wt.% graphene composites were fabricated by ball milling Al6061 particles and graphene, followed by pre-compaction at room temperature, and finally by hot compaction in the semi-solid regime. The ball milling time varied from 10 minutes to 90 minutes. The 10- and 30-minute ball milling times were not enough to homogeneously disperse the graphene into the Al6061 matrix, which resulted in degradation of the flexural strength for the 10-minute milling time sample and no enhancement for the 30-minute milling time sample. The strength increase for the Al6061-1.0 wt.% graphene composite was 47% and 34% for the 60-minute and 90-minute times, compared with the reference Al6061 sample. According to the Raman analysis, further milling did not introduce more damage to the graphene, but instead helped to uniformly disperse the graphene and reduce the number of the stacked layers. It was concluded that the strengthening was significantly affected by the dispersion of the graphene in the matrix phase.

CHAPTER 3 ULTRASONIC SPRAY DEPOSITION OF SIC NANOPARTICLES FOR LAMINATE METAL COMPOSITE FABRICATION

3.1 Introduction

Various techniques have been used in material coating or surface deposition, including tape casting [75], thermal spraying [76], plasma spraying [77], electrostatic spray deposition [78], spray deposition [79], spray pyrolysis [80], and ultrasonic spray deposition [81]. Among these techniques, ultrasonic spraying offers several unique and desirable characteristics. The ultrasonic spraying nozzle vibrates at high frequency using two piezoelectric discs and an amplifier. This makes the liquid leave the nozzle tip in the form of mist that has a narrow droplet size distribution and a very low spraying velocity (in the order of 1 m/s) compared with other spraying techniques [82]. It is a process that is favored by its simplicity and low cost, in addition to its flexibility in producing thin multilayered deposited structures [83]. It offers a relatively moderate deposition surface temperatures of 100–500°C [84]. Accordingly, a wide variety of substrate materials can be used [85] by tuning the spraying parameters. The technique also allows accurate control of the deposition rate [86] and deposition structure [81]. In a recent study, the deposition structures of ultrasonic and handheld spraying techniques were compared, and the ultrasonic spraying technique resulted in a smoother and more uniform deposition structure [87]. It has been used to fabricate fuel cell electrodes [88], thin films [89, 90], nanocatalysts [91], high temperature oxidation resistant coatings [90], and electrochromic windows [92]. The atomized droplet size, which significantly influences the deposition structure and the spray quality, is mainly determined by the liquid properties (surface tension and density) and the nozzle vibration frequency [93]. Moreover, spraying parameters, such as the nozzle

vibration frequency, flow rate, deposition surface temperature [94], spraying air pressure [95], and spraying distance [86], affect the final deposition structure.

In this study, the ultrasonic spraying is used for spraying nano-suspension systems to deposit nanoparticles on substrate materials. Nano-suspensions or nano-fluids are liquid with homogeneously suspended nano-sized particles [96], which may be metals [97], oxides [98], carbides [90], and carbon structured materials [99]. One of the main advantages of using nanoparticle suspensions is the low tendency for particle agglomeration and sedimentation, which will keep the particles suspended and dispersed throughout the operation and may potentially improve the quality of deposited layer [96]. Nano-suspension spraying has been used in many applications. It has been used to process granular nanoparticles using various spraying techniques, where the suspension is sprayed and the droplet dries while traveling and can then be collected [100-103]. During drying, the nanoparticles can be self-assembled in various morphologies depending on the process conditions [104]. Moreover, spraying suspension of CNT has been used to deposit a CNT network film on a substrate to fabricate a conductive film for electronic applications [105, 106]. Hand spraying of CNT micro-ball suspension was used to fabricate dye-sensitized solar cells [107]. Spraying of nano-suspension was also used to fabricate solid oxide fuel cells using a conventional spraying atomizer [108]. In a recent study, ultrasonic spraying was used to deposit graphene flakes films on polymer-coated glass. The researchers chose the ultrasonic spraying technique as it produced relatively small droplets of a few micrometers that allowed rapid solvent evaporation [109].

In this study, the ultrasonic spraying technique was applied to accurately control the deposition structure of nanoparticles needed to produce layered metal composites reinforced by nanoparticles at the interfaces. Previous studies demonstrated that laminated composites can be

designed to improve several characteristics, including damage tolerance [110], impact toughness [111], fatigue behavior [112], corrosion resistance, wear resistance, formability, and ductility [113]. In manufacturing of metal laminate composites reinforced with nanoparticles, several studies were found, each of which employed techniques involving manual spreading of the reinforcements [114], immersing the substrate in suspension systems [115], and air gun spraying to deposit nanoparticles [116]. The challenge, however, has been in trying to precisely control the spatial distribution of the reinforcement elements.

In this study, the deposition of silicon carbide (SiC) nanoparticles using ultrasonic spraying method was investigated for the purpose of synthesizing a multilayer composite made of metallic matrix. Two different composites were fabricated, Al6061 aluminum alloy composites and AZ31 magnesium alloy composites. The study entailed understanding the effects of suspension and spraying parameters on the deposited microstructure. The size and amount of nanoparticles in the ethanol suspension affect the initial atomization droplet size, which was calculated using a theoretical model. The effects of the spraying parameters (flow rate, substrate surface temperature, air pressure, and nozzle to substrate distance) on the deposition morphology were investigated to identify appropriate parameter ranges to make the multilayer composite. Finally, Al6061 and AZ31 laminate composites reinforced by silicon carbide (SiC) nanoparticles were fabricated, and the potential use of ultrasonic spraying technique for laminate composite synthesis was discussed.

3.2 Experimental procedures

Ultrasonic spraying is a promising technique that can coat surfaces with various nanoparticles and chemicals, and in so doing, precisely control the deposited microstructure. In this study, an ultrasonic deposition system (Exacta-Coat Ultrasonic Coating System, Sono-Tek

Corp.) as shown in Figure 3.1 was used to perform the spraying. The system features a sonic syringe that controls the flow rate of the suspension and provides bursts of vibration to prevent the suspended particles from developing sedimentation and agglomeration.

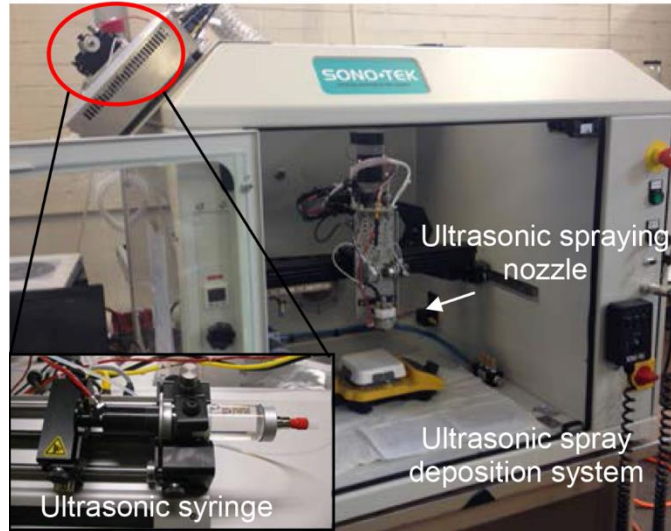


Figure 3.1 Ultrasonic spray deposition system

The spray-deposited structure can be influenced by various processing parameters, which may be classified into two categories: suspension and spraying parameters. The suspension parameters are the suspended particle type, size, and SiC concentration. Suspension concentrations of 0-16 wt.% of SiC were used to study the effect on the surface tension for two different particle sizes, 80 and 800 nm. For the 800 nm SiC, it was challenging to keep the suspension homogeneous during the spraying process due to the particles developing sedimentation and tendency to clog the spraying tubes and system. On the other hand, the 80 nm SiC particle suspension could be kept stable for days, which made it favorable for the spraying process. Nanoparticles were mixed into ethanol and sonicated for six hours in an ultrasonic bath to achieve a stable and homogenous suspension [117]. The surface tension was measured using the pendant drop method [118]. The important spraying parameters that could affect the

deposition structure are the deposition surface temperature (T), the spraying suspension flow rate (Q), the spraying air pressure (P), and the nozzle distance (D) [82]. Each parameter was investigated by analyzing the deposited structure qualitatively under a scanning electron microscope (SEM). For spraying, a low suspension concentration was prepared using the 80 nm SiC particles with a concentration of 0.1 wt.% SiC.

Figure 3.2 shows a schematic overview of the spraying process and the spraying path. A total of 12 passes were used for each sample with a nozzle velocity of 10 mm/sec. The spacing between the centers of two adjacent lines was 2 mm, which provided small enough spacing so that the spray area overlapped and the final deposited structure was uniform. The detailed spraying conditions and parameters are summarized in Table 3.1.

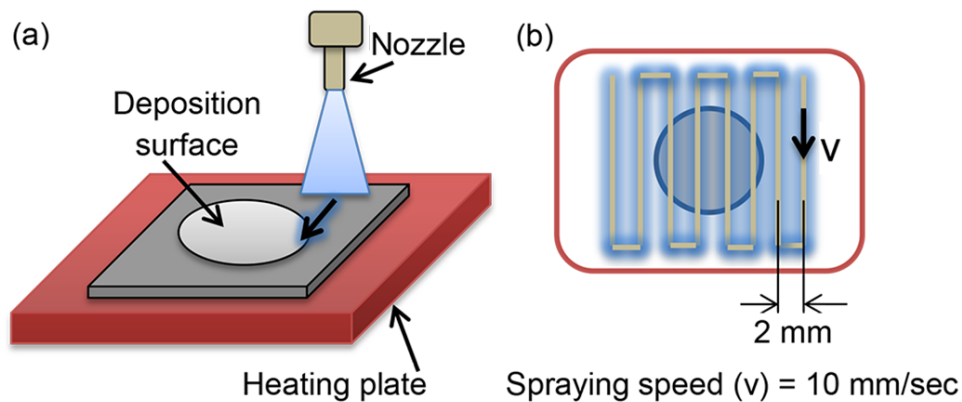


Figure 3.2 (a) Schematic overview of the spraying process and (b) spraying path

Table 3.1 Summary of the spraying parameters and their values

Parameters	Values
Material and particle size	SiC nanoparticles (< 80 nm)
Suspension medium and concentration	Ethanol + 0.1 wt.% SiC
Substrate thickness	80 μm
Sonication time	6 hours
Spraying type	Path spraying
Spraying speed	10 mm/sec
Spraying lines spacing	2 mm
Temperature (T)	140, 220, and 255°C
Flow rate (Q)	0.25, 0.5, and 1.0 ml/min
Air pressure (P)	0.25, 0.5, and 1.0 kPa
Distance (D)	15, 25, and 50 mm

For the Al6061-SiC laminate composite synthesis, a SiC nanoparticle layer was uniformly sprayed on the Al6061 sheet. Each composite comprised 21 layers of Al6061 sheets (60-70 μm thick) sprayed with SiC nanoparticles at the interface. The chemical composition of the Al6061 sheet is the following: 1.03% Mg, 0.52% Si, 0.06% Zn, 0.03% Mn, 0.28% Cu, Bal.% Al. The composite samples were prepared with SiC loadings of approximately 0.3 and 0.6 wt.% and without SiC nanoparticles for reference. The experimental setup used for composite synthesis is shown in Figure 2.1. The die was made of H13 tool steel and was lubricated by spraying a thin layer of boron nitride to prevent potential reaction between the aluminum and the die at elevated temperatures. The consolidation was performed in two stages. First, a pre-compaction pressure of 50 MPa was applied at room temperature. Then, the temperature was elevated to mushy zone (between the solidus and liquidus temperature of Al6061) while 10 MPa of pressure was maintained. Next, the compact was hot pressed at 50 MPa for 15 min at 635°C. The liquid phase percentage at this temperature is about 18%.

A laminate composite of magnesium alloy (AZ31) sheets and SiC nanoparticles were fabricated. The AZ31-SiC laminate composite was comprised of 15 layers of AZ31 sheets (80–

100 μm thick) sprayed with SiC at the interface. The chemical composition of the AZ31 sheet is provided in Table 3.2. Composites with different SiC loadings of 0, 0.15, 0.3, and 0.6 wt.% were synthesized. The experimental setup used for composite synthesis is the same used earlier and it is shown in Figure 2.1. The consolidation was performed in two stages. First, a pre-compaction pressure of 50 MPa was applied to the stacked layers at room temperature. Then the temperature was raised to the mushy zone of the AZ31 alloy (between the solidus and liquidus temperature of the AZ31 alloy) [36] while 50 MPa of pressure was maintained. The stacked layers were hot pressed under 50 MPa for 20 minutes at 610°C, at which temperature the liquid phase is about 9%.

Table 3.2 Chemical composition of AZ31 alloy

Chemical Composition Limits of AZ31 in wt.%										
	Al	Zn	Mn	Ca	Cu	Fe	Ni	Si	Others total	Mg
Min.	2.5	0.7	0.2	--	--	--	--	--	--	Bal.
Max.	3.5	1.3	1.0	0.04	0.05	0.005	0.005	0.05	0.3	Bal.

The obtained composites were cut using a diamond saw and were polished to the final dimensions (0.9 mm in thickness and 1.2 mm in width) needed to perform the three-point bend test. The flexural stress and flexural strain were recorded using the materials testing system.

3.3 Results and discussion

The droplet size is one of the main parameters that affects the deposited microstructure and is mainly determined by the ultrasonic frequency of the nozzle and the suspension properties (surface tension and density) [93]. The droplet size can be approximately estimated by Eqn. (1) [82], which represents a model that predicts the diameter of the atomized droplet exiting from the ultrasonic nozzle used in various studies [81, 82, 119]:

$$d_d = 2 \frac{\sqrt[3]{2}}{\pi} \left(\frac{\pi\sigma}{\rho f^2} \right)^{\frac{1}{3}} \quad (1)$$

where, σ and ρ are the surface tension and the density of the suspension, respectively; and f is the ultrasonic nozzle frequency. Note that the surface tension and density have opposite effect on the atomized droplet size.

Figure 3.3 (a) shows the relation between surface tension and particle loading for two different SiC particle sizes (80 nm and 800 nm). The surface tension increased as the SiC loading increased. Zhu et al. [120] reported a similar observation. Since the particles tend to agglomerate at the gas-liquid interface, it increases the concentration of particles at the surface. At the gas-liquid interface, two forces, repulsive force (electrostatic) and attractive force (van der Waals), compete with each other [121] and can affect the surface free energy of the suspension. At a low concentration, the particles are farther away from each other, and therefore, the particle interaction is lower, resulting in a lower surface tension according to Saeid et al. [122]. On the other hand, as the concentration increases, the distance between the particles becomes shorter, which increases the attractive force and results in surface free energy increase [122]. The observation also agrees with findings from other researchers [123].

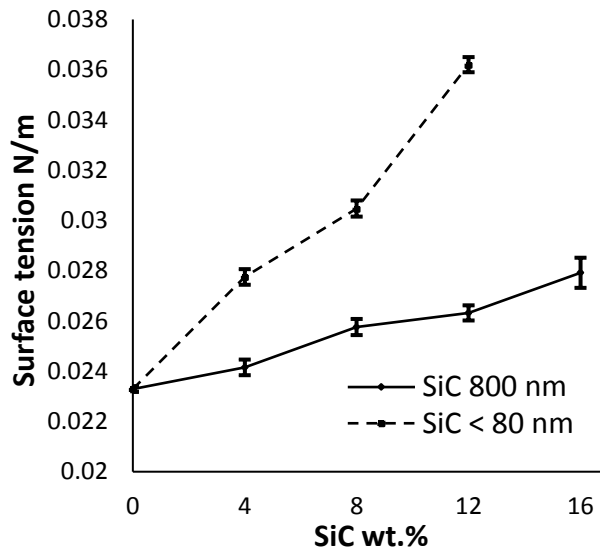


Figure 3.3 The effect of SiC loading and particle size on the surface tension of ethanol-SiC suspension system

It was observed that the suspension properties were significantly affected not only by the amount of the suspended particles but also by their size. When the same amount is loaded, the smaller particle size increases the total free surface area, which results in increase of the total surface free energy [121]. Moreover, the surface tension of the suspension affects the deposited structure. The morphology of the deposited structure becomes more uniform at a lower surface tension due to enhanced wetting that helps to enlarge the droplet spread area upon contacting the surface and allows merging of these droplets [124].

Using Eqn. (1), the droplet sizes for various conditions were calculated as shown in Figure 3.4. It can be noticed that the change in droplet size is reversed depending on the size of the suspended particle. As mentioned earlier, the surface tension and density have the opposite effect on atomization droplet size as the particle loading is increased. Since the change in surface tension is much lower for larger particles as the loading is increased, the droplet size decreased for larger particles with increasing loading (see Figure 3.4 (a)). However, for the

typical range of suspension concentration used in spraying, atomization droplet size is largely determined by the nozzle frequency as shown in Figure 3.4 (b). Since the spray system has a fixed nozzle frequency of 120 kHz, the expected droplet size is in the order of 15 μm .

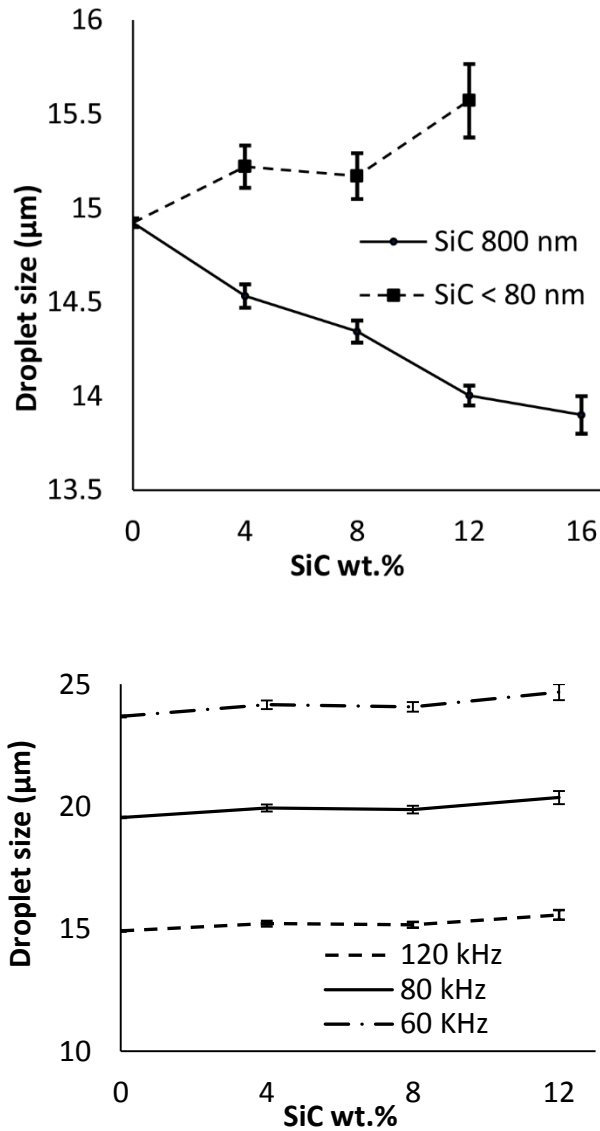


Figure 3.4 (a) Prediction of the atomization droplet size, and (b) prediction of the droplet size from the atomization using different atomization frequencies

The final deposited droplet size may vary depending on the evaporation and drying dynamics of the droplet when it contacts the heated surface [125]. Because the prediction of the

final droplet size before colliding into the substrate is complex, the deposition patterns of single droplets were experimentally measured. A single pass spray was applied on the heated substrate with a fast spraying speed of 100 mm/sec. The spraying was performed using a 0.1 wt.% SiC (80 nm)-ethanol suspension at 190°C, under air pressure of 0.5 kPa, and with a suspension flow rate of 0.25 ml/min. SEM images of the single droplets are shown in Figure 3.5.

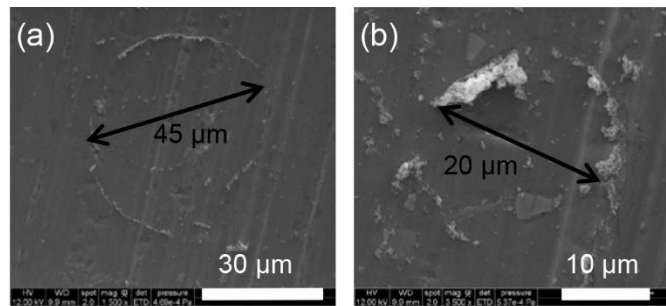


Figure 3.5 An atomized droplet deposited by a single pass experiment

It can be observed that nanoparticles form coffee ring patterns upon deposition and tend to cluster at the gas-liquid interface of the droplet [59]. Ring-like stains are commonly seen in the drops containing dispersed solutes. When the particles are homogeneously dispersed in the suspension droplet, the droplet spreads and the suspension begins to evaporate as soon as it collides with the surface. At the gas-liquid contact line, the suspended particles begin to deposit and cause the pinning of the contact line. Upon further evaporation, the droplet shrinkage is hindered in the horizontal direction, but it is allowed in the vertical one. The pinning of the contact line causes the migration of the liquid to the contact line to replenish the evaporated liquid. As a result, the particles carried by the liquid deposit and cluster at the contact line [126]. The size of the deposited droplet patterns varies in a wide range with a minimum of few microns to a maximum of about 50 μm. Most of the patterns, however, ranged between 20 and 50 μm,

which are larger than the initially estimated atomized droplet size of 15 μm , since the droplets spread due to the momentum as soon as it contacts the surface.

The effect of the flow rate on the deposited structure is shown in Figure 3.6. The samples were sprayed using a 0.1 wt.% SiC (80 nm)-ethanol suspension at the heat plate temperature of 220°C, under the air pressure of 0.5 kPa, and at the flow rates of 0.25–1.00 ml/min. As the flow rate increased, the SiC cluster size increased. Figure 3.6 (d) and (f) show that the SiC particles form a continuous line of segregated particles, which is interrupted by large clusters of SiC nanoparticles. The formation of such clusters during evaporation depends on the evaporation time of the suspension during its transportation to the substrate and after deposition. As the flow rate increases, the amount of liquid phase transported during spraying is higher, resulting in a longer evaporation time. The presence of a relatively large amount of the liquid phase on the deposition substrate allows the suspended particles to segregate and cluster at the contact lines. In contrast, spraying at a lower flow rate will help improve the uniformity and homogeneity of the deposited microstructure. The deposited structure will be favored with relatively smaller discontinuous nanoparticle clusters with a narrower clusters size distribution (Figure 3.6 (a)). For the 0.25 ml/min sample, the deposited nanoparticle cluster size varied from a single particle (80 nm) up to 20 μm . For the 1.00 ml/min sample, small clusters were observed in the range of few particles up to 70 μm . Naoki et al. [127] reported similar results where they studied the effect of the spraying time on the uniformity of the deposited structure. They reported that the shorter the spraying time (a smaller spraying amount) resulted in an evenly coated surface with a uniform structure while the longer one resulted in a non-uniform, highly textured deposited layer [127].

Spraying condition:

T= 220°C D= 25 mm P= 0.25 kPa

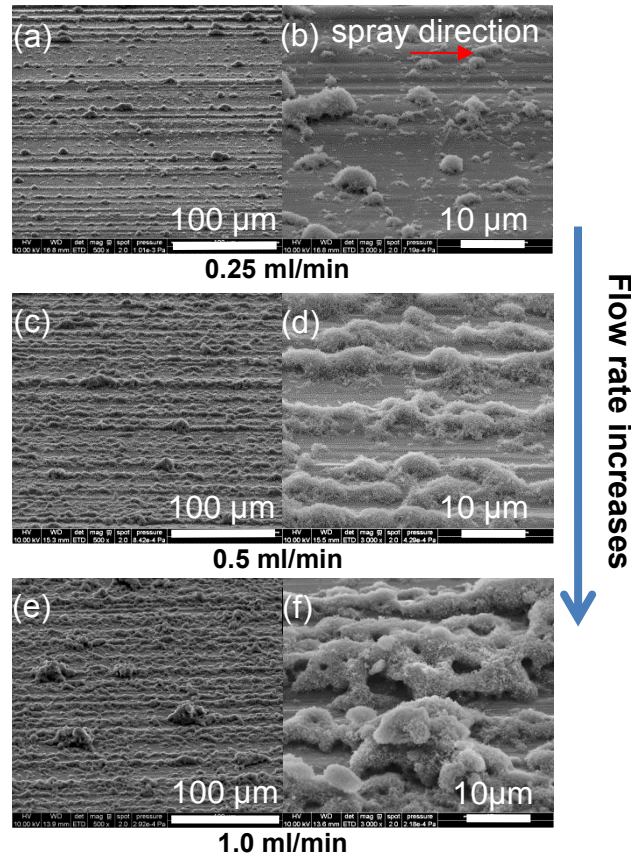


Figure 3.6 Effect of flow rate on the deposition structure (a, b) 0.25 ml/min, (c, d) 0.5 ml/min, and (e, f) 1.0 ml/min

As the flow rate increases, the deposited structure becomes more porous. In a typical spraying environment, the deposited structure is formed by the accumulation of the sprayed particles of each spraying pass. The morphology and texture of the dried deposited layer affect the drying dynamics of the successive sprayed layer [128]. When the dried deposited layer surface is rough (with high peaks and low valleys), the freshly deposited droplets dry on the peaks and do not fill the cavities on the surface due to the surface tension forming porous structures [127].

The effect of the deposition surface temperature is shown in Figure 3.7. The spraying was performed using a 0.1 wt.% SiC (80 nm)-ethanol suspension under an air pressure of 0.5 kPa, and with a suspension flow rate of 0.25 ml/min. At lower temperature, the suspension evaporation is slow and leads to agglomeration of the sprayed droplets. While evaporating, the nanoparticles begin to form larger clusters, which are continuous in the spraying direction and have lateral peripheral branches that grow perpendicular to the spraying direction as shown in Figure 3.7 (a) and (b). These peripheral branches are caused by fingering instability [125]. The instability occurs at the three phase contact line (gas, liquid, and particle) [129]. At higher temperatures, the evaporation rate is higher, thus leading to the reduction of the droplet size during travel [130]. A complete evaporation of relatively fine droplets may occur before they even reach the surface [131], which results in a loss of particles and prevents deposition. Moreover, the heated surface generates thermophoretic forces in an upward direction against the droplet movement. These forces contribute to the drag forces that hinder the droplet freefall and cause the droplets to deviate from their expected trajectory. For smaller droplets, the deviation from the droplet trajectory is greater than that of the relatively larger ones [86]. If complete evaporation occurs, the suspended particles do not have enough inertia to reach the substrate, and therefore, they are carried away from the substrate. The inertia of the traveling droplet needs to be above a critical value in order to overcome the thermophoretic forces and to be successfully deposited on the surface [81]. As seen in Figure 3.7 (e) and (f), the substrate is nearly free from any particle deposition at 255°C.

Spraying condition:

Q= 0.25 ml/min D= 25 mm P= 0.5 kPa

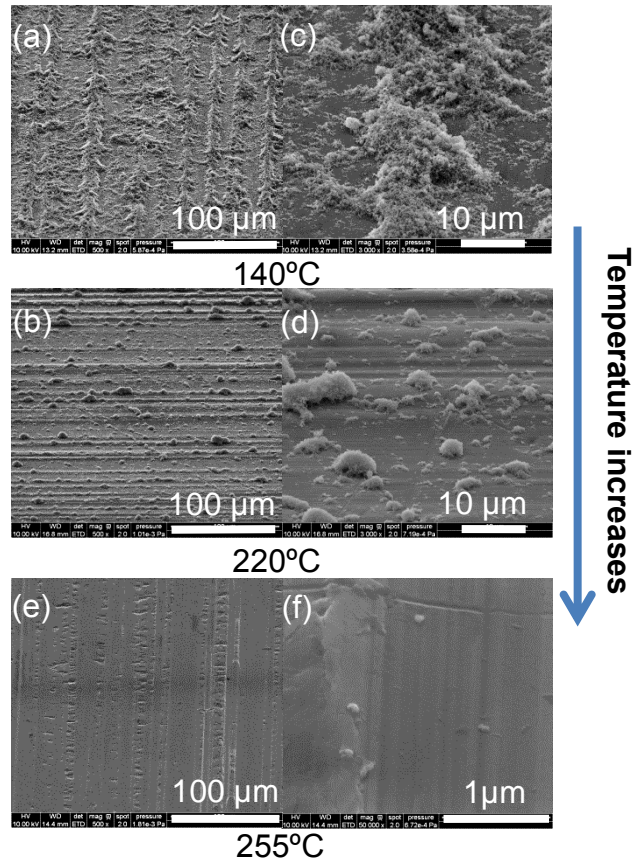


Figure 3.7 Effect of temperature on the deposition structure, (a, b) 140°C, (c, d) 220°C, and (e, f) 255°C

Figure 3.8 shows the effect of spraying air pressure on the deposited microstructure. The samples were sprayed using a 0.1 wt.% SiC (80 nm)-ethanol suspension at 220°C, with a suspension flow rate of 0.25 ml/min, and at air pressure settings of 0.25, 0.5, and 1.0 kPa. At the lowest air pressure (0.25 kPa), no SiC particles were observed on the substrate. This may be due to the lack of the force driving the nanoparticles to deposit on the substrate. As the droplet travels towards the substrate, the droplet velocity decays due to the air drag and thermophoretic forces [86]. At lower air pressure, the droplets take longer time to reach the substrate, which leads to partial or complete evaporation during travel. This can result in loss of particles as

discussed earlier. The sample sprayed under an air pressure of 0.5 kPa showed a wide range of nanoparticle cluster size distribution as shown in Figure 3.8 (a) and (b). As the air pressure increased to 1.0 kPa, only relatively larger nanoparticle clusters were present on the deposition surface, while smaller sized clusters were nearly absent. It is speculated that the violent air streams from higher air pressure blew away the weakly attached deposited clusters [127]. The nozzle distance from the deposition substrate had an effect similar to the effect of the air pressure. There was no deposition of nanoparticles if the nozzle was either too close ($D = 15$ mm) or far ($D = 50$ mm) from the substrate. As a result, only a limited nozzle distance range was available for each combination of spraying parameters.

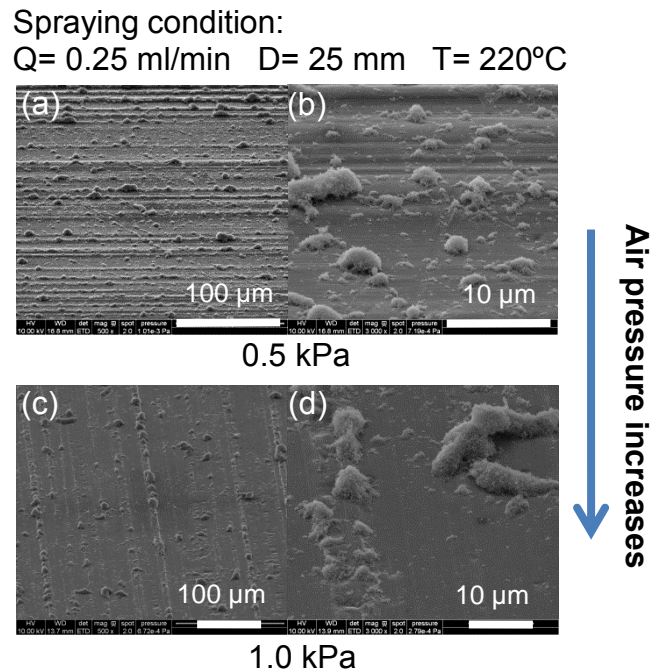


Figure 3.8 Effect of air pressure on the deposition structure, (a, b) 0.5 kPa and (c, d) 1.0 kPa

The potential of fabricating laminate composites reinforced with SiC nanoparticles via ultrasonic spraying was assessed by performing a three point bend test on synthesized

composites. The eventual deposited amount of SiC on the substrate was measured for the spraying condition used to fabricate the composites ($T=220^{\circ}\text{C}$, $P=0.5$ kPa, and $Q=0.25$ ml/min). A direct measurement of the deposited amount for each coupon, which requires 6-24 spray passes, was not possible since the amount deposited fell below the resolution of the balance (0.0001 g). For this reason, the suspension was sprayed for 200 passes on 10 coupons, and the average deposition per pass was determined [132]. The measured deposition amount per pass was 0.0255 g/m².

The flexural stress and strain were calculated from the measured force and displacement data using Eqns. (3.2) and (3.3) [39].

$$\sigma_{fl} = 3PL / 2wh^2 \quad (3.2)$$

$$\varepsilon_{fl} = 6d_c h / L^2 \quad (3.3)$$

σ_{fl} and ε_{fl} are the flexural stress and flexural strain, respectively. P is the load, L is the support span, w and h are the width and depth of the specimen, respectively, and d_c is the deflection at the middle of the span.

The measured flexural stress and strain curves of the Al6061-SiC composites are plotted in Figure 3.9 along with the reference Al6061 unsprayed but processed at the same condition. In general, the strength of the reinforced composite increased with the addition of the SiC nanoparticles, while the ductility was unchanged. For the Al6061-0.3 wt.% SiC, the yield and the ultimate flexural strength increased by 32% and 15%, respectively. That can be attributed to the local reinforcement of the composite at the interfaces of the consolidated sheets. The presence of the soft ductile zones separating the reinforced hard zones helped to preserve the ductility of the composite. Unfortunately, the SiC loading percentage, using the spraying process

is limited; only, a very small amount can be sprayed at the surface. When the SiC loading increased to 0.6 wt.%, no further increase in the strength was noticed. Upon spraying more SiC, the thicker layer hindered the bonding of the foils and resulted in lower mechanical properties [30, 36]. Samples were prepared with high loading percentages

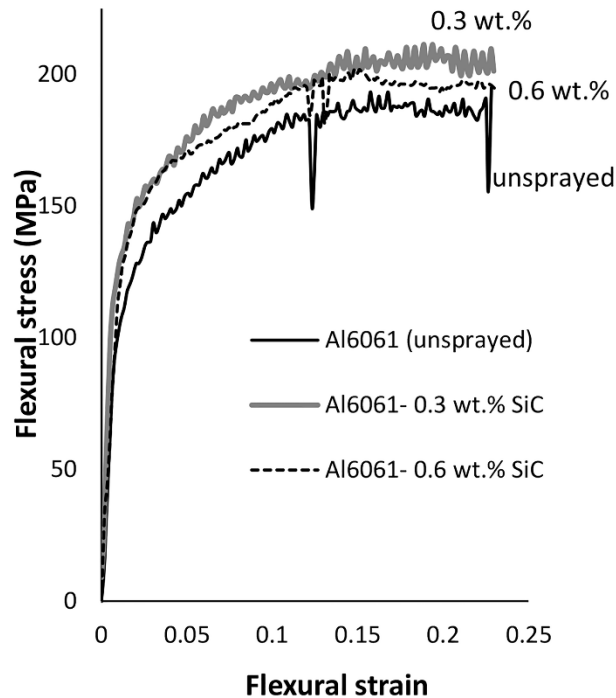


Figure 3.9 Effect of SiC loading on the flexural stress – strain curves of Al6061-SiC composites

The fracture surfaces of the Al6061-SiC composites were examined under the SEM. In Figure 3.10, the SiC reinforcement layers from the fracture surfaces of the Al6061-SiC composites are presented. For the Al6061-0.3 wt.% SiC composite, Figure 3.10 (a) shows that the SiC particles have been bonded. It is speculated that the SiC particles are fused by the liquid phase from the Al6061 that penetrated through the particles during consolidation. For the Al6061-0.6 wt.% SiC composites, a few regions were observed with SiC particles that did not consolidate and were still granulated as shown in Figure 3.10 (b). As the thickness of the SiC

nanoparticle layer increases, liquid phase penetration into the SiC particles becomes more difficult. The bond is strong where the liquid phase penetration is present and weaker beyond the penetration limit.

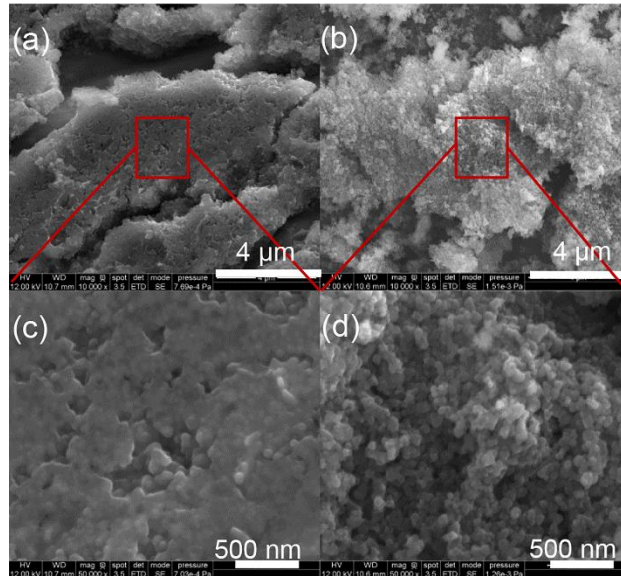


Figure 3.10 SEM images of SiC reinforcement layer on the fracture surfaces of (a, c) Al6061-0.3 wt.% SiC composite; (b, d) Al6061-0.6 wt.% SiC composite

Figure 3.11 (a) and (b) show the fractured Al6061 surface corresponding to the delaminated reinforcement surface for the Al6061-0.3 wt.% SiC and Al6061-0.6 wt.% SiC samples, respectively. Both composites showed the presence of ductile dimples on the Al6061 surface, which indicated formation of a robust bond at the interface and the mechanical load was transmitted.

Comparing Figure 3.11 (a) with Figure 3.11 (b), the 0.6 wt.% SiC sample still had pieces of the reinforcement particles attached in the vicinity of the ductile dimples. On the other hand, the fractured Al6061 layers of the 0.3 wt.% SiC composite were mostly free of the reinforcement particles. The observation indicated that the delamination may have occur through the weakly

bonded reinforcement region for the 0.6 wt.% SiC composite. In addition, submicron-size ductile dimples were also observed on the surfaces of the fractured SiC reinforcement layer on both samples, the 0.3 wt.% SiC and the 0.6 wt.% SiC, which are shown in Figure 3.12.

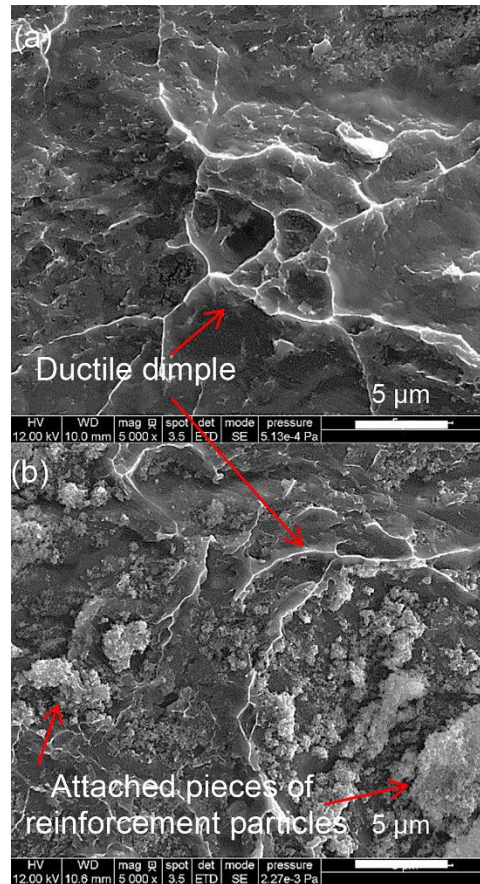


Figure 3.11 SEM images of Al6061 layer on the fracture surfaces of (a) Al6061-0.3 wt.% SiC composite; (b) Al6061-0.6 wt.% SiC composite

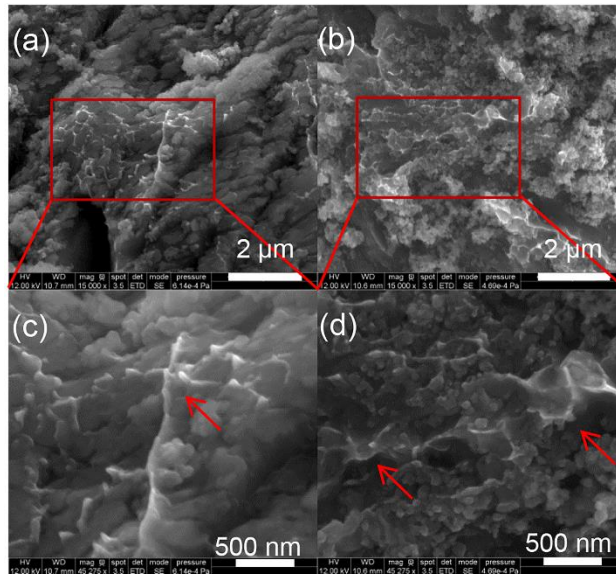


Figure 3.12 SEM images of reinforcement layer on the fracture surfaces of (a, c) Al6061-0.3 wt.% SiC composite; (b, d) Al6061-0.6 wt.% SiC composite

Figure 3.13 shows the flexural strength and strain of the consolidated samples with different SiC (80 nm) loadings (0.15–0.6 wt.% SiC). The samples were sprayed at 220°C, with a flow rate of 0.25 ml/min under a pressure of 0.5 kPa and from a distance of 25 mm. The addition of SiC at the interface between the consolidated layers increased the yield strength of the composite. The ultimate flexural strength, however, was only marginally improved compared with the unreinforced sample. The SiC reinforcement strengthened the composite until the yield, but did not change the hardening behavior since it was primarily governed by the AZ31 substrate material properties. An excessive amount of SiC loading at the interface resulted in degradation of mechanical properties as observed for 0.6 wt.% SiC sample in Figure 3.13. Too thick of a layer of SiC nanoparticles prevented bonding of the AZ31 sheets.

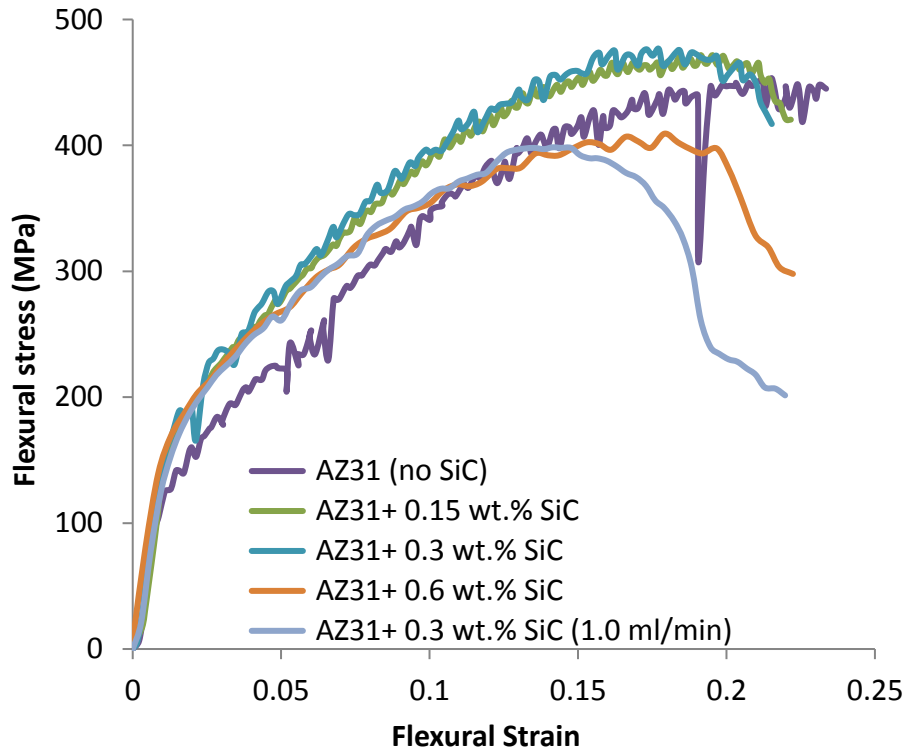


Figure 3.13 Flexural stress-strain curves of the consolidated AZ31-SiC composites

To compare the effect of the deposition layer morphology on the mechanical properties of the composite, a sample was synthesized with high flow rate (1.0 ml/min) while the other parameters were kept the same. Such spraying conditions led to a nonuniform layer with large porous nanoparticle clusters (see Figure 3.6), and the synthesized composite showed poor mechanical properties (see Figure 3.13). As mentioned in earlier discussion, a high flow rate resulted in the formation of large SiC clusters and a highly porous deposition microstructure. The large clusters introduced uneven distribution of nanoparticles at the interface, and porous sites may act as crack nucleation points, which contribute to early failure of the composite.

3.4 Conclusions

In this study, the dispersion and control of the deposited SiC nanoparticles were investigated using the ultrasonic spraying process. The ultrasonic spray deposition is governed by the suspension properties and the spraying parameters. The conclusions from this work can be summarized as the following:

- The atomization droplet size was largely affected by the nozzle vibration frequency while the suspension parameters only had a limited influence. According to Eqn (1), The change in suspension concentration up to 16 wt.% SiC only resulted in droplet size variation of approximately 1 μm .
- The deposited nanoparticle cluster size and morphology were affected by two main factors: the driving force that transports the atomized droplet from the nozzle to the substrate, and the evaporation behavior of the droplet (the amount of liquid phase present on the substrate and its evaporation rate). The amount of the liquid phase on the substrate and its evaporation rate were determined by the flow rate and the deposition surface temperature. The driving force is mainly determined by the air pressure and the nozzle to substrate distance.
- Having a large amount of liquid phase present on the substrate and low evaporation rate increased the nanoparticle cluster size and resulted in nonuniform deposition microstructure. Although a minimum inertia for the droplet is required for deposition of nanoparticles, violent air streams may destruct the deposited structure.
- The use of ultrasonic spraying of nanoparticles showed a promising potential to fabricate laminate composites. AZ31-0.3 wt.% SiC composites with uniformly deposited microstructure at the interface showed an improvement in the flexural yield strength by 49% compared with the

unreinforced AZ31, while composites with nonuniform structure or thicker deposition layer exhibited deterioration in mechanical properties.

CHAPTER 4 FABRICATION OF PATTERN REINFORCED AZ31 MULTILAYER COMPOSITE USING ULTRASONIC SPRAY DEPOSITION

4.1 Introduction

The outstanding mechanical behaviors of natural biological materials, such as wood, bones, shells, bird beak, etc., have attracted the interests of many researchers [29, 133-136]. The properties of these biological composites are often superior to the theoretically averaged properties of its constituents [136] due to their complex multiscale structures. A multilayer structure with controlled interface, structural gradients, hierarchical structures may yield a combination of favorable properties in strength, hardness, damage control, and fracture toughness, which cannot be obtained in conventional composites by simply dispersing particles or fibers [2, 137]. Many numerical testing and modeling work have been conducted to evaluate, optimize, and investigate hierarchical composite structures [1-5]. One of the biomaterials known for the strength and toughness is the nacre of a sea shell, which consists of multilayers of brick-and-mortar structure. The deformation mechanism of the nacre has been studied by several researchers [138, 139]. Some of its key structural characteristics that allow extraordinary strength and toughness despite the brittleness of its constituents are the layered brick-and-mortar configuration, the interlocking behavior between the platelets, the nanostructure within the platelets [138], and the structured interfaces with interpenetrating, gradient nanostructure [7]. In a recent study, Mishnaevsky et al. conducted a computational micromechanical study on the effects of nano-engineered interfaces in biocomposite materials on mechanical properties [7] and concluded that nanostructured interfaces is a promising approach to tailor the material deformation and mechanical properties.

Metal matrix composites (MMCs) produced nowadays have been limited to rather simple structures of dispersing reinforcing particles or fibers in the matrix phase. The traditional fabrication routes for MMCs, such as milling and blending [14-18], powder metallurgy [19-23], melt processing [24-26], and others [27, 28], are not capable of creating such complex hierarchical structures. A more versatile, flexible, scalable manufacturing method is needed to realize such sophisticated designs in MMCs [29].

In this study, a unique fabrication method that used ultrasonic spraying to deposit microscale patterns on sheets was developed to create custom structures in MMCs. Various techniques have been used in material coating or surface deposition, such as tape casting [75], thermal plasma spraying [77], electrostatic spray deposition [78], spray deposition [79], and ultrasonic spray deposition [81]. Among those techniques, ultrasonic spraying offers several unique characteristics. The ultrasonic spraying nozzle vibrates at high frequency using two piezoelectric discs and an amplifier. This makes the liquid leave the nozzle tip in the form of mist that has a narrow droplet size distribution and a very low spraying velocity in the order of 1 m/s compared with other spraying techniques [82], which help control the spatial distribution of deposited particles as well as the deposition structure [140, 141]. The technique also allows accurate control of the deposition rate [86] and deposition structure [81, 87]. In a recent study by Bastwros and Kim, ultrasonic spraying was used to deposit SiC nanoparticles on AZ31 foils to fabricate laminate composites [141]. A considerable enhancement in the yield strength was reported compared with the unreinforced layered AZ31.

In this study, an AZ31 composite panel with custom pattern reinforcement structure has been fabricated with an ultrasonic spraying method. The panels consist of multilayer of AZ31 foils with nanostructured micro-pattern reinforcements at the interface. The micro-patterns were

created by spraying through a mask layer. After deposition, the foils were stacked and hot pressed in the semi-solid temperature range to consolidate into a composite panel. Three point bend test and small punch test (SPT) were performed to measure the mechanical properties of the composite. Nanoindentation and scanning electron microscopy analysis were used to evaluate the mechanical behavior and to analyze the chemical composition of the developed reinforcement phases.

4.2 Experimental procedures

An ultrasonic deposition system (Exacta-Coat Ultrasonic Coating System, Sono-Tek Corp.), as shown in Figure 3.1, was used to perform the spraying. The system features Sonic Syringe that provides bursts of vibration to prevent the suspended particles from sedimentation and agglomeration. The spraying parameters considered to study pattern deposition includes deposition surface temperature (T), spraying suspension flow rate (Q), spraying air pressure (P), nozzle vibration frequency (f), and the nozzle distance (D), which have been found to be important [81, 82]. A mask pattern was used to analyze the deposition of structures using spraying method. The spraying suspension was prepared by adding 80 nm SiC particles into ethanol with loading of 0.1 wt.% SiC. Figure 4.1 shows a schematic overview of the spraying process and the patterned mask used. The pattern holes are 200 μm in diameter with a total mask opening area of 20%. The suspension was sprayed for 5 min. The detailed spraying conditions and parameters are summarized in Table 4.1.

Table 4.1 Summary of the spraying parameters and their values

Parameters	Values
Reinforcement material	Nano SiC (< 80 nm)
Suspension medium	Ethanol + 0.1 wt.% SiC
Sonication time	6 hours
Temperatures (T)	160, 190, and 220°C
Flow rates (Q)	0.25, 0.5, and 1.0 ml/min
Air pressure (P)	0.25, 0.5, and 1 kPa
Distance (D)	20, 25, and 30 mm
Spraying speed (V)	0, 1, 5, 10 mm/s
Spraying time (t)	5 min
Nozzle frequency (f)	120 kHz

A nanoparticle suspension with a mixture of 0.05 wt.% SiC nanoparticle (80 nm) and 0.015 wt.% Al6061 particles (1.73 μm) was prepared for spraying to fabricate the composite. The suspension was prepared using ultrasonic bath. The sonication was performed in two steps. In the first step, each particle specie was suspended and dispersed separately in an ultrasonic bath for 6-8 hours. Then, they were mixed and sonicated for another 4-6 hours prior to spraying. The spraying parameters that were used are as follows: deposition surface temperature (T) = 190°C, spraying suspension flow rate (Q) = 0.25 ml/min, spraying air pressure (P) = 0.5 kPa, nozzle to substrate distance (D) = 25 mm, and a spraying nozzle speed (V) = 5 mm/s [141]. The spraying was performed through a mask with the desired pattern to deposit the particles on the AZ31 foils. The detailed spraying conditions and parameters are summarized Table 4.2.

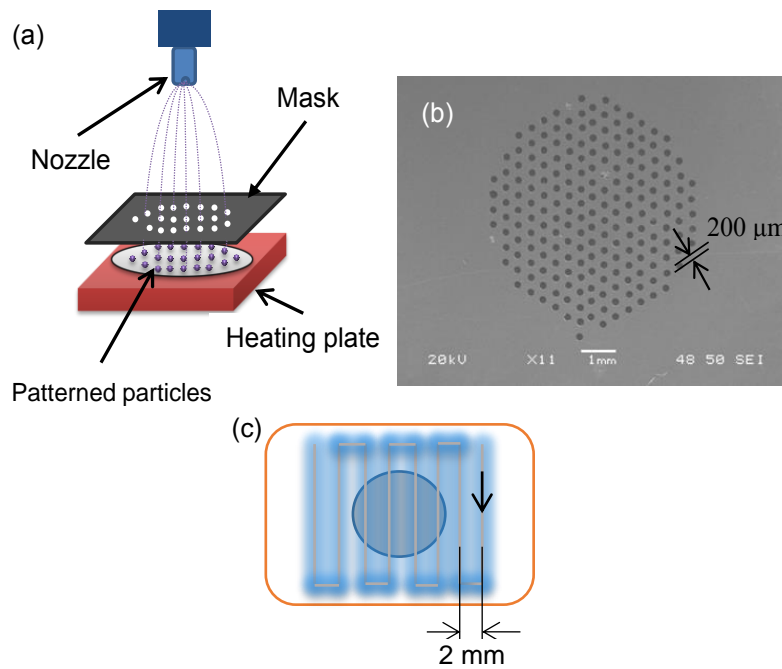


Figure 4.1 (a) Schematic overview of the spraying process, (b) patterned mask, and (c) spraying path

After spraying the SiC and Al6061 particles on coupons of AZ31 foils, the coupons were stacked together and consolidated. The AZ31-SiC/Al6061 composite panel comprised 14 layers of AZ31 foils ($\sim 100 \mu\text{m}$ thick) with sprayed patterns at the interfaces. The chemical composition of the AZ31 foil is provided in Table 3.2.

The experimental setup used for composite synthesis is shown in Figure 2.1. The die was made of H13 tool steel and was lubricated by spraying a thin layer of boron nitride to prevent potential reaction between the material and the die at elevated temperatures. The consolidation was performed in two stages. First, the sheets were stacked together and pre-compacted at 100 MPa, and then a pressure of 50 MPa was applied on the sample during heating and consolidation of the sample. The sample was heated to 610°C and then held for 20 min. The liquid phase percentage at this temperature is approximately 9%.

Table 4.2 Summary of the spraying parameters and their values for composite fabrication

Parameters	Values
Nanoparticles	Nano SiC (< 80 nm), Al6061 (1.73 μm)
Suspension medium	Ethanol + 0.05 wt.% SiC + 0.015 wt.% Al6061
sheet thickness	90-100 μm
Temperatures (T)	190°C
Flow rates (Q)	0.5 ml/min
Air pressure (P)	0.5 kPa
Distance (D)	25 mm
Spraying speed (V)	5 mm/s
Number of spraying passes	25 pass
Nozzle frequency (f)	120 kHz

Two different tests were used to evaluate the mechanical behavior of the fabricated composites: the three point bend test and SPT. For the three point bend test, the synthesized composites were cut using a diamond saw and were polished to the final dimensions of 0.9 mm in thickness and 1.2 mm in width. The flexural stress and strain were recorded using the materials testing system. The SPT was carried out using an experimental device as shown in Figure 4.2, which was mounted on a universal testing machine. The experimental setup included the disc specimen, a 6 mm diameter ceramic ball, and a specimen holder that consisted of an upper and lower die on which the sample was placed and centered. The sample was placed between the upper and lower dies and tightened uniformly with clamping screws. The crosshead speed was 0.2 mm/min, and the values of the load and cross head displacement were recorded simultaneously over time.

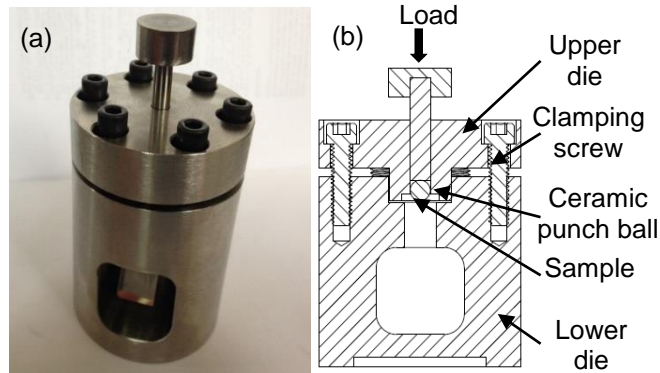


Figure 4.2 Small punch test (a) small punch test setup, (b) cross sectional view of the SPT

Scanning electron microscope (FEI Quanta-250 field-emission scanning electron microscope) and energy dispersive spectroscopy (EDS) technique were used to examine the pattern deposition (before consolidation) and the fracture surface. Nanoindentation was used to estimate the mechanical properties of the reinforcement phase.

4.3 Results and discussion

4.3.1 Nanoparticle deposition

The spraying parameters significantly influence the deposition structure of the nanoparticles. The critical ones are the deposition surface temperature (T), spraying suspension flow rate (Q), spraying air pressure (P), and the nozzle to substrate distance (D) [81, 82]. In the previous study by Bastwros and Kim [141], the effects of those parameters on the deposition structure were investigated to fabricate layered composite with uniform spraying without the mask pattern. In this work, the effect of these parameters and the spraying traveling speed (V) on the pattern deposition is investigated.

The effect of the flow rate on the deposited structure is shown in Figure 4.3. The samples were sprayed at flow rates of 0.25–1.00 ml/min while other parameters were held constant. As the flow rate increased, the amount of liquid phase transported during spraying was higher,

resulting in a longer evaporation time. Therefore, at higher flow rate, the pattern totally disappeared due to the remnant liquid phase ethanol that did not evaporate and accumulated on the substrate [81]. The liquid phase ethanol sipped into the gap between the mask and substrate destroying the pattern structure. At lower flow rates, the patterns were well defined, but the deposited layer was thin.

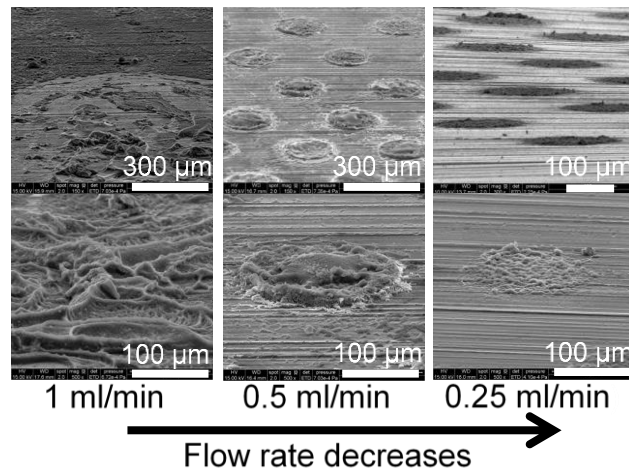


Figure 4.3 Effect of flow rate change on the deposition structure with spraying condition at $T=190\text{ }^{\circ}\text{C}$, $D=25\text{ mm}$, and $P=0.25\text{ kPa}$

Figure 4.4 shows the effect of the temperature on the deposited structure. The temperature range tested was $160\text{--}220\text{ }^{\circ}\text{C}$. At the higher temperature ($220\text{ }^{\circ}\text{C}$), the ethanol evaporated before it reached the substrate resulting in loss of nanoparticles [81]. Moreover, the heated surface generates thermophoresis forces in upward direction against the droplet movement. These forces add to drag forces that hinder the droplet freefall and cause the droplets to deviate from their trajectory. For smaller droplets, the deviation from the droplet trajectory is greater than that of the relatively larger ones [128]. If complete evaporation occurs, the suspended particles do not have enough inertia to reach the substrate [131], and therefore, they are carried away from the substrate. However, the pattern was more uniform and denser

compared with the structure deposited at lower temperatures. At the lower temperature (160°C), the ethanol did not evaporate until it reached the substrate. The resulting structure showed that some SiC nanoparticles were carried under the mask layer causing deposition outside the pattern area. The temperature should be selected such that the ethanol evaporates immediately after delivering the nanoparticles on the substrate for precise pattern formation. Substrate temperature is considered very important for final film morphology and should be higher than the boiling temperature of the suspension liquid [94].

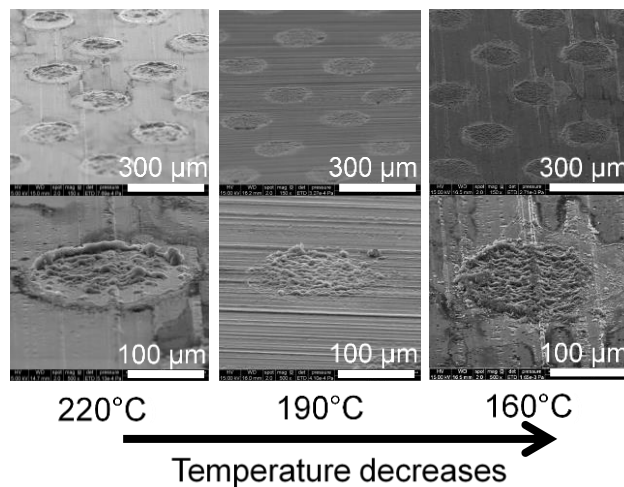


Figure 4.4 Effect of temperature change on the deposition structure with spraying condition at $Q=0.25$ ml/min, $D=25$ mm, and $P=0.25$ kPa

Figure 4.5 shows the effect of air pressure on the deposited structure. The samples were sprayed at different air pressures of 0.25, 0.50, and 1.0 kPa. At the lowest air pressure (0.25 kPa), uniform structure and pattern formation was observed, but the structure was not as dense as structures obtained at higher pressures. It may be due to the lack of driving force to deposit the nanoparticles through the mask. As the droplet travels towards the substrate, the droplet velocity decays due to the air drag and thermophoresis forces [128], and evaporation

occurs which can cause loss of particles [94]. The inertia of the traveling droplet needs to be above a critical value in order to overcome the thermophoresis forces and to be successfully deposited on the surface [81]. As the air pressure increased, higher amount of accumulation and densification were observed. However, at the highest pressure (1.0 kPa), the violent air stream destructed the deposited structure [127].

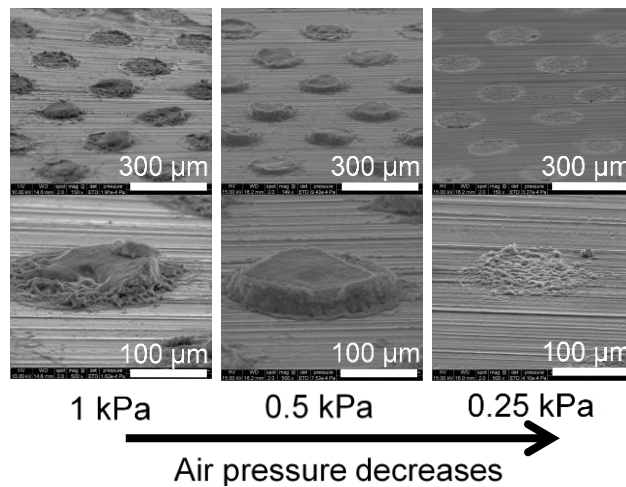


Figure 4.5 Effect of air pressure change on the deposition structure with spraying condition at $T=190\text{ }^{\circ}\text{C}$, $Q=0.25\text{ ml/min}$, and $D=25\text{ mm}$

Figure 4.6 shows the effect of spraying distance (nozzle tip to substrate distance) on the deposited structure. The samples were sprayed from different spraying distances: 20, 25, and 30 mm. For the 30 mm and 25 mm samples, the structures are comparable. For the 20 mm sample, the pattern was not uniform, and some of the particles were found between the patterns. That could be attributed to the violent force of the air stream, which destroyed the deposited structure by partially flushing the previously deposited particles and spreading them randomly on the substrate [127].

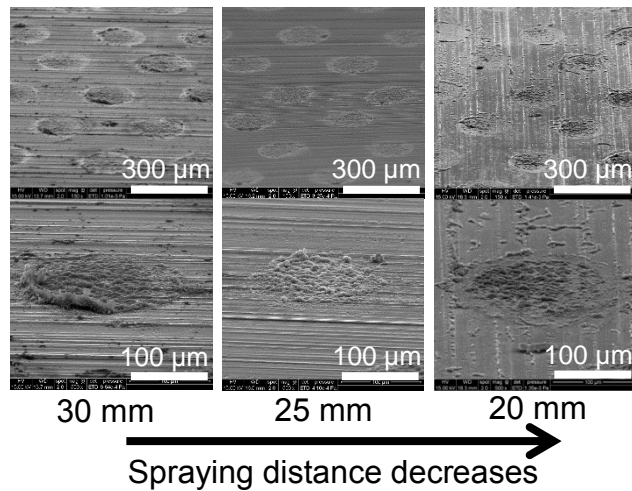


Figure 4.6 Effect of spraying distance change on the deposition structure with spraying condition at $T=190\text{ }^{\circ}\text{C}$, $Q=0.25\text{ ml/min}$, and $P=0.25\text{ kPa}$

A suspension with a mixture of 0.05 wt.% SiC nanoparticle (80 nm) and 0.015 wt.% Al6061 particles (1.73 μm) was sprayed using different spraying nozzle speeds. Figure 4.7 shows the effect of spraying speeds on the deposited structure. There are three speeds that were used: 1, 5, and 10 mm/s. For the slow spraying speed (1 mm/s), the deposited pattern was present on the substrate, but some of the sprayed particles were carried under the mask resulting in deposition outside the pattern holes. In addition, considerable amount of segregation of the sprayed particles was observed along the periphery of the patterns. This may be due to the large amount of liquid phase present on the foil surface [141], where the air flow may transport nanoparticles towards the periphery and trap them until suspension is evaporated [140].

Spraying condition:

Q= 0.5 ml/min D= 25 mm P= 0.5 kPa T= 190°C

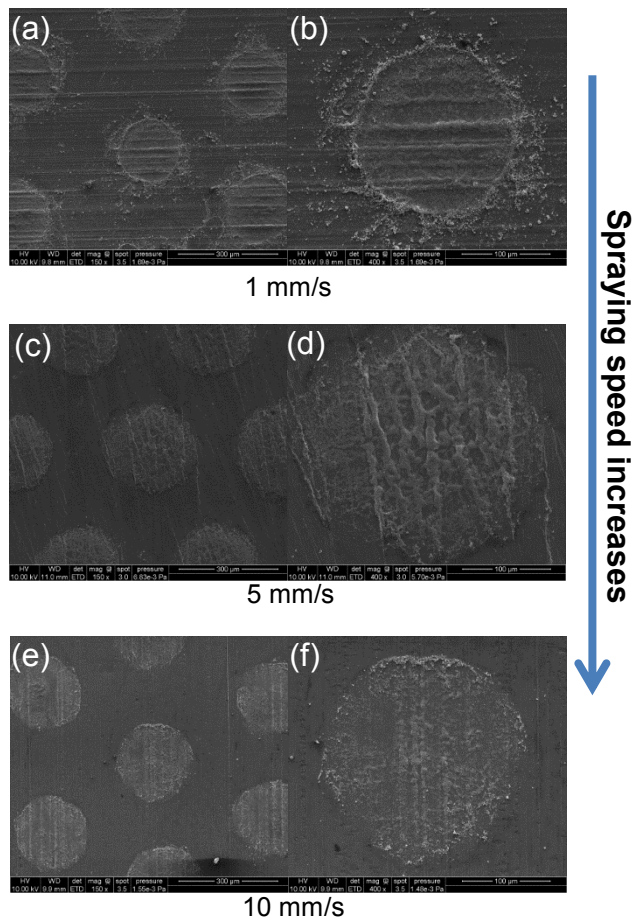


Figure 4.7 Effect of spraying speed on the deposition structure, (a, b) 1 mm/s, (c, d) 5 mm/s, and (e, f) 10mm/s

When the spraying nozzle speed is increased to 5 mm/s, the deposited pattern was acceptable with well-defined patterns and with fewer particles carried between the patterns. An equilibrium state was reached between the amount of liquid phase that reach the surface and the evaporation caused by heating the plate temperature [81]. Increasing the spraying speed up to 10 mm/s resulted in a well-defined pattern but with a minor clustering at the periphery of some of the patterns in the spraying direction. Both 5 and 10 mm/s settings may be used for spraying a well-defined pattern.

In Figure 4.7, the deposition structure of the pattern, Level 1, has been confirmed. The nanostructure of pattern feature, Level 2, was examined to confirm the mixing and dispersion of its constituents (SiC and Al6061 particles). Figure 4.8 shows SEM image of the deposited particles using the spraying parameters mentioned in Table 4.2. In addition, elemental analysis of the deposited structure was conducted using EDS to locate Mg, Si, and Al. The Al6061 particles are well dispersed within the SiC particles. Theoretically, the ratio between the weight of the SiC particles and the Al6061 particles is 3:1. The EDS map of Al content (Figure 4.8 (b)) shows less amount of Al present. This may be due to either the Al6061 particles are covered by SiC particles or its amount is relatively small to be detected by the detector.

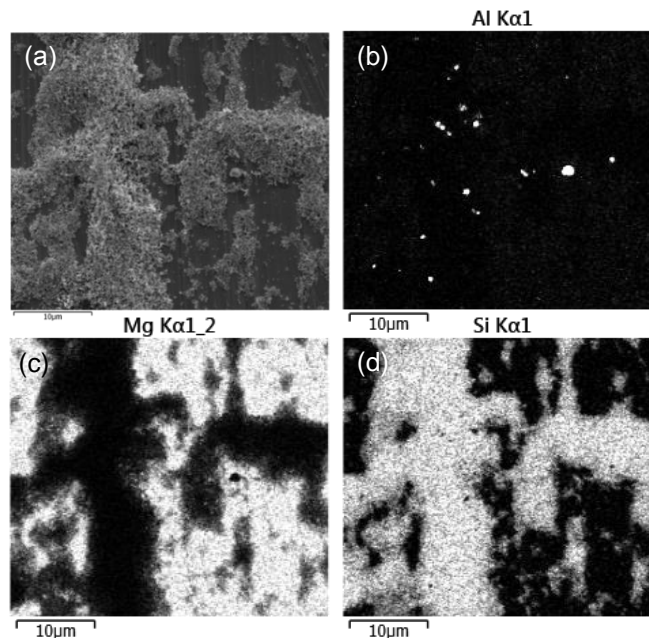


Figure 4.8 (a) SEM image of AZ31 substrate sprayed with SiC/Al6061 particles, (b) EDS map of Al distribution, (c) EDS map of the Mg distribution, and (d) EDS map of the Si distribution

4.3.2 Composite consolidation

After the spray deposition of the patterns on the AZ31 coupons, a layered composite was prepared by stacking the coupon together and consolidating them. The AZ31 sheets have an average thickness of 100 μm . The SiC/Al6061 particle mixture was sprayed using the spraying condition summarized in Table 4.2. The spraying with the mask resulted in the SiC particle loading of approximately 0.12 wt.% SiC and 0.04 wt.% Al6061.

The three point bend test results are shown in Figure 4.9 for the AZ31 (layered, no pattern, unsprayed) and AZ31 composite with patterns. The behavior of the sprayed composite showed an increase in the strength compared with that of the unsprayed AZ31 sample. The flexural yield and ultimate strength of the patterned sample increased by 75% and 18% compared with the unreinforced sample, respectively.

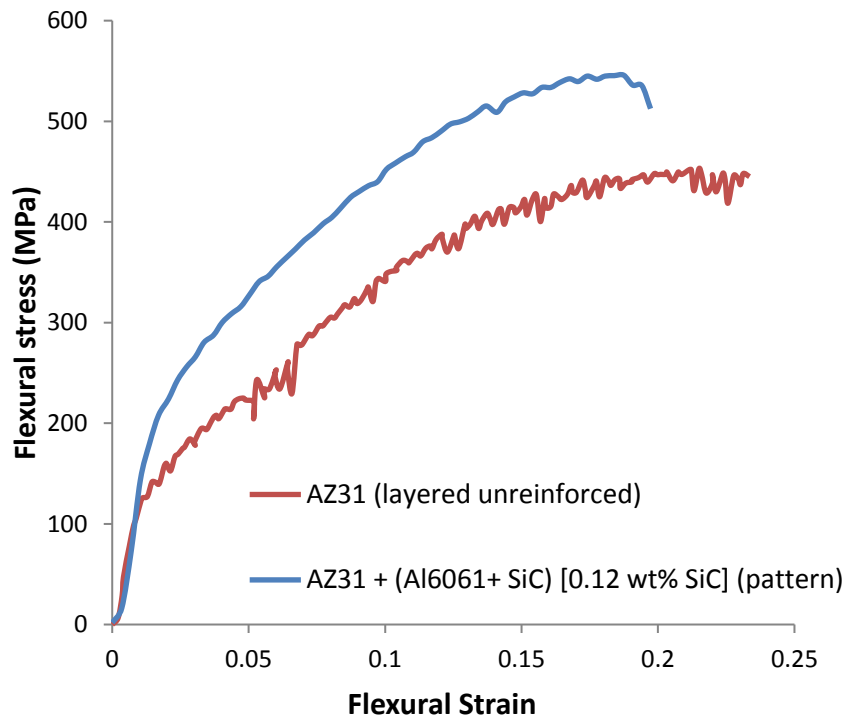


Figure 4.9 Flexural stress-strain curves of the consolidated samples

It is speculated that the strength increase in the patterned composite may be due to the combined effect from the pattern reinforcement and its interaction at the interface. Although the shape and spacing differ from the brick-and-mortar structure in nacre, some insights may be obtained from the analysis. The brick-and-mortar structure under tensile loading follows load transfer path of the tension-shear chain, where the hard, reinforcement patterns are under tension and the relatively soft matrix is under shear [134]. This configuration allows better distribution of the stresses and deformation within the composite, which have better utilization of the maximum properties of the components [142]. Once the damage initiates, the crack propagates until it reaches an interface, either the AZ31/AZ31 interface or the AZ31/reinforcement. Depending on the interface characteristics, the crack may either deviate trying to find a weaker path to propagate or may be arrested until the stress level increases to allow the crack to overcome the interface barrier [113]. The debonding of the interface and the shearing of the soft phase (matrix) during the crack propagation help to increase the fracture energy absorption during the deformation [7]. Moreover, the interlocking behavior between the reinforcement phase and the matrix increase the composite strength and toughness.

After the three point bend test, the sample was manually bent until fracture to analyze the fracture surface. Figure 4.10(a) shows a lower magnification of the fracture surface. Local debonding is shown between the layers caused by shearing along the interface [133]. The crack propagate under tensile stresses (mode I) passing across the AZ31 layer until it hits an interface. If the interface is strong enough, the crack path deviate and propagate under shearing stresses (mode II) through the weak zones along the interface until the stress level allows the crack to propagate across the layer again. The additional shear component makes the crack path deviates from original direction increasing the travel path, which increases the absorbed fracture energy

during deformation [113, 133]. An in-depth analysis of the fracture surface was performed under the SEM to locate the pattern structure after consolidation as shown in Figure 4.10(b) at higher magnification. Using EDS, the elemental map of Al, Si, and Mg for the surface was constructed. By matching the Si map with the SEM image, the reinforcement pattern was partially located surrounded by an unreinforced zone, which supports that the pattern was not destroyed during stacking, compaction, or sintering. Al was not detected at this magnification because the Al amount was relatively small compared with the SiC and the AZ31 that represent the background signal.

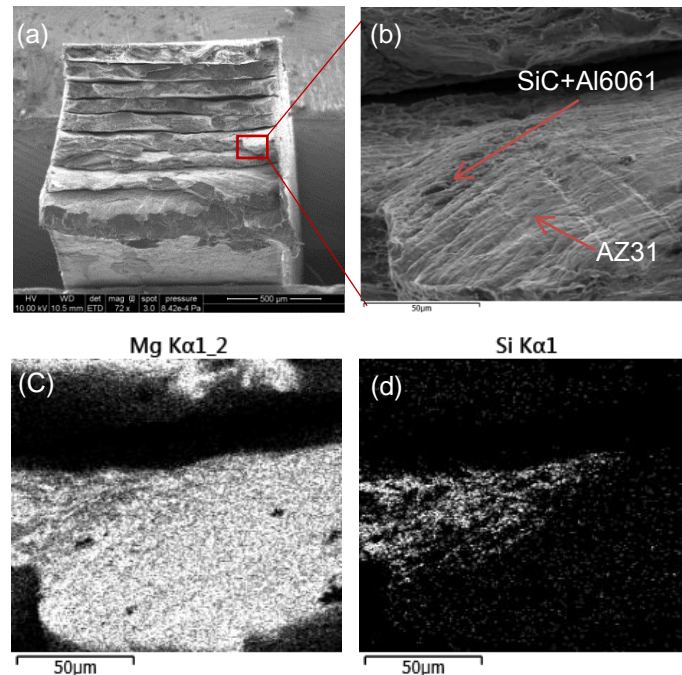


Figure 4.10 Patterned composite fracture surface (a, b) SEM image of fracture surface, (c) EDS map of the Mg distribution of SEM image “b”, and (d) EDS map of the Si distribution of SEM image “b”

At the higher magnification of the fractured surface, Figure 4.11 shows the reinforcement zone shown in Figure 4.10(b) and the corresponding Al, Si, and Mg elemental EDS map. The

maps clearly locate the Si and the Mg element and locate the Al content as well but with some signal noise as the Al is included in AZ31 alloy composition. The Al and Si match well, and the Mg map agrees well with the darker spots in the Si map. These zones are marked on the SEM image in Figure 4.11(a). It can be seen that the reinforcement zone fractured into discrete pieces but is still attached to the AZ31 surface, which may indicate a gradual failure at the interface. In addition, ductile dimples are observed on the AZ31, which shows that there is considerable bonding between the reinforcement phase and the AZ31 layers to allow load transfer [140].

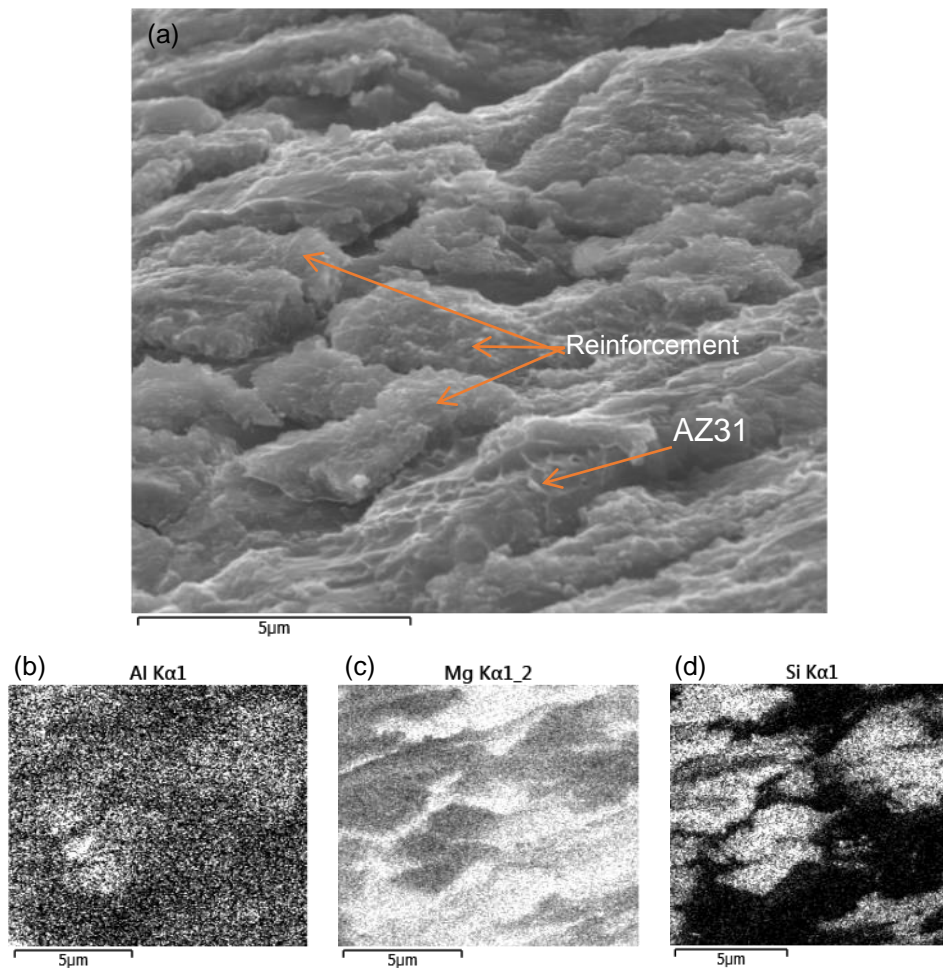


Figure 4.11 Fracture surface (a) higher magnification of the reinforcement phase, (b) EDS map of the Mg distribution, (c) EDS map of the Si distribution, and (d) EDS map of Al distribution.

Figure 4.12 shows an opened crack at the reinforcement zone on the fracture surface. It is noticed that the reinforcement phase is attached to the AZ31 surface. For the reinforcement layer, the fracture has an angle of 90° , which indicates a brittle fracture that cannot accommodate plastic deformation compared with the AZ31 phase.

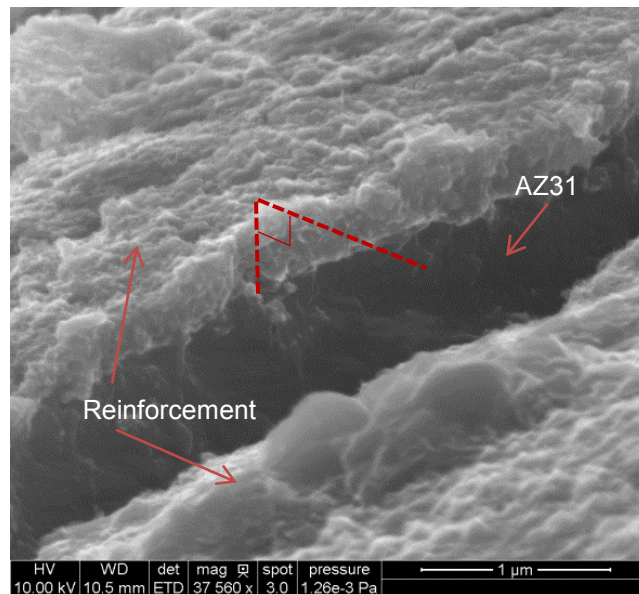


Figure 4.12 SEM image of the reinforcement layer attached to the AZ31 sheet.

The interpenetration of the AZ31 phase and reinforcement particles helps to generate a gradual transition of properties to avoid sharp interfaces. Examination of Figure 4.11 shows that the surface topography of both the AZ31 phase and the reinforcement phase is relatively rough (full of nano-asperities). Due to the nanostructure of reinforcement phase and the presence of the liquid phase (AZ31) during semi-solid sintering, the interface between the reinforcement and matrix phases is interpenetrating. The interpenetration of the AZ31 phase within the

reinforcement phase was also detected by the EDS as shown in Figure 4.13. This may generate additional resistance to the crack propagation by dissipating additional energy at the interface through debonding and shearing of these nano-asperities. Mishknaevsky et al. suggested that the structured interfaces with interpenetrating, gradient nanostructures increase the toughness of biomaterials [7]. Katti et al. simulated the nano-asperities in the platelets/biopolymer interfaces in the nacre. They reported marginal effect on the mechanical properties [143]. Song and Bai reported that these interpenetrating interface reinforce the weak interfaces in the nacre and control the crack propagation at the interfaces [144].

4.3.3 Reinforcement phase properties

To evaluate the composition and mechanical properties, a sample was prepared to conduct EDS analysis and to perform nanoindentation test at the reinforcement zone. The sample is composed of two AZ31 coupons sprayed with SiC/Al6061 particle mix at the interface. The SiC/Al6061 particle mixture was sprayed at same spraying condition as described earlier. One coupon was sprayed for 50 passes and covered with another one. The two coupons were stacked together and consolidated under the same condition as described earlier.

The sample was cut in the thickness direction using a low speed diamond saw. The sample was then molded and mirror polished to perform the EDS analysis. EDS was performed using a line scan across the reinforcement phase zone to detect the change in the concentration of different elemental species (Figure 4.13). The interface had a thickness of about 4 μm . The matrix is mainly rich of Mg, Al, and Zn while the interface is rich of Si, C, and Al. It can be seen that the Mg is present even at the middle of the reinforcement zone indicating that the liquid phase penetrated and diffused through the deposited nanoparticles during consolidation. This increased the bond between the SiC nanoparticles. Moreover, the Si that reflects the SiC content

was absent in the AZ31 phase and gradually increasing near the interface. Both the Al (from Al6061) and the C (from SiC nanoparticles) concentrations were low and did not change at the interface, which could be due to their small amounts present on the surface. From the EDS analysis, the reinforcement phase composition concentration can be estimated to be 62% and 33.3% of AZ31 and SiC phase, respectively.

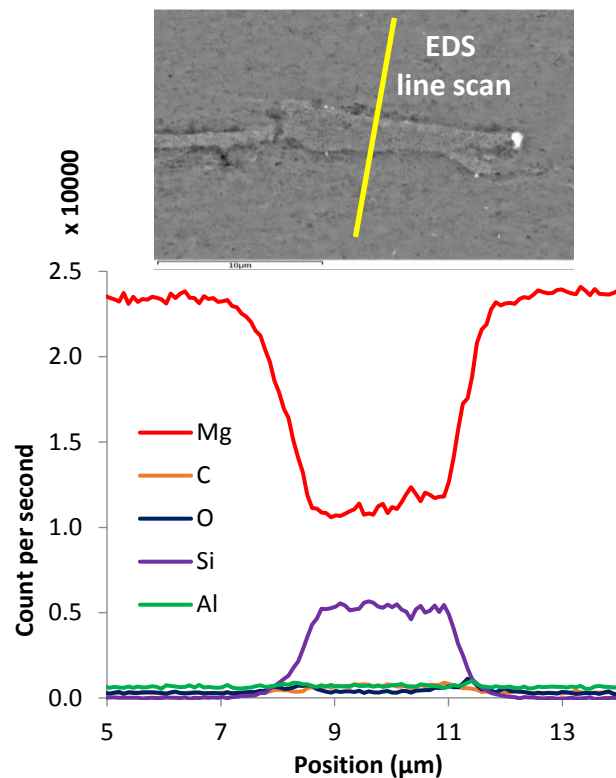


Figure 4.13 EDS line scan across the interface between two AZ31 foils, and elemental diffraction intensity along the line scan with respect to the position on the scanned line

The reinforcement zone thickness was too small to perform either a macro or a micro-hardness test, and therefore nanoindentation test was performed to predict the mechanical properties of the reinforcement phase. The test was conducted for both the reinforcement zone and the AZ31 phase. Although the interface was still relatively small to predict accurate

mechanical properties, a relative estimation of the reinforcement and the AZ31 phase can be provided. The nanoindentation was performed using a quartz cube corner tip indenter. Figure 4.14 shows the AFM images of the surface before and after one of the indentation of both AZ31 zone and the reinforcement zone.

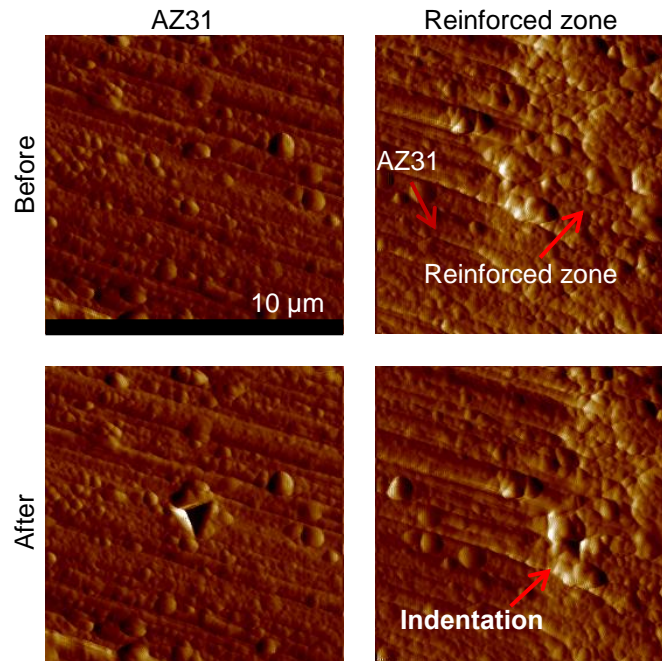


Figure 4.14 AFM images of the surface topography before and after indentation: (a) AZ31 zone before indentation, (b) interface zone before indentation, (c) AZ31 after indentation, and (d) interface after indentation

The relative hardness and bulk modulus of the interface with respect to the AZ31 were averaging 1.9 and 1.5, respectively. As a result the interface hardness and bulk modulus will be approximately 114 HV (1.123 GPa) and 75 GPa, respectively. As discussed earlier, the reinforcement zone consists of 66% of the matrix phase (AZ31) interpenetrated between the SiC and Al6061 particles, which have helped bond the SiC nanoparticles together and justify the relatively low mechanical properties of the reinforcement zone reported, compared to the SiC

particle properties. There is relatively small difference between the mechanical properties of the reinforcement zone and the matrix phase, which helped reduce the properties mismatch between both phases. The presence of large mismatch in the mechanical properties between the reinforcement phase and the matrix phase promote sharp transition of properties at the interface, which may affect the efficiency of the load transfer due to the premature interface failure [145]. Moreover, the interpenetration of the liquid phase (AZ31) between the reinforcement nanoparticles during sintering helped generate a gradual transition in the mechanical properties between the reinforcement zone and the matrix, which may have helped increase the strength and toughness of these composites by enhancing the load transfer efficiency between the reinforcement zone and the matrix [7].

4.3.4 Small punch test

The SPT was performed to confirm the mechanical strength enhancement of the patterned composite. The SPT exerts a biaxial loading condition to the sample where the sample will first experience bending followed by stretching. This complex state of stress better reflects actual use conditions for panel composites.

A patterned composite sprayed with SiC and Al6061 particles was fabricated using an 800 μm pattern size mask on a 19 mm coupon diameter. The composite consists of 14 layers of AZ31 coupons. The spraying and consolidation conditions are the same as described earlier. Figure 4.15 shows the load-displacement curves from the SPT for the patterned and the uniform sprayed samples that have a similar amount of sprayed particles. The unreinforced AZ31 sample was included for comparison. The patterned sample had the highest ultimate load of 1300 N, and the uniform sprayed one had 1150 N.

As discussed earlier, these patterns may have activated a mechanical interlocking mechanism between the reinforcement zone and the matrix phase (AZ31 sheet), which may have helped enhance the mechanical behavior. Moreover, these reinforcement zones are separated and surrounded by a soft phase (matrix), which may have enhanced the deformation behavior of these composites [60]. In addition, these patterns acted as crack arresting zones that add resistance to the crack propagation, which delayed the failure.

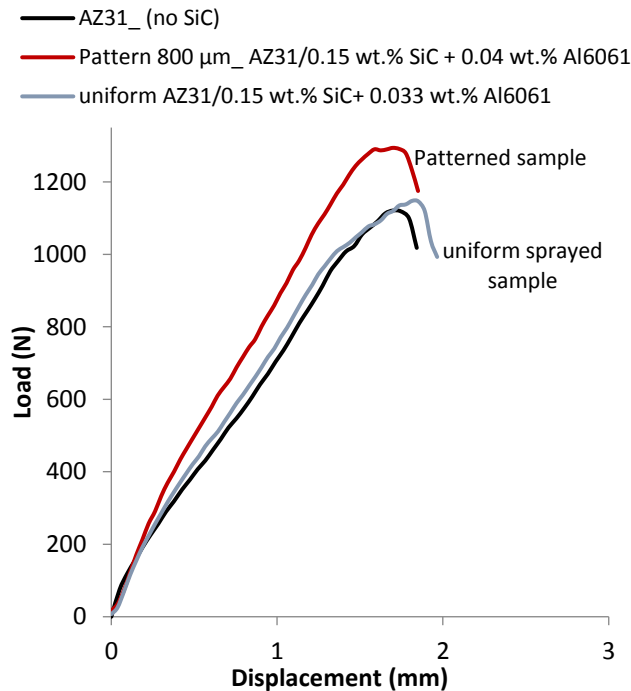


Figure 4.15 SPT load – displacement curves.

4.4 Conclusions

In this study, AZ31/ (SiC-Al6061) composite panel was synthesized by spraying ethanol suspension of SiC-Al6061 particle mixture on the AZ31 foils. A custom structure was successfully created by spraying the nanoparticles through a patterned mask. The patterned

composite showed an enhancement in the flexural yield and ultimate strength of 75% and 18% compared with the unreinforced sample, respectively. The patterned composite showed higher ultimate load and comparable total displacement compared with unreinforced and uniformly sprayed sample (same reinforcement amount). The enhancement in the mechanical properties was mainly attributed to the brick-and-mortar configuration that allowed a tension-shear load transfer chain between the reinforcement and the matrix phase. On the nanoscale level, the nanostructure of the reinforcement phase helped enhance the damage resistance of the reinforcement phase. The liquid phase introduced during the semi-solid consolidation, combined with the nanostructure of the reinforcement phase created an interpenetrating gradient interface that may have helped to control the interface debonding and the crack propagation. Overall, the proposed approach was successful in fabricating a complex, multiscale structure in metal composites, which showed a considerable enhancement in mechanical properties.

CHAPTER 5 MAGNETIC FIELD ASSISTED DEPOSITION OF FERROMAGNETIC NANOPARTICLES

5.1 Introduction and motivation

The progress in understanding and utilization of the dominant forces and phenomena at the nanoscale has advanced the bottom-up nanofabrication, especially in the area of directed/self-assembly methods [146]. It allows scalable fabrication of multifunctional nanostructured materials with exceptional properties [146], unlike the top-bottom nanolithography based techniques, which are characterized with relatively high cost, small fabrication scale, and high time consumption [125, 147]. Various methods have been implemented in nanoparticle self-assembly, which include those utilizing evaporation dynamics [125, 140, 141, 148, 149], electrophoretic forces [150], elasto-cappillary dynamics [147, 151], gravitational forces [152], centrifugal forces [153], electrostatic interaction [154, 155], van der Waals interaction [156], and magnetic field [157].

Magnetic field assisted assembly in particular has attracted the interest of many researchers due to its relatively fast stimuli-response behavior [40, 158]. It has showed promising capabilities for use in many applications such as actuators [159, 160], optoelectronic devices [148], optical diffraction gratings [161] and photonic crystal [162], biomedical applications [163, 164], composites [165-167], solar cells [168], electronics, and sensors [169]. Magnetic field assisted assembly can be categorized into two main techniques: (i) colloidal assembly of particles in a suspension where the magnetic dipole-dipole interaction of the particle are the dominant assembly force; and (ii) surface-patterning where a predetermined magnetic field gradient pattern is used to selectively attract the magnetic particles towards the designated deposition spots on a substrate [40].

Magnetic field can assemble colloidal building blocks into complex secondary structures [41]. Under a relatively low magnetic field, magnetic nanoparticles tend to assemble in a 1D chain-like structure directed by the particles dipole-dipole interaction [166, 170-175]. By increasing the magnetic field, these chains tend to bundle up in a 2D sheet or 3D crystal structures [41, 152, 162, 176, 177]. Assembly of particles in various shapes of 1D periodic chains [166, 173, 176, 178, 179], 2D sheets [41, 158], and 3D structures [9, 152, 162, 177] have been reported depending on the particle size and spatial concentration, inter-particle interactions (equilibrium between attractive and repulsive forces), and magnetic field characteristics [180]. Upon removal of the magnetic field, the assembly does not retain its shape unless a complementary step to bond the assembled particle is performed. Cross linking (e.g. using DNA [181] or chemically [40]) or coating of assemblies (e.g. silica coating [176, 179]) have been used to retain the assembled shape after removing the magnetic field. However, the current approaches are limited to generating colloidal assemblies with shape configurations mentioned earlier. Complex, custom designed shapes cannot be assembled using this approach.

Magnetically directed surface-patterning has been a promising approach for direct assembly of nanoparticles in custom user-defined shapes. Magnetic nanoparticle in a spatially variable magnetic field will be driven and pulled towards the highest field gradient regions; this phenomena is called magnetophoresis [42, 182]. Magnetic manipulation of nanoparticles can be a promising approach to selectively deposit nanoparticles if the applied magnetic field is precisely modulated. Different methods have been reported to modulate the magnetic field by creating a custom designed pattern of variable magnetic field gradient on a magnetic source to assemble magnetic nanoparticles. Ye et. al. have demonstrated that perpendicular recording media can direct self-assembly of magnetic nanoparticles from a colloidal fluid into custom

designed patterns deposited at the medium surfaces [42]. Velez et. al. have used magnetization mask to selectively magnetize a desired pattern onto a deposited magnetic material film. They were able to deposit nanoparticle with a complex shapes using this approach and to in-situ cross-linking the deposited nanoparticle into permeant assemblies [40]. Zhang et. al., introduced a lithographically patterned nonmagnetic substrate to modulate the local magnetic field distribution [41]. Some of these methods, however, involve multiple steps and sophisticated instruments to create magnetically patterned source. One way of patterning the magnetic field can be by creating topographical variation on the magnetic source, creating protrusions and valleys on the surface. This topographical variation creates magnetic field gradients on the substrate surface with local high magnetic field at the protrusions and lower field at the valleys. In this work, we investigated magnetic field patterning by machining (CNC or laser machining) user defined patterns directly on the magnetic source. The magnetic source can be permeant, electromagnet, or magnetic material attached to a magnet. This method is characterized by its simplicity, scalability, and low cost.

Conventionally, magnetically directed surface-patterning has been limited to magnetic particles [40]. In this work, we demonstrate the use of magnetically directed surface-patterning approach to deposit a mixture of magnetic and nonmagnetic nanoparticles into user-defined pattern on a substrate. The magnetic particles (Fe nanoparticles) were used as the carrier for the nonmagnetic particles (SiC) through van der Waals particle interaction. The deposition behavior and resolution were studied.

5.2 Experimental setup

Figure 5.1 illustrates the magnetic field-assisted deposition setup. Deposition behaviors of magnetic-only (Fe) and magnetic (Fe) + nonmagnetic (SiC) particles were performed. A pure iron disc attached to a NdFeB magnet was used as the magnetic source. The magnetic source was fabricated by machining grooves on the surface creating patterns of protrusions. These protrusions modulate the local magnetic field distribution on the deposition substrate surface. The regions on the substrate surface corresponding to the protrusions have relatively higher magnetic field strength compared to the other regions corresponding to the grooves. [162, 183]. As a result, the peak magnetic field gradient regions are located at the periphery of the protrusions [40-42, 183]. For the deposition process, 0.2 ml of suspension is introduced on a 50 μm aluminum substrate, which is fixed on top of the patterned iron disc. The suspension is left to dry under the ambient conditions (300°K) while applying the magnetic field. Two different machining process have been used to pattern the iron disks, micro-milling and micro-laser machining.

A pure iron disk has been machined using micro-milling CNC machine and polished as shown in Figure 5.1. Total of six lines have been machined with three pairs of linewidth 65, 100, and 200 μm as shown in Figure 5.2. All the protrusion lines have a depth of 150 μm and a spacing of 750 μm .

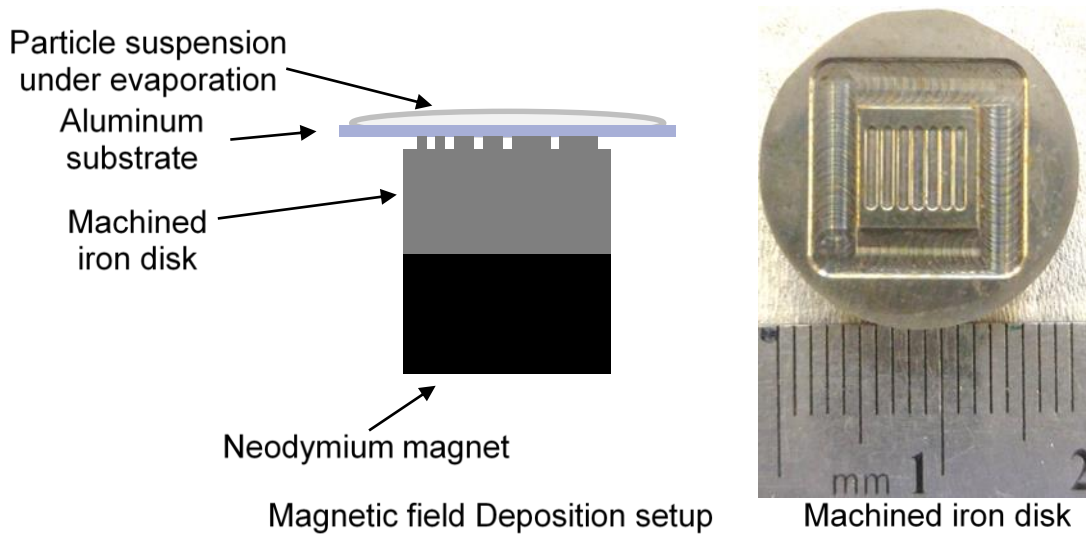


Figure 5.1 Machined iron disk attached to a magnetic source

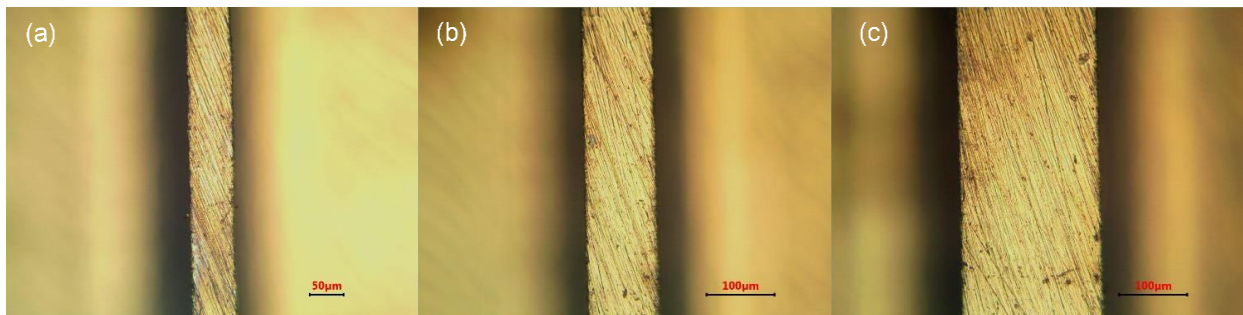


Figure 5.2 Micro-line protrusion on the iron disc: (a) 65 μm , (b) 100 μm , and (c) 200 μm

For the second iron disc, it has been laser machined, using a 6 μm laser beam creating smaller protrusions with smaller spacing compared to micro-milling machining. This disc was machined by Prof. Yung C. Shin group at the advanced laser micro-machining facility at Purdue University. Protrusions with different sizes have been machined on the disk with a single line of 50 μm and four pairs of line widths 10, 25, 75, and 100 μm as shown in Figure 5.3. The spacing between each protrusion pair was the same as the width of these protrusions. However, the 10 μm protrusions were too narrow and evaporated during laser machining process.

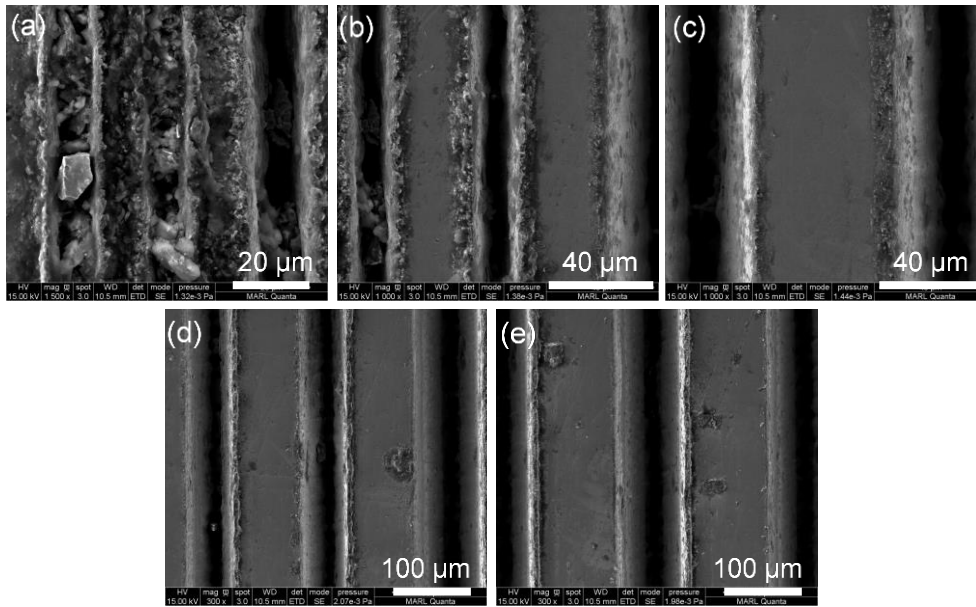


Figure 5.3 laser machined line protrusions on iron disc with linewidth of, (a) 10 μm , (b) 25 μm , (c) 50 μm , (d) 75 μm , and (e) 100 μm

Various types of suspensions were prepared and used for deposition as summarized in Table 5.1. One deposition consisted of only magnetic iron (Fe) nanoparticles, while the others had a mixture of Fe nanoparticles and nonmagnetic silicon carbide (SiC) particles with different SiC particle sizes and Fe : SiC weight ratios (R). All nanoparticles in this study have been handled in a glove box while the operator is equipped with personal protective equipment as recommended by the university safety guidelines (Appendix A), which include wearing a lab coat and putting on gloves, a dust mask, and safety glasses. As received Fe nanoparticles, in particular, have been opened and handled with extra care in the glove box as it has a high affinity to oxidation that can lead to exothermic reaction and cause particle ignition. The different suspension characteristics and particle sizes are summarized in Table 5.1. The suspensions were prepared by mixing the particles in ethanol. For the Fe and SiC mixture suspensions, the sonication was performed in two steps. In the first step, each particle specie was suspended and

dispersed separately in an ultrasonic bath for 4-6 hours. Then, they were mixed and sonicated for another one hour prior to deposition. For the Fe suspensions, only the first step was performed prior to deposition.

Table 5.1 Summary of nanoparticle size, suspension concentration, and mixing parameters

Deposited particles	Suspension concentration (wt.%)	Fe : SiC wt. ratio (R)	Suspension vol. ratio (SiC/ethanol : Fe/ethanol)
Fe (25 nm)	0.025 % Fe/ethanol	N/A	N/A
Fe (25 nm) + SiC (80 nm)	0.025 % Fe/ethanol 0.1% SiC/ethanol	1:1	1:4
Fe (25 nm) + SiC (80 nm)	0.025 % Fe/ethanol 0.1% SiC/ethanol	1:5	1:20
Fe (25 nm) + SiC (80 nm)	0.025 % Fe/ethanol 0.1% SiC/ethanol	1:10	1:40
Fe (25 nm) + SiC (80 nm)	0.025 % Fe/ethanol 0.1% SiC/ethanol	1:20	1:80
Fe (25 nm) + SiC (800 nm)	0.025 % Fe/ethanol 0.1% SiC/ethanol	1:1	1:4
Fe (25 nm) + SiC (5 μ m)	0.025 % Fe/ethanol 0.1% SiC/ethanol	1:1	1:4

5.3 Results and discussions

The deposition of only magnetic particles (Fe) was investigated to understand their assembly behavior. Figure 5.4 shows the deposition of Fe magnetic nanoparticles with different deposition pattern sizes. No particles were deposited outside the designated deposition regions. Higher deposition concentrations were found in the middle forming island-like deposition microstructures along the deposition line. Figure 5.6 shows the major and total deposition widths corresponding to the protrusion sizes 65, 100, and 200 μ m. The major deposition width is the continuously deposited portion excluding the peripheral fringes, while the total deposition

width includes the peripheral fringes. EDS analysis was used to help determine the deposition line width. Figure 5.5 shows the EDS line scan of the deposition corresponding to 65 μm line protrusion. It shows major and total deposition widths of the deposited micro-patterns.

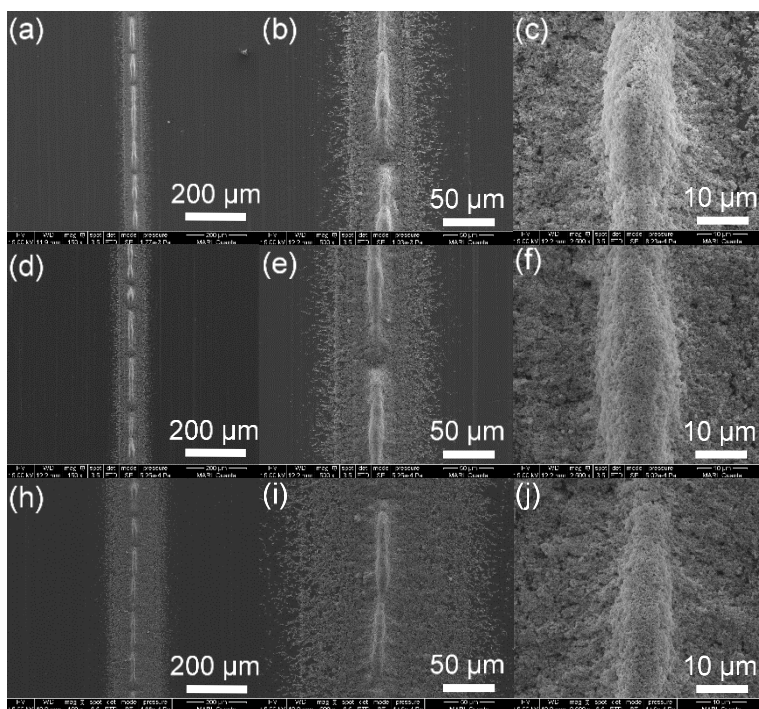


Figure 5.4 Fe nanoparticle deposition corresponding to different line protrusion sizes, (a, b, and c) 65 μm , (d, e, and f) 100 μm , and (h, i, and j) 200 μm

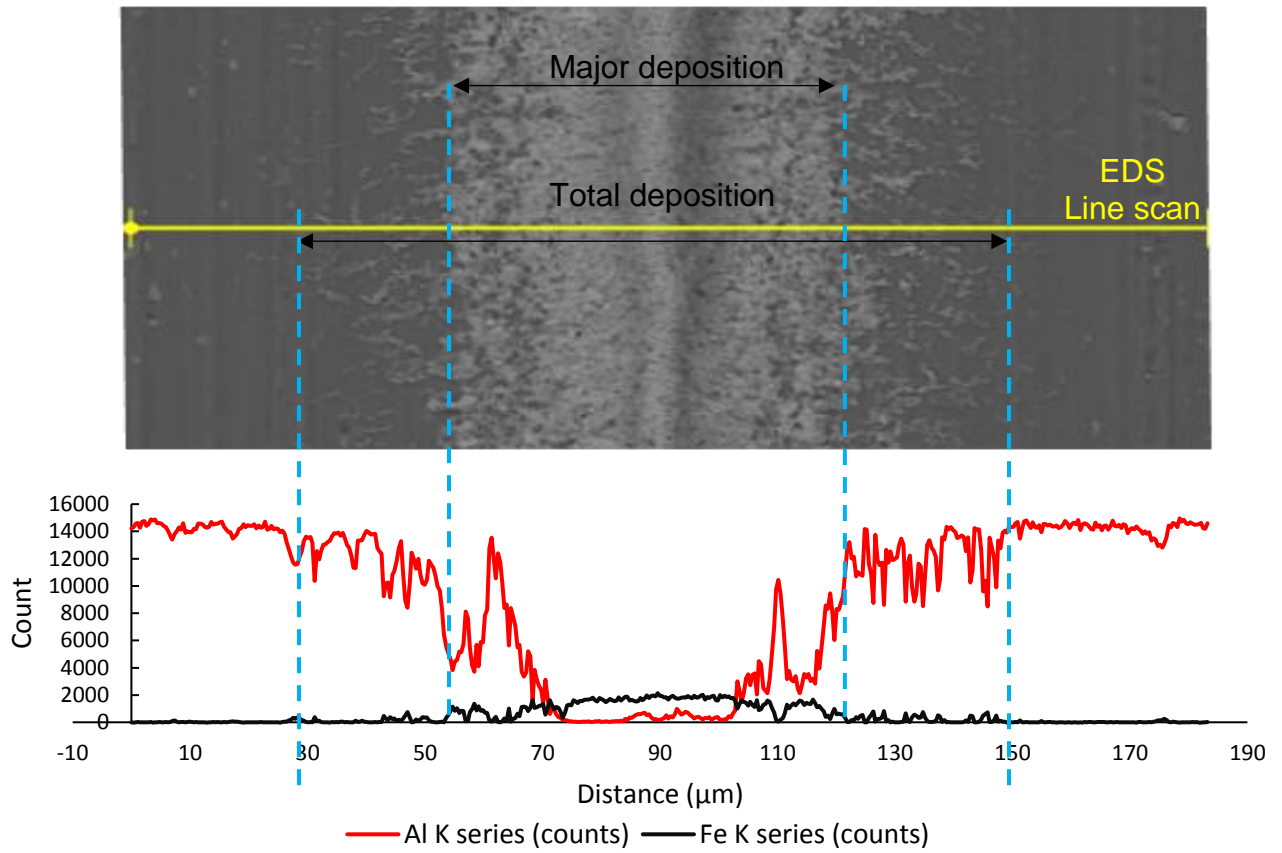


Figure 5.5 EDS line scan of the deposited Fe particles corresponding to 65 μm protrusion

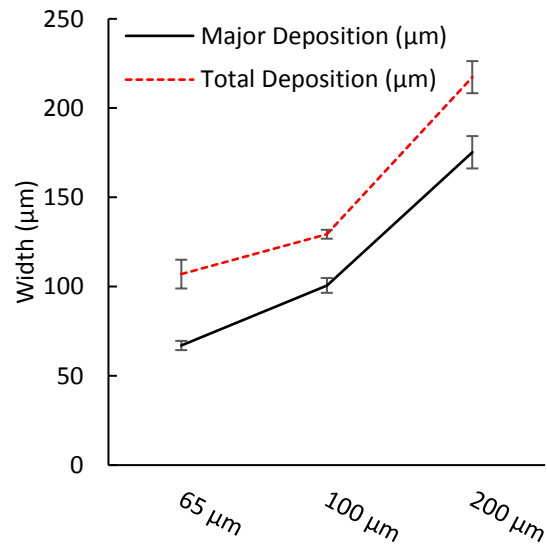


Figure 5.6 Major and total deposition widths of the Fe nanoparticle depositions

In the absence of the magnetic field, the nanoparticles are well dispersed in the suspension and the Brownian motion makes them randomly mobile. Two forces are induced upon applying the magnetic field: (i) magnetic packing force that pulls each individual magnetic particle to the deposition surface and (ii) the dipole-dipole interaction force which is attraction forces in between the magnetic particles. The magnetic packing force attracts each individual particle toward the highest local field gradient on the deposition surface. The magnetic packing force is described by $F_m = \nabla(\mu B)$ [41], where μ is the induced magnetic moment and B is the strength of the external field. The dipole-dipole interaction between the particle controls the assembly and clustering behavior of the nanoparticles, which is described by $F_d = 3\mu^2(1 - \cos^2 \theta)/d^4$. θ is the angle between the unit vector representing the distance between the centers of the particles and the direction of the field, and d is the center-center distance [41]. As the particles reach the deposition surface, the deposited particles pull the arriving particles due to the dipole-dipole interaction and begin to arrange them on top of each other. They form piles at the periphery of the magnetic pattern [40]. These piles grow as more particles arrive at the deposition surface. When the distance between those piles is close enough, they begin to interact magnetically and coalesce together forming bigger piles (Figure 5.4).

During evaporation, a secondary assembly mechanisms is introduced, which influences the final nanoparticle assembly. The surface tension and the capillary forces attract the deposited particles to minimize the surface area of the assembly [141, 147, 151, 156].

The mixture of magnetic and nonmagnetic nanoparticles was used to understand the particle interaction, transport, and deposition. A mixture of Fe (25 nm) + SiC (80 nm) with 1:1 weight ratio (R) was used to deposit line patterns with different widths of 65 μm , 100 μm , and 200 μm . The resulting deposition structures are shown in Figure 5.7. Both the nonmagnetic and

magnetic particles formed a well-defined pattern structures. The regions between the individual pattern features were nearly particle free as shown in Figure 5.7. The island-like structures shown in the Fe nanoparticle deposition are still visible with the Fe + SiC mixtures, but are less distinct and begin to fade as the deposition line width increases.

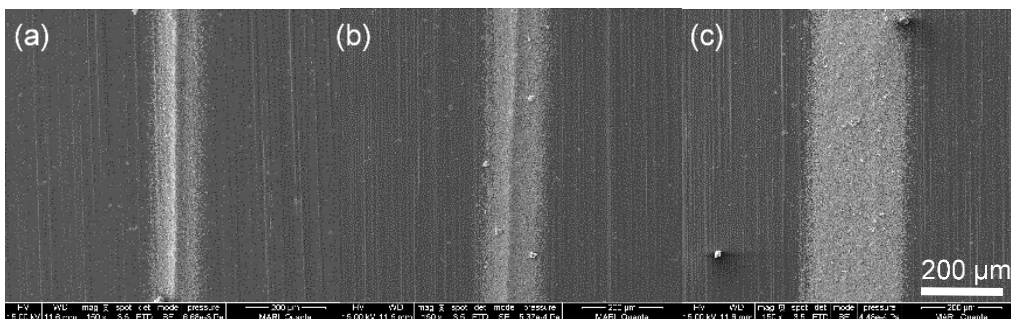


Figure 5.7 Fe+SiC nanoparticle deposition (weight ratio of 1:1) corresponding to protrusion sizes (a) 65 μm , (b) 100 μm , and (c) 200 μm

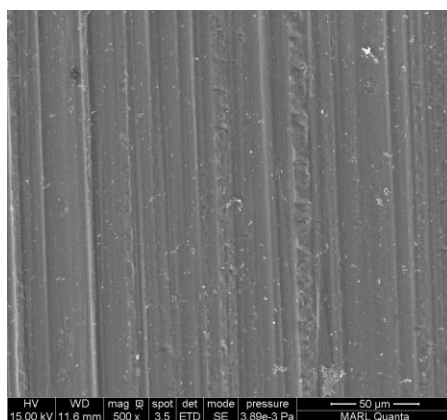


Figure 5.8 Areas between the deposition lines

EDS technique was used to help determine the deposition line widths combined with image analysis by performing line scans along the width of different deposition structures.

Figure 5.9 shows the major and total deposition widths for the Fe + SiC mixture with 1:1 weight ratio.

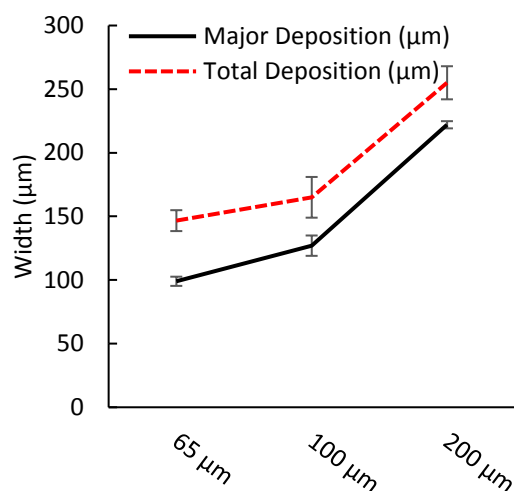


Figure 5.9 Major and total deposition widths of the Fe (25 nm) + SiC (80 nm) nanoparticle (weight ratio 1:1)

When a mixture of nonmagnetic and magnetic particles is introduced, the van der Waals interaction becomes the dominant force between the magnetic and nonmagnetic particles. The nonmagnetic particles get attached to the magnetic particles and both travel to the deposition spots [184, 185]. Moreover, the magnetic dipole-dipole interaction helps to form network of magnetic particle links [166]. The interstitial spaces within this networks helps to retain the nonmagnetic particles adding extra support during transfer. Figure 5.10 shows the EDS map of Si and Fe, and both elements are uniformly deposited. This indicates that there is acceptable homogenous mixing between the two particle species.

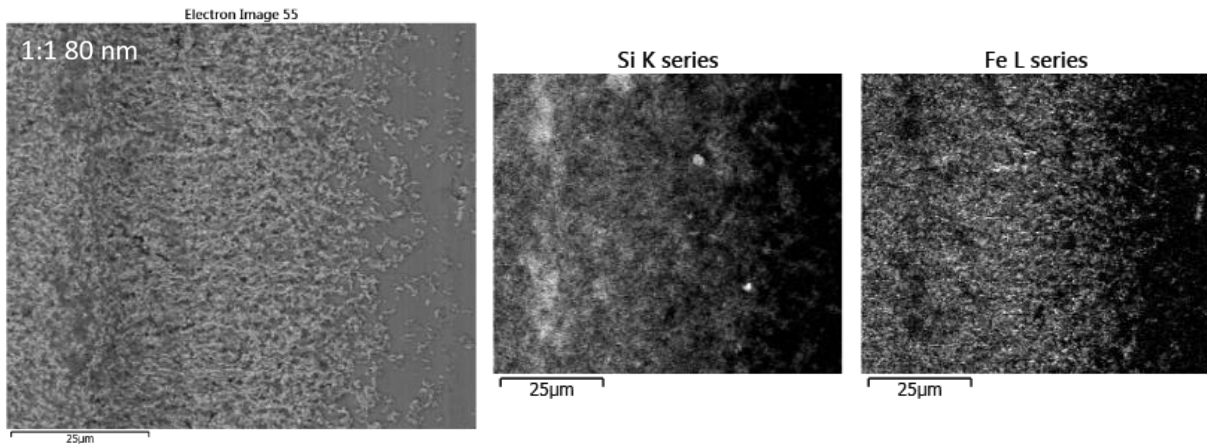


Figure 5.10 SEM image of the Fe + SiC deposition corresponding to the 65 μm protrusion and the EDS maps of the Si and Fe elements (R= 1:1)

To determine the transfer capability of Fe nanoparticles, depositions of suspensions with different R (1:1, 1:5, 1:10, and 1:20) were analyzed. Figure 5.11 shows SEM images of the Fe + SiC particle mixture deposition with different R deposited on the 65 μm width protrusion. Successful deposition was achieved up to R of 1:20. As the concentration of SiC particles increases in the suspension, the width of the deposited patterns increases resulting in a decrease in the resolution. It can be noticed that the island like structures fade gradually as R increases. This is because the magnetic particle dipole-dipole interaction decreases with increasing nonmagnetic particle concentration. As discussed earlier, the nonmagnetic particles are attracted to the magnetic particles forming a cluster that deposit on the substrate surface. As the concentration of the SiC increases, more SiC particles are packed between the Fe particles increasing the interaction distance between the Fe particles. As a result, the dipole-dipole interaction force decreases between the magnetic particles, and thus, the total magnetic-induced stiffness of the assembly decreases forming more relaxed pile structures.

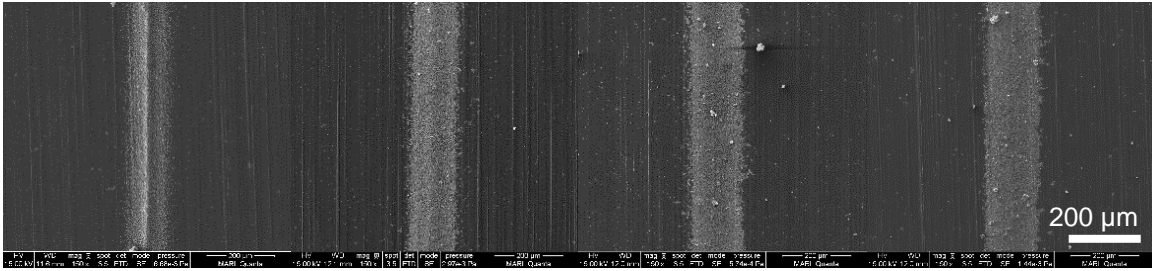


Figure 5.11 Fe + SiC nanoparticle deposition corresponding to protrusion size 65 μm with different Fe:SiC particle weight ratio, (a) 1:1, (b) 1:5, (c) 1:10, and (d) 1:20

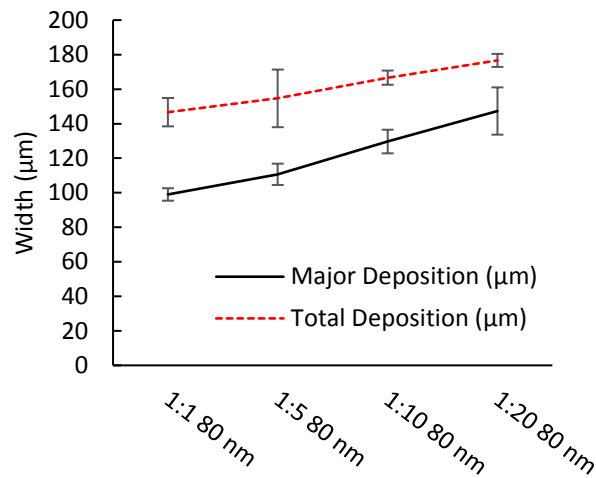


Figure 5.12 Major and total deposition widths of the Fe (25 nm) + SiC (80 nm) nanoparticle with different deposition weight ratios

The number of SiC (80 nm) particles carried by an individual Fe (25 nm) particle can be theoretically evaluated assuming that all SiC particles have been transferred for each R.

$$\text{the mass of Fe particles in the suspension} = x$$

$$= (N_{\text{Fe}}) (m_{\text{pFe}})$$

$$= (N_{\text{Fe}}) (V_{\text{pFe}}) (\rho_{\text{Fe}})$$

$$= (N_{\text{Fe}}) \left(\frac{4}{3} \pi r_{\text{Fe}}^3 \right) (\rho_{\text{Fe}})$$

$$\text{the mass of SiC particles in the suspension} = \frac{x}{R}$$

$$\begin{aligned}
&= (N_{SiC}) (m_{pSiC}) \\
&= (N_{SiC}) (V_{pSiC}) (\rho_{SiC}) \\
&= (N_{SiC}) \left(\frac{4}{3} \pi r_{SiC}^3 \right) (\rho_{SiC}) \\
\text{Then, } \frac{N_{SiC}}{N_{Fe}} &= \frac{1}{R} \left(\frac{\rho_{SiC}}{\rho_{Fe}} \right) \left(\frac{r_{SiC}}{r_{Fe}} \right)^3
\end{aligned}$$

N_{Fe} and N_{SiC} are the number of Fe and SiC particles in the deposition suspension, respectively; V_{pFe} and V_{pSiC} are the volume of the individual Fe and SiC particles, respectively; ρ_{Fe} and ρ_{SiC} are the density of Fe and SiC particles, respectively; and r_{Fe} and r_{SiC} are the radius of the Fe and SiC particles, respectively. Table 5.2 shows the number of SiC particles carried by one Fe Particle (N_{SiC}/N_{Fe}). It can be noticed that for $R= 1/20$, one Fe particle was capable of carrying almost 1.5 SiC particles, noting that the volume of the SiC particle is, on average, 30 times the volume of the Fe particles.

Table 5.2 The number of SiC particles transferred by a single Fe particle for different R

Fe : Si C wt. ratio (R)	N_{SiC}/N_{Fe}
1:1	0.075
1:5	0.374
1:10	0.747
1:20	1.495

Figure 5.13 shows little nanoparticle deposition outside the designated deposition areas. For R of 1:20, however, the deposited clusters are slightly larger. Figure 5.14 shows the mixing behavior between the two particle species, Fe and SiC. For all ratios, the particles showed an acceptable mixing behavior.

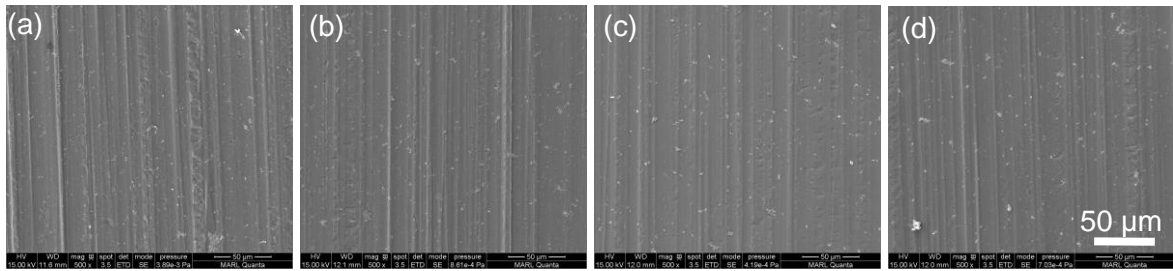


Figure 5.13 Areas in between the deposition lines for different R, (a) 1:1, (b) 1:5, (C) 1:10, and (d) 1:20

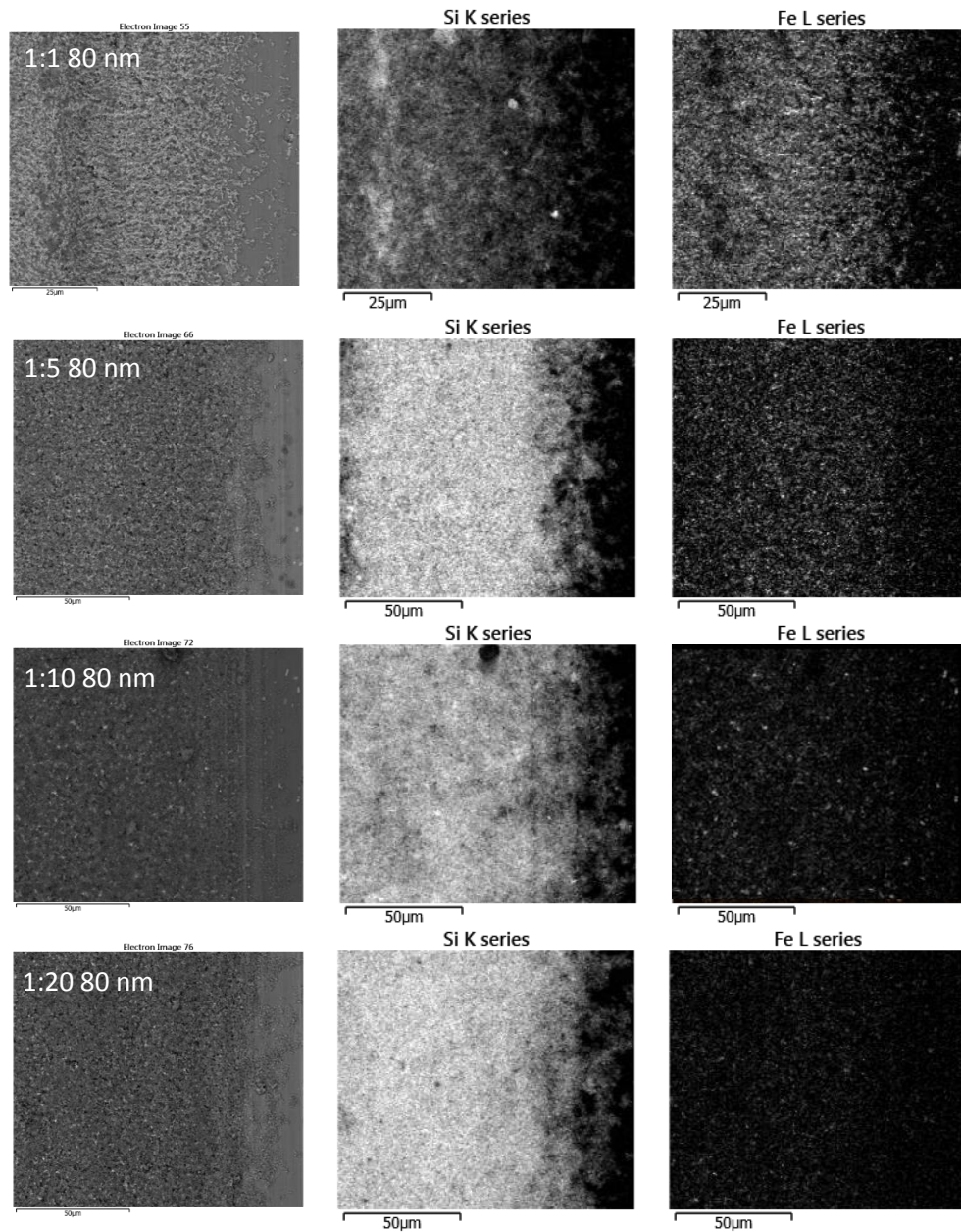


Figure 5.14 SEM image of the Fe + SiC deposition corresponding to the 65 μm protrusion and the EDS maps of the Si and Fe elements of different R, 1:1, 1:5, 1:10, and 1:20

A mixture of SiC and Fe nanoparticles was deposited using different SiC particle sizes of 80 nm, 800 nm, and 5 μm. There is approximately one order of magnitude difference between the three particle sizes to capture the changes in the deposition and assembly behavior. The

resulting deposition structure is shown in Figure 5.15, and successful deposition was observed for all the particle sizes. However, as the SiC particle size increases, more particle deposition is observed between the deposited patterns (Figure 5.16). There are three major forces acting on the SiC particles, van der Waals force between the SiC and Fe particles, the drag force acting against the moving particles in the suspension, and the gravitational force [182]. The effect of the gravitational force on the SiC particle increases as the particle size increases. The van der Waals force is competing with the drag force acting on the SiC particles. The van der Waals force between two Fe and SiC particles can be expressed as $F_{vw} = \frac{A}{6D^2} \left(\frac{r_{Fe} r_{SiC}}{r_{Fe} + r_{SiC}} \right)$, where A is the Hamaker constant, D is the separation distance between the particle surfaces, and r_1 and r_2 are the radii of the Fe and SiC particles, respectively. For a particle attached to a surface, D is about 0.4 to 1 nm [184, 185]. A and D are almost constant for different SiC particle size suspension systems. Accordingly, van der Waals force will depend on $\left(\frac{r_{Fe} r_{SiC}}{r_{Fe} + r_{SiC}} \right)$ as calculated in Figure 5.17. Therefore, the van der Waals force does not continually increase even the SiC particle size increases. On the other hand, the drag force increases significantly, which may cause the detachment of the SiC particles from the Fe particles [182]. Figure 5.18(a) shows SEM image of SiC particle deposited outside the deposition area where no Fe nanoparticles are present on the SiC particle surface. On the other hand, Figure 5.18(b) shows SiC particles at the periphery of the deposited patterns where they are anchored to the Al substrate by means of the Fe nanoparticle chains.

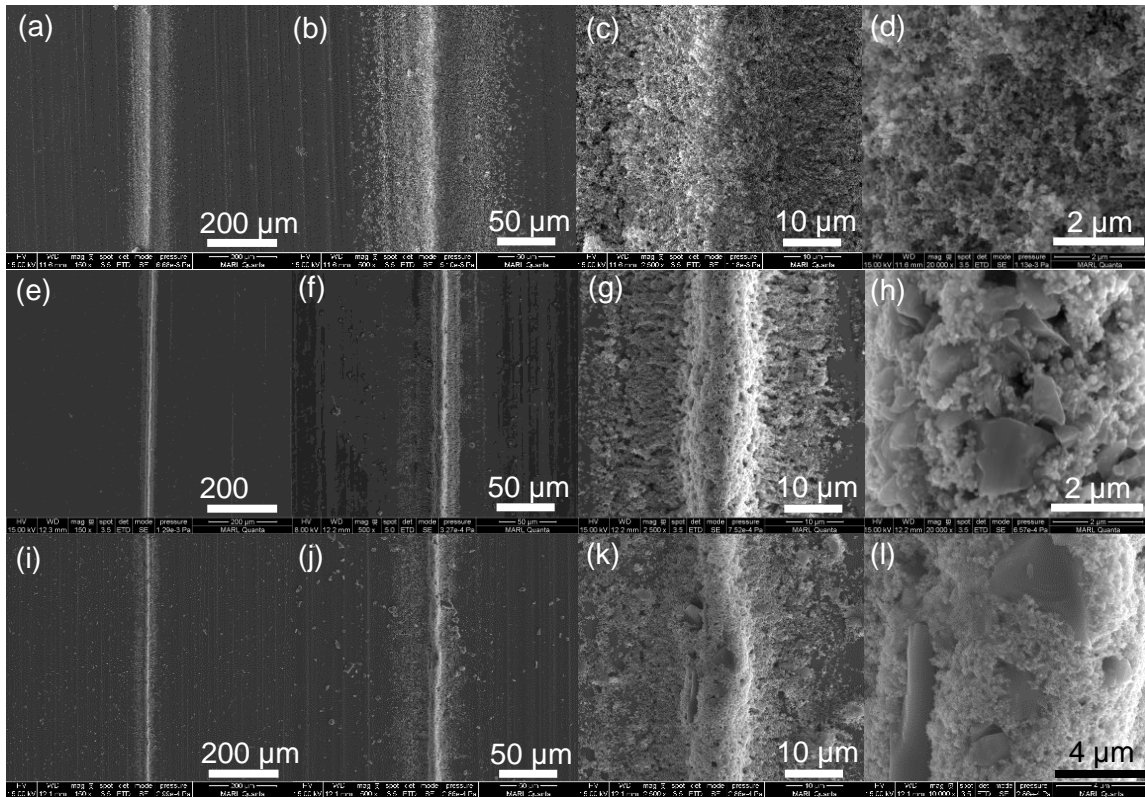


Figure 5.15 Fe + SiC nanoparticle deposition (1:1 weight ratio) corresponding to protrusion size 65 μm with different SiC particle sizes, (a, b, c, and d) 80 nm, (e, f, g, and h) 800 nm, and (i, j, k, and l) 5 μm

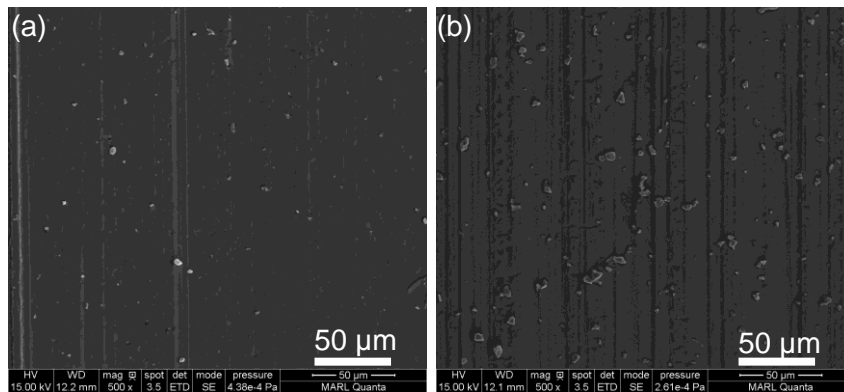


Figure 5.16 areas in between the deposition lines of Fe + SiC (1:1) deposition with different SiC particle sizes, (a) 800 nm and (b) 5 μm

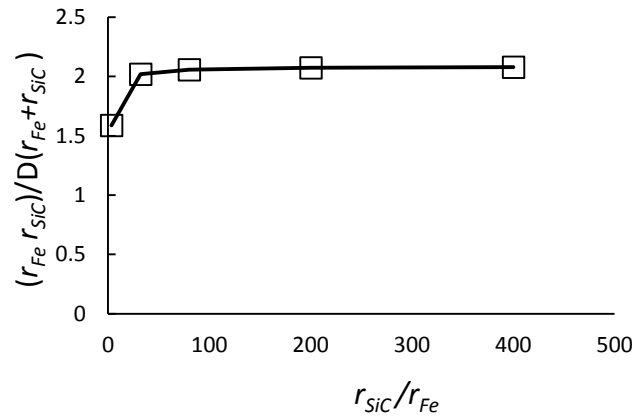


Figure 5.17 The effect of SiC particle size on the van der Waals force

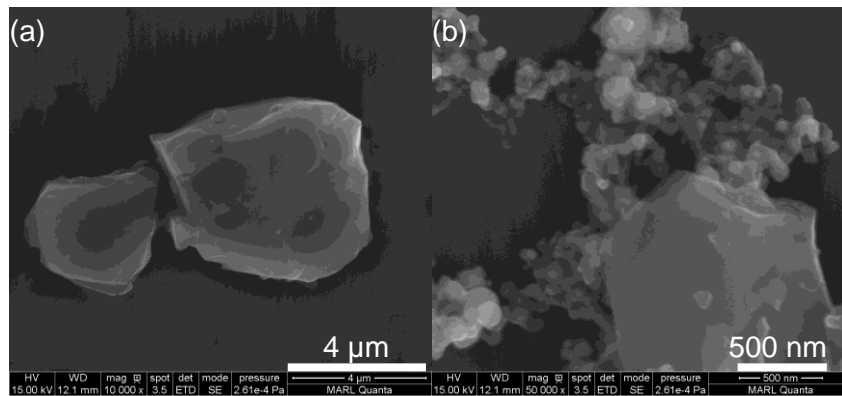


Figure 5.18 SEM image of SiC (5 μ m) particle , (a) deposited in between the deposition lines and (b) SiC particle deposited at the periphery of the deposition area

Figure 5.19 shows the deposited pattern widths corresponding to the 65 μ m protrusion for deposition of Fe + SiC with different SiC particle sizes. As the SiC particle size increases, the major and total deposition widths decrease.

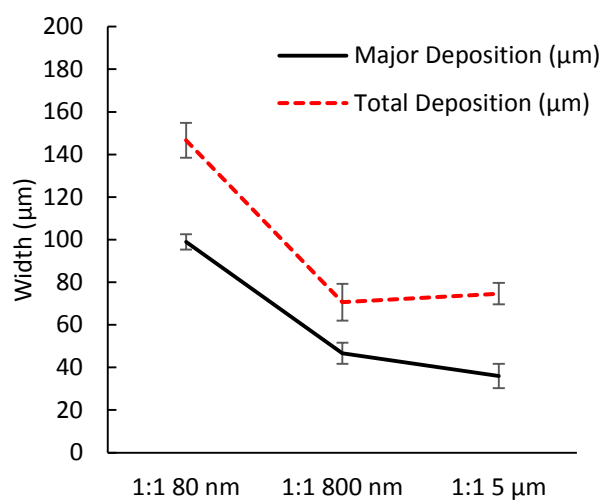


Figure 5.19 Major and total deposition widths of the Fe (25 nm) + SiC (80 nm) nanoparticle with different deposition weight ratios

Figure 5.20 shows the mixing behavior between the two particle species, Fe and SiC. For all particle sizes, the Fe + SiC particles showed acceptable mixing behavior. It can be noticed that there is no segregation for neither the SiC nor the Fe particles. For the 5 μm SiC particles, it is clearly seen that every particle is individually surrounded and embedded by Fe particle network.

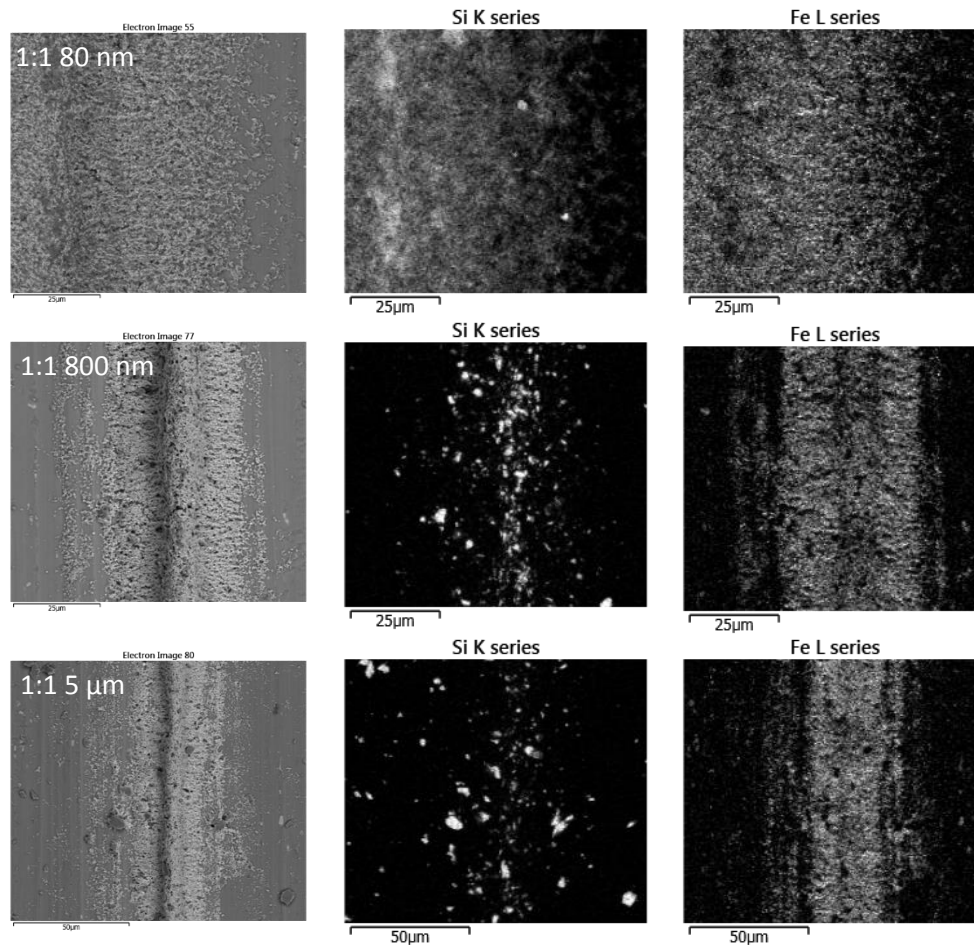


Figure 5.20 SEM image of the Fe + SiC deposition corresponding to the 65 μm protrusion and the EDS maps of the Si and Fe elements of different SiC particle sizes, 80 nm, 800 nm, and 5 μm

The effect of the spacing between protrusions on the deposition structure was evaluated. A mixture of Fe (25 nm) + SiC (80 nm) with 1:1 weight ratio was used to deposit line patterns. The ratio between the protrusion width and the spacing between the protrusions is almost 1:1. The resulting deposition structures are shown in Figure 5.21. Both the nonmagnetic and magnetic particles formed a well-defined pattern structures with well-defined spacing between the two deposited lines, which shows the high deposition resolution in terms of the spacing

between the deposited features. Also, it indicates that possible deposition of a high density array of patterns (ratio between feature size and spacing between features is 1:1) can be achieved with almost no interaction between the deposited patterns. It was noticed that the deposition width is smaller than the width of the corresponding protrusion. The deposition widths of the 75 and 100 μm protrusions were around 60 and 78 μm , respectively. The 10 and 25 μm protrusions did not have any corresponding deposition on the substrate. The laser machined edges experience residual stresses due to the thermal shock wave resulted from the rapid heating and cooling rate far from metallurgical equilibrium [186]. That results in permanent deterioration of the magnetic permeability of the heat affected zone at the cut edge, which is estimated by 10-15 μm [186, 187]. The deposition corresponding to the laser machined protrusion always observed thinner width compared with the corresponding protrusion by 15-25 μm for this reason.

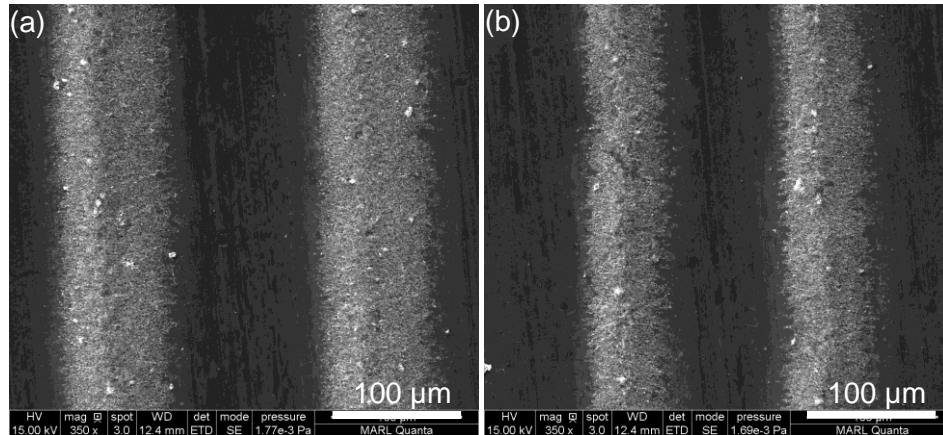


Figure 5.21 Fe + SiC nanoparticle deposition (weight ratio of 1:1) corresponding to protrusion sizes and spacings of (a) 100 μm and (b) 75 μm

A mixture of Fe (25 nm) + SiC (80 nm) with 1:1 weight ratio was used to deposit a line pattern corresponding to 50 μm protrusion. Figure 5.22 shows the SEM images of the deposited structure. A well-defined line of 15-25 μm was observed, which indicates the relatively high

deposition resolution with this technique. As discussed earlier, laser machining results in deterioration of the magnetic permeability of the heat affected zones at the machined edges, which is estimated by 10-15 μm . As a result, smaller deposition width is observed compared with the corresponding protrusion width.

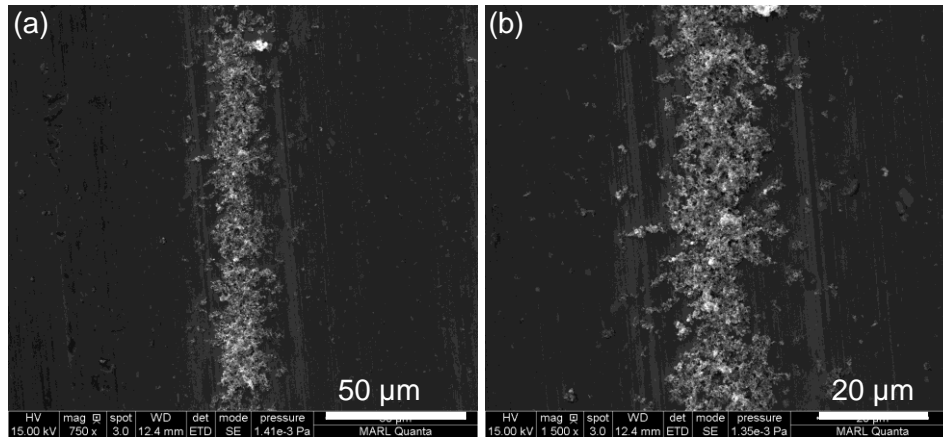


Figure 5.22 Fe + SiC nanoparticle deposition (weight ratio of 1:1) corresponding to 50 μm protrusion size (a) corresponding deposition line and (b) higher magnification

5.4 Conclusions

A magnetic field directed pattern-deposition of a mixture of magnetic (Fe) and nonmagnetic (SiC) particles have been investigated. The magnetic field pattern was modulated by creating topographical pattern (protrusions) on the magnetic source surface. Creating topographical variation on the magnetic source surface is a promising approach to precisely modulate the magnetic field distribution that can be used for, relatively, high precision particle deposition. Deposition structure as small as 15 μm (R of 1:1) was achieved. For magnetic particle deposition, two major forces are driving the transfer, assembly, and deposition behavior. These forces are the magnetic packing forces and dipole-dipole interaction forces. The magnetic packing force is responsible for the particle transport and anchoring to the deposition surface. Fe

particles were precisely deposited in the designated deposition regions, with no deposition outside the designated deposition regions. The deposited patterns were preserved during evaporation due to the strong anchoring to the substrate. The dipole-dipole interaction is responsible for the particle arrangement and assembly, which control the assembly morphology. Deposition of only Fe particles showed a strong dipole-dipole interaction that resulted in island-like structure with high aspect ratio. Adding nonmagnetic particles to the mixture reduces the magnetic particle interaction which showed less sharp island-like structure. For deposition of a mixture of magnetic and nonmagnetic particles, van der Waals forces govern the magnetic and nonmagnetic particle interaction. Deposition of a mixture of Fe + SiC particles up to 1:20 weight ratio was achieved. Further increase in nonmagnetic particle concentration, however, reduces the deposition resolution due to weakening of the dipole-dipole interaction between the magnetic particles. The increase in the nonmagnetic particle size results in higher dragging forces causing detachment of the nonmagnetic particles from the travelling cluster. As a result, the transfer efficiency of the nonmagnetic particles diminishes causing the detached nonmagnetic particles to deposit outside the designated deposition spots.

CHAPTER 6 SUMMARY AND CONTRIBUTIONS

In this section, the conclusions and contributions of the work carried out were summarized. The major conclusions from each individual work were introduced in section 6.1, the contributions were discussed in section 6.2, the recommendation for future work was presented in section 6.3, and the acknowledgement in section 6.4.

6.1 Summary

The conclusions of individual sections are summarized as follows:

6.1.1 Effect of ball milling on graphene reinforced Al6061 composite fabricated by semi-solid sintering

In this work, Al6061-1.0 wt.% graphene composites were fabricated by ball milling Al6061 particles and graphene, followed by pre-compaction at room temperature, and finally by hot compaction in the semi-solid regime. The ball milling time varied from 10 minutes to 90 minutes.

- The 10- and 30-minute ball milling times were not enough to homogeneously disperse the graphene into the Al6061 matrix, which resulted in degradation of the flexural strength for the 10-minute milling time sample and no enhancement for the 30-minute milling time sample.
- The strength increase for the Al6061-1.0 wt.% graphene composite was 47% and 34% for the 60-minute and 90-minute times, compared with the reference Al6061 sample. The strengthening was significantly affected by the dispersion of the graphene in the matrix phase.

- According to the Raman analysis, further milling did not introduce more damage to the graphene, but instead helped to uniformly disperse the graphene and reduce the number of the stacked layers.

6.1.2 The ultrasonic spray deposition of sic nanoparticles for laminate metal composite fabrication

In this work, the dispersion and control of the deposited SiC nanoparticles were investigated using the ultrasonic spraying process. The ultrasonic spray deposition is governed by the suspension properties and the spraying parameters. The conclusions from this work can be summarized as the following:

- The atomization droplet size was largely influenced by the nozzle vibration frequency while the suspension parameters only had a limited impact. The change in suspension concentration up to 16 wt.% SiC only resulted in droplet size variation of approximately 1 μm .
- The deposited cluster size and morphology were affected by two main factors: the driving force that transports the atomized droplet from the nozzle to the substrate, and the evaporation behavior of the droplet (the amount of liquid phase present on the substrate and its evaporation rate). The amount of the liquid phase on the substrate and its evaporation rate were determined by the flow rate and the deposition surface temperature. The driving force is mainly determined by the air pressure and the nozzle to substrate distance.
- Large amount of liquid phase present on the substrate and low evaporation rate increased the particle cluster size and resulted in nonuniform deposition microstructure. Although a minimum inertia for the droplet is required for deposition of nanoparticles, violent air streams may destruct the deposited structure.

- The use of ultrasonic spraying of nanoparticles showed a promising potential to fabricate laminate composites. AZ31-SiC composites with uniformly deposited microstructure at the interface showed an improvement in the flexural yield strength by 49%, while composites with nonuniform structure or thicker deposition layer exhibited deterioration in mechanical properties.

6.1.3 Fabrication of pattern reinforced AZ31 multilayer composite using ultrasonic spray deposition

In this work, AZ31/ (SiC-Al6061) composite panel was synthesized by spraying ethanol suspension of SiC-Al6061 particle mixture on the AZ31 foils.

- The patterned composite showed an enhancement in the flexural yield and ultimate strength of 75% and 18% compared with the unreinforced sample, respectively. The patterned composite showed higher ultimate load and comparable total displacement compared with both unreinforced and uniformly sprayed sample (same reinforcement amount).
- The enhancement in the mechanical properties was mainly attributed to the brick-and-mortar configuration that allowed a tension-shear load transfer chain between the reinforcement and the matrix phase. On the nanoscale level, the nanostructure of the reinforcement phase helped enhance the damage resistance of the reinforcement phase.
- The liquid phase introduced during the semi-solid consolidation, combined with the nanostructure of the reinforcement phase created an interpenetrating, gradient interface that may have helped to control the interface debonding and the crack propagation.
- The proposed approach was successful in fabricating a complex, multiscale structure in metal composites, which showed a considerable enhancement in mechanical properties.

6.1.4 Magnetic field assisted nanoparticle deposition

A magnetic field directed pattern-deposition of a mixture of magnetic (Fe) and nonmagnetic (SiC) particles have been investigated. The magnetic field pattern was modulated by creating topographical pattern on the magnetic source surface. The conclusions from this work can be summarized as the following.

- Creating topographical variation on the magnetic source surface is a promising approach to precisely modulate the magnetic field distribution that can be used for, relatively, high precision particle deposition. Deposition structure as small as 15 μm (R of 1:1) was achieved.
- For magnetic particle deposition, two major forces, magnetic packing force and dipole-dipole interaction force, are driving the transfer, assembly, and deposition behavior. The magnetic packing force is responsible for the particle transport and anchoring to the deposition surface. Fe particles were precisely deposited in the designated deposition regions with no deposition outside the designated regions. Magnetic packing force was able to preserve the deposition structure from destruction during evaporation.
- The dipole-dipole interaction is responsible for the particle arrangement and assembly, which control the assembly morphology. Deposition of only Fe particles showed a strong dipole-dipole interaction that resulted in island-like structure with high aspect ratio. Adding nonmagnetic particles to the mixture reduces the magnetic particle interaction which showed less sharp island-like structure.
- For deposition of a mixture of magnetic and nonmagnetic particles, van der Waals forces govern the magnetic and nonmagnetic particle interaction. Deposition of a mixture of Fe + SiC particles up to 1:20 weight ratio was achieved. Further increase in nonmagnetic particle

concentration, however, reduces the deposition resolution due to weakening of the dipole-dipole interaction between the magnetic particles.

- The increase in the nonmagnetic particle size results in higher dragging forces causing detachment of the nonmagnetic particles from the travelling cluster. As a result, the transfer efficiency of the nonmagnetic particles diminishes causing the detached nonmagnetic particles to deposit outside the designated deposition spots.

6.2 Scientific Contributions

The major scientific contributions of the dissertation may be summarized as the following:

- One of the first attempts to implement ball milling technique to mix and disperse graphene in Al matrix was demonstrated. This study provided better understanding of effect of milling time on the dispersion efficiency and damage evolution of the graphene.
- For the first time, Al6061-graphene composites with improved strength (~ 47%) were successfully fabricated using mechanical alloying technique and semisolid consolidation. This work contributed toward understanding the relation between mechanical properties of the composites and the milling time.
- This work provided insight on identifying the governing parameters of the ultrasonic spray deposition process of nanoparticles and their appropriate control ranges. The effect of these parameters, which includes suspension and spraying parameters, on the deposition morphology was better understood.
- The potential of using ultrasonic spraying to fabricate laminate composites reinforced at the interface with nanoparticles was determined. This study identified the role of particle loading and deposition structure morphology on the composite behavior.

- A novel process was developed using magnetic field directed assembly of nanoparticles to manipulate and deposit a mixture of magnetic and nonmagnetic particles into user-defined micro-patterns. This study contributed towards better understanding of the particle transfer, interaction, and assembly behavior of a system of magnetic and nonmagnetic particles and towards identifying the dominant forces directing the assembly.

6.3 Recommendation for future work

- The magnetic field directed assembly was performed on spherical and polygonal particle shapes. Incorporating particles with different form aspects, i.e. tubular or sheet form, may expand the capabilities of tailoring the final deposition structure. Those particles may, however, have different responsive assembly behavior. For this reason, the assembly and deposition kinetics of particles with different form factor needs to be investigated.
- The magnetic field gradient distribution on a deposition substrate surface affects the deposition structure morphology, which is highly dependent on the protrusion geometry (e. g. height, width, and cross section profile), and the pattern spacing. Therefore, a systematic study is required to offer better understanding of the effect of those parameters on the deposition structure.
- This approach may be successfully used in fabricating metal matrix composites with custom design structures. For this reason, fabrication of laminate MMCs with micro-pattern structure using field assisted deposition needs to be investigated. The metallurgical compatibility of the matrix material and the deposited particles (the magnetic and/or the nonmagnetic particles) needs to be considered. The corresponding densification conditions need to be determined.

6.4 Acknowledgement

The authors greatly appreciate the financial support from Defense Advanced Research Projects Agency (N66001-12-1-4257) and the United States National Science Foundation (CMMI-1030120) and (CMMI-1502900).

APPENDIX : SAFE HANDLING OF NANOPARTICLES

Background

Although insufficient information exists to predict the health hazard posed by the exposure to nanoparticles, current research indicates that exposure via inhalation and skin contact can result in these particles entering the body. Nanoparticles have the greatest potential to enter the body if they are in the form of individual particles, agglomerates of nanoparticles, and particles from nanostructured materials that become airborne or come into contact with the skin. Moreover, particles with high reactivity or high affinity to oxidation may ignite causing fire or explosion.

According to The National Institute for Occupational Safety and Health (NIOSH), the following workplace tasks may increase the risk of exposure to nanoparticles:

1. Working with nanoparticles in liquid media without adequate protection (e.g., gloves) will increase the risk of skin exposure.
2. Working with nanoparticles in liquid media during pouring or mixing operations, or where a high degree of agitation is involved, will lead to an increased likelihood of inhalation and respirable droplets being formed.
3. Generating nanoparticles in the gas phase in non-enclosed systems will increase the chances of aerosol release to the workplace.
4. Handling nano-structured powders will lead to the possibility of aerosolization.
5. Maintenance on equipment and processes used to produce or fabricate nanoparticles will pose a potential exposure risk to workers performing these tasks.
6. Cleaning of dust collection systems used to capture nanoparticles will pose a potential for both skin and inhalation exposure.

Control procedures

The following engineering, work practice and ventilation controls are required when handling nanoparticles to reduce potential exposure and ensure safe conditions in Iowa State University laboratories.

Lab protection and hygiene

1. Lab coat must be worn by the nanoparticle users.
2. Arm sleeves are required where high levels of exposure or splashes of solutions containing nanoparticles are anticipated.
3. Safety glasses must be worn while working in the lab.
4. Disposable gloves must be worn when handling nano-materials.
5. Long pants and closed toed shoes are required.
6. Respirators are required.
7. Particles with high oxidation affinity should be handled into a glove box to avoid particle ignition. Vacuum or inert gas environments are preferred to handle those particles.

Ventilation controls

Labs that handle nanoparticles must have non-recirculating ventilation systems. Activities that are likely to release nanoparticles (such as the opening and emptying of nanoparticle containers, weighing of dry nanoparticles, preparing suspension systems, and spraying) should not be performed on the open bench. These activities should be performed in a fume hood, a glove box, or a vented enclosure.

REFERENCES

- [1] L.L. Mishnaevsky Jr, Automatic voxel-based generation of 3D microstructural FE models and its application to the damage analysis of composites, *Materials Science and Engineering: A*, 407 (2005) 11-23.
- [2] L.L. Mishnaevsky Jr, Three-dimensional numerical testing of microstructures of particle reinforced composites, *Acta Materialia*, 52 (2004) 4177-4188.
- [3] L. Mishnaevsky Jr, K. Derrien, D. Baptiste, Effect of microstructure of particle reinforced composites on the damage evolution: probabilistic and numerical analysis, *Composites Science and Technology*, 64 (2004) 1805-1818.
- [4] L. Mishnaevsky Jr, G. Dai, Hybrid and hierarchical nanoreinforced polymer composites: Computational modelling of structure-properties relationships, *Composite Structures*, 117 (2014) 156-168.
- [5] K.S. Katti, D.R. Katti, Why is nacre so tough and strong?, *Materials Science and Engineering: C*, 26 (2006) 1317-1324.
- [6] L. Mishnaevsky Jr, U. Weber, S. Schmauder, Numerical analysis of the effect of microstructures of particle-reinforced metallic materials on the crack growth and fracture resistance, *Int J Fract*, 125 (2004) 33-50.
- [7] L. Mishnaevsky Jr, Nanostructured interfaces for enhancing mechanical properties of composites: Computational micromechanical studies, *Composites Part B: Engineering*, 68 (2015) 75-84.

- [8] X. Zeng, L. Ye, S. Yu, H. Li, R. Sun, J. Xu, C.-P. Wong, Artificial nacre-like papers based on noncovalent functionalized boron nitride nanosheets with excellent mechanical and thermally conductive properties, *Nanoscale*, 7 (2015) 6774-6781.
- [9] H.-B. Yao, H.-Y. Fang, X.-H. Wang, S.-H. Yu, Hierarchical assembly of micro-/nano-building blocks: bio-inspired rigid structural functional materials, *Chemical Society Reviews*, 40 (2011) 3764-3785.
- [10] S. Huang, S.L. Phua, W. Liu, G. Ding, X. Lu, Nacre-like composite films based on mussel-inspired 'glue' and nanoclay, *RSC Advances*, 4 (2014) 1425-1431.
- [11] Y. Wu, R. Cao, L. Ji, W. Huang, X. Yang, Y. Tu, Synergistic toughening of bioinspired artificial nacre by polystyrene grafted graphene oxide, *RSC Advances*, 5 (2015) 28085-28091.
- [12] W. Hao, L. Zhang, X. Wang, J. Wang, Z. Hu, W. Yang, Tough and strong nacre-like composites from hyperbranched poly(amido amine) and clay nanosheets cross-linked by genipin, *RSC Advances*, 6 (2016) 1415-1421.
- [13] Z. Li, Q. Guo, Z. Li, G. Fan, D.-B. Xiong, Y. Su, J. Zhang, D. Zhang, Enhanced Mechanical Properties of Graphene (Reduced Graphene Oxide)/Aluminum Composites with a Bioinspired Nanolaminated Structure, *Nano Lett*, 15 (2015) 8077-8083.
- [14] A.M.K. Esawi, M.A. El Borady, Carbon nanotube-reinforced aluminium strips, *Composites Science and Technology*, 68 (2008) 486-492.
- [15] H.J. Choi, G.B. Kwon, G.Y. Lee, D.H. Bae, Reinforcement with carbon nanotubes in aluminum matrix composites, *Scripta Mater*, 59 (2008) 360-363.

- [16] A.M.K. Esawi, K. Morsi, A. Sayed, A.A. Gawad, P. Borah, Fabrication and properties of dispersed carbon nanotube-aluminum composites, *Mat Sci Eng a-Struct*, 508 (2009) 167-173.
- [17] I. Ozdemir, S. Ahrens, S. Mücklich, B. Wielage, Nanocrystalline Al–Al₂O₃p and SiCp composites produced by high-energy ball milling, *Journal of Materials Processing Technology*, 205 (2008) 111-118.
- [18] M. Bastwros, G.-Y. Kim, C. Zhu, K. Zhang, S. Wang, X. Tang, X. Wang, Effect of ball milling on graphene reinforced Al6061 composite fabricated by semi-solid sintering, *Composites Part B: Engineering*, 60 (2014) 111-118.
- [19] C.N. He, N.Q. Zhao, C.S. Shi, X.W. Du, J.J. Li, H.P. Li, Q.R. Cui, An approach to obtaining homogeneously dispersed carbon nanotubes in Al powders for preparing reinforced Al-matrix composites, *Adv Mater*, 19 (2007) 1128-1132.
- [20] T. Kuzumaki, K. Miyazawa, H. Ichinose, K. Ito, Processing of carbon nanotube reinforced aluminum composite, *J Mater Res*, 13 (1998) 2445-2449.
- [21] H. Kwon, M. Estili, K. Takagi, T. Miyazaki, A. Kawasaki, Combination of hot extrusion and spark plasma sintering for producing carbon nanotube reinforced aluminum matrix composites, *Carbon*, 47 (2009) 570-577.
- [22] B. Ogel, R. Gurbuz, Microstructural characterization and tensile properties of hot pressed Al–SiC composites prepared from pure Al and Cu powders, *Materials Science and Engineering: A*, 301 (2001) 213-220.

- [23] M. Ravichandran, A. Naveen Sait, V. Anandakrishnan, Synthesis and forming characteristics of Al-TiO₂ powder metallurgy composites during cold upsetting under plane stress state conditions, *Journal of Sandwich Structures and Materials*, (2015).
- [24] T. Noguchi, A. Magario, S. Fukazawa, S. Shimizu, J. Beppu, M. Seki, Carbon nanotube/aluminium composites with uniform dispersion, *Mater Trans*, 45 (2004) 602-604.
- [25] E. Candan, H. Ahlatci, H. Çimenoglu, Abrasive wear behaviour of Al-SiC composites produced by pressure infiltration technique, *Wear*, 247 (2001) 133-138.
- [26] A. Fadavi Boostani, S. Tahamtan, Z.Y. Jiang, D. Wei, S. Yazdani, R. Azari Khosroshahi, R. Taherzadeh Mousavian, J. Xu, X. Zhang, D. Gong, Enhanced tensile properties of aluminium matrix composites reinforced with graphene encapsulated SiC nanoparticles, *Composites Part A: Applied Science and Manufacturing*, 68 (2015) 155-163.
- [27] C.F. Deng, X.X. Zhang, D.Z. Wang, Q. Lin, A.B. Li, Preparation and characterization of carbon nanotubes/aluminum matrix composites, *Mater Lett*, 61 (2007) 1725-1728.
- [28] L.M. Tham, M. Gupta, L. Cheng, Effect of reinforcement volume fraction on the evolution of reinforcement size during the extrusion of Al-SiC composites, *Materials Science and Engineering: A*, 326 (2002) 355-363.
- [29] R. Lakes, Materials with structural hierarchy, *Nature*, 361 (1993) 511-515.
- [30] A. Esawi, K. Morsi, Dispersion of carbon nanotubes (CNTs) in aluminum powder, *Composites Part A: Applied Science and Manufacturing*, 38 (2007) 646-650.
- [31] N. Darsono, D.-H. Yoon, J. Kim, Milling and dispersion of multi-walled carbon nanotubes in texanol, *Applied Surface Science*, 254 (2008) 3412-3419.

- [32] J. Liao, M.-J. Tan, Mixing of carbon nanotubes (CNTs) and aluminum powder for powder metallurgy use, *Powder Technology*, 208 (2011) 42-48.
- [33] B. Munkhbayar, M.J. Nine, J. Jeoun, M. Bat-Erdene, H. Chung, H. Jeong, Influence of dry and wet ball milling on dispersion characteristics of the multi-walled carbon nanotubes in aqueous solution with and without surfactant, *Powder Technology*, 234 (2013) 132-140.
- [34] Z.Y. Liu, S.J. Xu, B.L. Xiao, P. Xue, W.G. Wang, Z.Y. Ma, Effect of ball-milling time on mechanical properties of carbon nanotubes reinforced aluminum matrix composites, *Composites Part A: Applied Science and Manufacturing*, 43 (2012) 2161-2168.
- [35] L. Wang, H. Choi, J.-M. Myoung, W. Lee, Mechanical alloying of multi-walled carbon nanotubes and aluminium powders for the preparation of carbon/metal composites, *Carbon*, 47 (2009) 3427-3433.
- [36] Y. Wu, G.-Y. Kim, Carbon nanotube reinforced aluminum composite fabricated by semi-solid powder processing, *Journal of Materials Processing Technology*, 211 (2011) 1341-1347.
- [37] A.M.K. Esawi, K. Morsi, A. Sayed, M. Taher, S. Lanka, The influence of carbon nanotube (CNT) morphology and diameter on the processing and properties of CNT-reinforced aluminium composites, *Composites Part A: Applied Science and Manufacturing*, 42 (2011) 234-243.
- [38] J. Wang, Z. Li, G. Fan, H. Pan, Z. Chen, D. Zhang, Reinforcement with graphene nanosheets in aluminum matrix composites, *Scripta Mater*, 66 (2012) 594-597.
- [39] Y. Wu, G.-Y. Kim, A.M. Russell, Effects of mechanical alloying on an Al6061–CNT composite fabricated by semi-solid powder processing, *Materials Science and Engineering: A*, 538 (2012) 164-172.

- [40] C. Velez, I. Torres-Díaz, L. Maldonado-Camargo, C. Rinaldi, D.P. Arnold, Magnetic Assembly and Cross-Linking of Nanoparticles for Releasable Magnetic Microstructures, *ACS Nano*, 9 (2015) 10165-10172.
- [41] Q. Zhang, M. Janner, L. He, M. Wang, Y. Hu, Y. Lu, Y. Yin, Photonic Labyrinths: Two-Dimensional Dynamic Magnetic Assembly and in Situ Solidification, *Nano Lett*, 13 (2013) 1770-1775.
- [42] L. Ye, T. Pearson, C. Dolbashian, P. Pstrak, A.R. Mohtasebzadeh, B. Fellows, O.T. Mefford, T.M. Crawford, Magnetic-Field-Directed Self-Assembly of Programmable Mesoscale Shapes, *Advanced Functional Materials*, (2016) n/a-n/a.
- [43] R. George, K.T. Kashyap, R. Rahul, S. Yamdagni, Strengthening in carbon nanotube/aluminium (CNT/Al) composites, *Scripta Mater*, 53 (2005) 1159-1163.
- [44] A.M.K. Esawi, K. Morsi, A. Sayed, M. Taher, S. Lanka, Effect of carbon nanotube (CNT) content on the mechanical properties of CNT-reinforced aluminium composites, *Composites Science and Technology*, 70 (2010) 2237-2241.
- [45] S.F. Bartolucci, J. Paras, M.A. Rafiee, J. Rafiee, S. Lee, D. Kapoor, N. Koratkar, Graphene–aluminum nanocomposites, *Materials Science and Engineering: A*, 528 (2011) 7933-7937.
- [46] D.H. Nam, Y.K. Kim, S.I. Cha, S.H. Hong, Effect of CNTs on precipitation hardening behavior of CNT/Al–Cu composites, *Carbon*, 50 (2012) 4809-4814.
- [47] S. Gopalakrishnan, N. Murugan, Production and wear characterisation of AA 6061 matrix titanium carbide particulate reinforced composite by enhanced stir casting method, *Composites Part B: Engineering*, 43 (2012) 302-308.

- [48] A. Baradeswaran, A. Elaya Perumal, Study on mechanical and wear properties of Al 7075/Al₂O₃/graphite hybrid composites, *Composites Part B: Engineering*, 56 (2014) 464-471.
- [49] B. Peng, M. Locascio, P. Zapol, S. Li, S.L. Mielke, G.C. Schatz, H.D. Espinosa, Measurements of near-ultimate strength for multiwalled carbon nanotubes and irradiation-induced crosslinking improvements, *Nature nanotechnology*, 3 (2008) 626.
- [50] F. Gardea, D.C. Lagoudas, Characterization of Electrical and Thermal Properties of Carbon Nanotube/Epoxy Composites, *Composites Part B: Engineering*.
- [51] J.K. Chen, I.S. Huang, Thermal properties of aluminum–graphite composites by powder metallurgy, *Composites Part B: Engineering*, 44 (2013) 698-703.
- [52] C. Balázs, B. Fényi, N. Hegman, Z. Kövér, F. Wéber, Z. Vértesy, Z. Kónya, I. Kiricsi, L.P. Biró, P. Arató, Development of CNT/Si₃N₄ composites with improved mechanical and electrical properties, *Composites Part B: Engineering*, 37 (2006) 418-424.
- [53] M.M.H. Bastwros, A.M.K. Esawi, A. Wifi, Friction and wear behavior of Al–CNT composites, *Wear*, 307 (2013) 164-173.
- [54] A. Baradeswaran, A.E. Perumal, Wear and mechanical characteristics of Al 7075/graphite composites, *Composites Part B: Engineering*, 56 (2014) 472-476.
- [55] R. Pérez-Bustamante, F. Pérez-Bustamante, I. Estrada-Guel, L. Licea-Jiménez, M. Miki-Yoshida, R. Martínez-Sánchez, Effect of milling time and CNT concentration on hardness of CNT/Al₂O₃ composites produced by mechanical alloying, *Materials Characterization*, (2013).

- [56] D.K. Lim, T. Shibayanagi, A.P. Gerlich, Synthesis of multi-walled CNT reinforced aluminium alloy composite via friction stir processing, *Materials Science and Engineering: A*, 507 (2009) 194-199.
- [57] D. Lahiri, S.R. Bakshi, A.K. Keshri, Y. Liu, A. Agarwal, Dual strengthening mechanisms induced by carbon nanotubes in roll bonded aluminum composites, *Materials Science and Engineering: A*, 523 (2009) 263-270.
- [58] Y. Jang, S. Kim, S. Lee, D. Kim, M. Um, Fabrication of carbon nano-sized fiber reinforced copper composite using liquid infiltration process, *Composites Science and Technology*, 65 (2005) 781-784.
- [59] S. Cho, K. Takagi, H. Kwon, D. Seo, K. Ogawa, K. Kikuchi, A. Kawasaki, Multi-walled carbon nanotube-reinforced copper nanocomposite coating fabricated by low-pressure cold spray process, *Surface and Coatings Technology*, 206 (2012) 3488-3494.
- [60] K. Morsi, A.M.K. Esawi, P. Borah, S. Lanka, A. Sayed, M. Taher, Properties of single and dual matrix aluminum-carbon nanotube composites processed via spark plasma extrusion (SPE), *Materials Science and Engineering: A*, 527 (2010) 5686-5690.
- [61] S.B. Lee, K. Matsunaga, Y. Ikuhara, S.-K. Lee, Effect of alloying elements on the interfacial bonding strength and electric conductivity of carbon nano-fiber reinforced Cu matrix composites, *Materials Science and Engineering: A*, 449-451 (2007) 778-781.
- [62] R. Pérez-Bustamante, D. Bolaños-Morales, J. Bonilla-Martínez, I. Estrada-Guel, R. Martínez-Sánchez, Microstructural and hardness behavior of graphene-nanoplatelets/aluminum composites

synthesized by mechanical alloying, *Journal of Alloys and Compounds*, 615, Supplement 1 (2014) S578-S582.

[63] H. Zhang, C. Xu, W. Xiao, K. Ameyama, C. Ma, Enhanced mechanical properties of Al5083 alloy with graphene nanoplates prepared by ball milling and hot extrusion, *Materials Science and Engineering: A*, 658 (2016) 8-15.

[64] S. Wang, M. Tambraparni, J. Qiu, J. Tipton, D. Dean, Thermal Expansion of Graphene Composites, *Macromolecules*, 42 (2009) 5251-5255.

[65] A.C. Ferrari, J. Robertson, Interpretation of Raman spectra of disordered and amorphous carbon, *Phys Rev B*, 61 (2000) 14095-14107.

[66] D. Graf, F. Molitor, K. Ensslin, C. Stampfer, A. Jungen, C. Hierold, L. Wirtz, Spatially resolved raman spectroscopy of single- and few-layer graphene, *Nano Lett*, 7 (2007) 238-242.

[67] T.M.G. Mohiuddin, A. Lombardo, R.R. Nair, A. Bonetti, G. Savini, R. Jalil, N. Bonini, D.M. Basko, C. Galotis, N. Marzari, K.S. Novoselov, A.K. Geim, A.C. Ferrari, Uniaxial strain in graphene by Raman spectroscopy: G peak splitting, Grüneisen parameters, and sample orientation, *Phys Rev B*, 79 (2009) 205433.

[68] C. Suryanarayana, Mechanical alloying and milling, *Progress in Materials Science*, 46 (2001) 1-184.

[69] I.-Y. Kim, J.-H. Lee, G.-S. Lee, S.-H. Baik, Y.-J. Kim, Y.-Z. Lee, Friction and wear characteristics of the carbon nanotube–aluminum composites with different manufacturing conditions, *Wear*, 267 (2009) 593-598.

- [70] J. Jin-long, W. Hai-zhong, Y. hua, X. Jin-cheng, Fabrication and wear behavior of CNT/Al composites, *Transactions of Nonferrous Metals Society of China*, 17 (2007) s113-s116.
- [71] L. Jun, L. Ying, L. Lixian, Y. Xuejuan, Mechanical properties and oil content of CNT reinforced porous CuSn oil bearings, *Composites Part B: Engineering*, 43 (2012) 1681-1686.
- [72] C. Lee, X. Wei, J.W. Kysar, J. Hone, Measurement of the Elastic Properties and Intrinsic Strength of Monolayer Graphene, *Science*, 321 (2008) 385.
- [73] L. Liu, J. Zhang, J. Zhao, F. Liu, Mechanical properties of graphene oxides, *Nanoscale*, 4 (2012) 5910-5916.
- [74] J. Zhang, S. Ju, D. Jiang, H.-X. Peng, Reducing dispersity of mechanical properties of carbon fiber/epoxy composites by introducing multi-walled carbon nanotubes, *Composites Part B: Engineering*, 54 (2013) 371-376.
- [75] L. Hao, D. Zhou, Q. Fu, Y. Hu, Multiferroic properties of multilayered BaTiO₃-CoFe₂O₄ composites via tape casting method, *J Mater Sci*, 48 (2013) 178-185.
- [76] D. Bémer, R. Régnier, Y. Morele, F. Gripari, J.-C. Appert-collin, D. Thomas, Study of clogging and cleaning cycles of a pleated cartridge filter used in a thermal spraying process to filter ultrafine particles, *Powder Technology*, 234 (2013) 1-6.
- [77] R. Hui, Z. Wang, O. Kesler, L. Rose, J. Jankovic, S. Yick, R. Maric, D. Ghosh, Thermal plasma spraying for SOFCs: Applications, potential advantages, and challenges, *Journal of Power Sources*, 170 (2007) 308-323.

- [78] S.-R. Li, N. Yesibolati, Y. Qiao, S.-Y. Ge, X.-Y. Feng, J.-F. Zhu, C.-H. Chen, Electrostatic spray deposition of porous Fe₂V₄O₁₃ films as electrodes for Li-ion batteries, *Journal of Alloys and Compounds*, 520 (2012) 77-82.
- [79] I. Concina, N. Memarian, G.S. Selopal, M.M. Natile, G. Sberveglieri, A. Vomiero, Spray-assisted silar deposition of cadmium sulphide quantum dots on metal oxide films for excitonic solar cells, *Journal of Power Sources*, 240 (2013) 736-744.
- [80] A. López, D. Acosta, A. I. Martínez, J. Santiago, Nanostructured low crystallized titanium dioxide thin films with good photocatalytic activity, *Powder Technology*, 202 (2010) 111-117.
- [81] L. Liu, G.-Y. Kim, A. Chandra, Fabrication of solid oxide fuel cell anode electrode by spray pyrolysis, *Journal of Power Sources*, 195 (2010) 7046-7053.
- [82] M. Dobre, L. Bolle, Practical design of ultrasonic spray devices: experimental testing of several atomizer geometries, *Experimental Thermal and Fluid Science*, 26 (2002) 205-211.
- [83] B. Barua, M.C. Saha, Ultrasound Assisted Hybrid Carbon Epoxy Composites Containing Carbon Nanotubes, *Journal of Engineering Materials and Technology*, 135 (2013) 011009-011009.
- [84] C. Agashe, M.G. Takwale, B.R. Marathe, V.G. Bhide, Structural properties of SnO₂: F films deposited by spray pyrolysis, *Solar Energy Materials*, 17 (1988) 99-117.
- [85] P.S. Patil, Versatility of chemical spray pyrolysis technique, *Materials Chemistry and Physics*, 59 (1999) 185-198.
- [86] U.P. Muecke, G.L. Messing, L.J. Gauckler, The Leidenfrost effect during spray pyrolysis of nickel oxide-gadolinia doped ceria composite thin films, *Thin Solid Films*, 517 (2009) 1515-1521.

- [87] F. Ely, A. Matsumoto, B. Zoetebier, V.S. Peressinotto, M.K. Hirata, D.A. de Sousa, R. Maciel, Handheld and automated ultrasonic spray deposition of conductive PEDOT:PSS films and their application in AC EL devices, *Organic Electronics*, 15 (2014) 1062-1070.
- [88] L. Liu, G.-Y. Kim, A.C. Hillier, A. Chandra, Microstructural and electrochemical impedance study of nickel–Ce_{0.9}Gd_{0.1}O_{1.95} anodes for solid oxide fuel cells fabricated by ultrasonic spray pyrolysis, *Journal of Power Sources*, 196 (2011) 3026-3032.
- [89] M. Valdés, G. Santoro, M. Vázquez, Spray deposition of Cu₂ZnSnS₄ thin films, *Journal of Alloys and Compounds*, 585 (2014) 776-782.
- [90] J. Yao, Y. He, D. Wang, J. Lin, High-temperature oxidation resistance of (Al₂O₃–Y₂O₃)/(Y₂O₃-stabilized ZrO₂) laminated coating on 8Nb–TiAl alloy prepared by a novel spray pyrolysis, *Corrosion Science*, 80 (2014) 19-27.
- [91] C.-H. Jung, J. Yun, K. Qadir, B. Naik, J.-Y. Yun, J.Y. Park, Catalytic activity of Pt/SiO₂ nanocatalysts synthesized via ultrasonic spray pyrolysis process under CO oxidation, *Applied Catalysis B: Environmental*, 154–155 (2014) 171-176.
- [92] C.-P. Li, F. Lin, R.M. Richards, C. Engtrakul, R.C. Tenent, C.A. Wolden, The influence of sol–gel processing on the electrochromic properties of mesoporous WO₃ films produced by ultrasonic spray deposition, *Solar Energy Materials and Solar Cells*, 121 (2014) 163-170.
- [93] M. Dobre, L. Bolle, Visualisation and analysis of liquid film surface patterns formed on ultrasonic atomisers, *ILASS-Europe'99*, (1999).
- [94] O. Wilhelm, S.E. Pratsinis, D. Perednis, L.J. Gauckler, Electro spray and pressurized spray deposition of yttria-stabilized zirconia films, *Thin Solid Films*, 479 (2005) 121-129.

- [95] R.P. Reolon, C.M. Halmenschlager, R. Neagu, C. de Fraga Malfatti, C.P. Bergmann, Electrochemical performance of gadolinia-doped ceria (CGO) electrolyte thin films for ITSOFC deposited by spray pyrolysis, *Journal of Power Sources*, 261 (2014) 348-355.
- [96] S.K. Das, S.U.S. Choi, H.E. Patel, Heat Transfer in Nanofluids—A Review, *Heat Transfer Engineering*, 27 (2006) 3-19.
- [97] M. Jones, C. Li, A. Afjeh, G. Peterson, Experimental study of combustion characteristics of nanoscale metal and metal oxide additives in biofuel (ethanol), *Nanoscale Research Letters*, 6 (2011) 246.
- [98] V. Sridhara, L. Satapathy, Al₂O₃-based nanofluids: a review, *Nanoscale Research Letters*, 6 (2011) 1-16.
- [99] A.D. Willey, J.M. Holt, B.A. Larsen, J.L. Blackburn, S. Liddiard, J. Abbott, M. Coffin, R.R. Vanfleet, R.C. Davis, Thin films of carbon nanotubes via ultrasonic spraying of suspensions in N-methyl-2-pyrrolidone and N-cyclohexyl-2-pyrrolidone, *Journal of Vacuum Science and technology B*, 32 (2014) 011218.
- [100] B. Faure, J. Sæderup Lindeløv, M. Wahlberg, N. Adkins, P. Jackson, L. Bergström, Spray drying of TiO₂ nanoparticles into redispersible granules, *Powder Technology*, 203 (2010) 384-388.
- [101] H.-m. Bian, Y. Yang, Y. Wang, W. Tian, Preparation of nanostructured alumina–titania composite powders by spray drying, heat treatment and plasma treatment, *Powder Technology*, 219 (2012) 257-263.

- [102] K. Kho, K. Hadinoto, Aqueous re-dispersibility characterization of spray-dried hollow spherical silica nano-aggregates, *Powder Technology*, 198 (2010) 354-363.
- [103] P. Roy, G. Bertrand, C. Coddet, Spray drying and sintering of zirconia based hollow powders, *Powder Technology*, 157 (2005) 20-26.
- [104] A.B.D. Nandiyanto, K. Okuyama, Progress in developing spray-drying methods for the production of controlled morphology particles: From the nanometer to submicrometer size ranges, *Advanced Powder Technology*, 22 (2011) 1-19.
- [105] N. Ferrer-Anglada, V. Gomis, Z. El-Hachemi, U.D. Weglikovska, M. Kaempgen, S. Roth, Carbon nanotube based composites for electronic applications: CNT-conducting polymers, CNT-Cu, *physica status solidi (a)*, 203 (2006) 1082-1087.
- [106] H. Erismis, D. Nemeč, M. Geiss, V. Skakalova, U. Ritter, I. Kolaric, S. Roth, Penetration based CNT/Sol-Gel composite films and their remarkable electrical properties, *Microelectronic Engineering*, 88 (2011) 2513-2515.
- [107] S.I. Cha, B.K. Koo, S.H. Seo, D.Y. Lee, Pt-free transparent counter electrodes for dye-sensitized solar cells prepared from carbon nanotube micro-balls, *Journal of Materials Chemistry*, 20 (2010) 659-662.
- [108] Y. Liu, S. Zha, M. Liu, Nanocomposite Electrodes Fabricated by a Particle-Solution Spraying Process for Low-Temperature SOFCs, *Chemistry of Materials*, 16 (2004) 3502-3506.
- [109] L.B. Modesto-López, M. Miettinen, T. Torvela, A. Lähde, J. Jokiniemi, Direct deposition of graphene nanomaterial films on polymer-coated glass by ultrasonic spraying, *Thin Solid Films*, 578 (2015) 45-52.

- [110] S. Lee, T. Oyama, J. Wadsworth, O.D. Sherby, Impact properties of a laminated composite based on ultrahigh carbon steel and brass, *Materials Science and Engineering: A*, 154 (1992) 133-137.
- [111] M. Pozuelo, F. Carreño, O.A. Ruano, Delamination effect on the impact toughness of an ultrahigh carbon–mild steel laminate composite, *Composites Science and Technology*, 66 (2006) 2671-2676.
- [112] P.B. Hoffman, J.C. Gibeling, Near-threshold fatigue crack growth in aluminum composite laminates, *Scripta Metallurgica et Materialia*, 32 (1995) 901-906.
- [113] D.R. Lesuer, C.K. Syn, O.D. Sherby, J. Wadsworth, J.J. Lewandowski, W.H. Hunt, Mechanical behaviour of laminated metal composites, *International Materials Reviews*, 41 (1996) 169-197.
- [114] M. Samadzadeh, M. Toroghinejad, The Influence of Carbon Nanotube and Roll Bonding Parameters on the Bond Strength of Al Sheets, *J. of Materi Eng and Perform*, 23 (2014) 1887-1895.
- [115] M. Rezayat, A. Akbarzadeh, A. Owhadi, Fabrication of High-Strength Al/SiC p Nanocomposite Sheets by Accumulative Roll Bonding, *Metall and Mat Trans A*, 43 (2012) 2085-2093.
- [116] C.W. Schmidt, C. Knieke, V. Maier, H.W. Höppel, W. Peukert, M. Göken, Accelerated grain refinement during accumulative roll bonding by nanoparticle reinforcement, *Scripta Mater*, 64 (2011) 245-248.

- [117] J.-K. Kim, J.Y. Jung, Y.T. Kang, The effect of nano-particles on the bubble absorption performance in a binary nanofluid, *International Journal of Refrigeration*, 29 (2006) 22-29.
- [118] R.-H. Chen, T.X. Phuoc, D. Martello, Surface tension of evaporating nanofluid droplets, *International Journal of Heat and Mass Transfer*, 54 (2011) 2459-2466.
- [119] V. Jokanović, D. Janačković, D. Uskoković, Influence of aerosol formation mechanism by an ultrasonic field on particle size distribution of ceramic powders, *Ultrasonics Sonochemistry*, 6 (1999) 157-169.
- [120] D.S. Zhu, S.Y. Wu, N. Wang, Surface Tension and Viscosity of Aluminum Oxide Nanofluids, *AIP Conference Proceedings*, 1207 (2010) 460-464.
- [121] S. Tanvir, L. Qiao, Surface tension of Nanofluid-type fuels containing suspended nanomaterials, *Nanoscale Research Letters*, 7 (2012) 1-10.
- [122] V. Saeid, P. Arup, J. Abhishek, R. Ganapathiraman, B.-T. Theodorian, The effect of nanoparticles on the liquid–gas surface tension of Bi₂Te₃ nanofluids, *Nanotechnology*, 20 (2009) 185702.
- [123] R. Kumar, D. Milanova, Effect of surface tension on nanotube nanofluids, *Applied Physics Letters*, 94 (2009) -.
- [124] K.X. Steirer, M.O. Reese, B.L. Rupert, N. Kopidakis, D.C. Olson, R.T. Collins, D.S. Ginley, Ultrasonic spray deposition for production of organic solar cells, *Solar Energy Materials and Solar Cells*, 93 (2009) 447-453.
- [125] M. Byun, N.B. Bowden, Z. Lin, Hierarchically Organized Structures Engineered from Controlled Evaporative Self-Assembly, *Nano Lett*, 10 (2010) 3111-3117.

- [126] D.D. Robert, B. Olgica, F.D. Todd, H. Greb, R.N. Sidney, A.W. Thomas, Capillary flow as the cause of ring stains from dried liquid drops, *Nature*, 389 (1997) 827-829.
- [127] O. Naoki, Y. Yeong, D. Isobel, Fabrication of Gas Electrodes by Wet Powder Spraying of Binder-Free Particle Suspensions Using a Pulse Injection Process, *Journal of the American Ceramic Society*, 90 (2007) 1365-1369.
- [128] U.P. Muecke, N. Luechinger, L. Schlagenhauf, L.J. Gauckler, Initial stages of deposition and film formation during spray pyrolysis — Nickel oxide, cerium gadolinium oxide and mixtures thereof, *Thin Solid Films*, 517 (2009) 1522-1529.
- [129] E. Pauliac-Vaujour, A. Stannard, C.P. Martin, M.O. Blunt, I. Notinger, P.J. Moriarty, I. Vancea, U. Thiele, Fingering Instabilities in Dewetting Nanofluids, *Physical Review Letters*, 100 (2008) 176102.
- [130] R.P. Reolon, C.M. Halmenschlager, R. Neagu, C. de Fraga Malfatti, C.P. Bergmann, Electrochemical Performance Of Gadolinia-Doped Ceria (CGO) Electrolyte Thin Films For Itsoc Deposited By Spray Pyrolysis, *Journal of Power Sources*.
- [131] D. Perednis, L. Gauckler, Thin Film Deposition Using Spray Pyrolysis, *J Electroceram*, 14 (2005) 103-111.
- [132] D. Ragazzon, A. Nakaruk, C.C. Sorrell, Deposition rate of anatase films by ultrasonic spray pyrolysis, *Advances in Applied Ceramics*, 109 (2010) 196-199.
- [133] P. Fratzl, R. Weinkamer, Nature's hierarchical materials, *Progress in Materials Science*, 52 (2007) 1263-1334.

- [134] H. Gao, Application of Fracture Mechanics Concepts to Hierarchical Biomechanics of Bone and Bone-like Materials, *Int J Fract*, 138 (2006) 101-137.
- [135] P.R. Rao, Biomimetics, *Sadhana*, 28 (2003) 657-676.
- [136] M.A. Meyers, P.-Y. Chen, A.Y.-M. Lin, Y. Seki, Biological materials: Structure and mechanical properties, *Progress in Materials Science*, 53 (2008) 1-206.
- [137] L. Mishnaevsky Jr, Micromechanics of hierarchical materials: a brief overview, *Rev. Adv. Mater. Sci*, 30 (2012) 60-72.
- [138] R.Z. Wang, Z. Suo, A.G. Evans, N. Yao, I.A. Aksay, Deformation mechanisms in nacre, *J Mater Res*, 16 (2001) 2485-2493.
- [139] A.P. Jackson, J.F.V. Vincent, R.M. Turner, The Mechanical Design of Nacre, *Proceedings of the Royal Society of London B: Biological Sciences*, 234 (1988) 415-440.
- [140] M. Bastwros, G.-Y. Kim, Fabrication of Aluminum–SiC Laminate Nanocomposite by Ultrasonic Spray Deposited Sheet Bonding¹, *Journal of Micro and Nano-Manufacturing*, 3 (2015) 031005-031005.
- [141] M. Bastwros, G.-Y. Kim, Ultrasonic spray deposition of SiC nanoparticles for laminate metal composite fabrication, *Powder Technology*, 288 (2016) 279-285.
- [142] B. Ji, H. Gao, Mechanical properties of nanostructure of biological materials, *Journal of the Mechanics and Physics of Solids*, 52 (2004) 1963-1990.
- [143] D.R. Katti, S.M. Pradhan, K.S. Katti, Modeling the organic-inorganic interfacial nanoasperities in a model bio-nanocomposite, nacre, *Reviews on Advanced Materials Science*, 6 (2004) 162-168.

- [144] F. Song, Y.L. Bai, Effects of nanostructures on the fracture strength of the interfaces in nacre, *J Mater Res*, 18 (2003) 1741-1744.
- [145] L.R. Xu, S. Sengupta, Interfacial Stress Transfer and Property Mismatch in Discontinuous Nanofiber/Nanotube Composite Materials, *Journal of Nanoscience and Nanotechnology*, 5 (2005) 620-626.
- [146] X. Xue, J. Wang, E.P. Furlani, Self-Assembly of Crystalline Structures of Magnetic Core–Shell Nanoparticles for Fabrication of Nanostructured Materials, *ACS Applied Materials & Interfaces*, 7 (2015) 22515-22524.
- [147] M.F.L. De Volder, S. Tawfick, S.J. Park, A.J. Hart, Corrugated Carbon Nanotube Microstructures with Geometrically Tunable Compliance, *ACS Nano*, 5 (2011) 7310-7317.
- [148] P. Li, Y. Li, Z.-K. Zhou, S. Tang, X.-F. Yu, S. Xiao, Z. Wu, Q. Xiao, Y. Zhao, H. Wang, P.K. Chu, Evaporative Self-Assembly of Gold Nanorods into Macroscopic 3D Plasmonic Superlattice Arrays, *Adv Mater*, 28 (2016) 2511-2517.
- [149] W. Han, Z. Lin, Learning from “Coffee Rings”: Ordered Structures Enabled by Controlled Evaporative Self-Assembly, *Angewandte Chemie International Edition*, 51 (2012) 1534-1546.
- [150] M. Holgado, F. García-Santamaría, A. Blanco, M. Ibisate, A. Cintas, H. Míguez, C.J. Serna, C. Molpeceres, J. Requena, A. Mifsud, F. Meseguer, C. López, Electrophoretic Deposition To Control Artificial Opal Growth, *Langmuir*, 15 (1999) 4701-4704.
- [151] M. De Volder, S.H. Tawfick, S.J. Park, D. Copic, Z. Zhao, W. Lu, A.J. Hart, Diverse 3D Microarchitectures Made by Capillary Forming of Carbon Nanotubes, *Adv Mater*, 22 (2010) 4384-4389.

- [152] P.V. Braun, R.W. Zehner, C.A. White, M.K. Weldon, C. Kloc, S.S. Patel, P. Wiltzius, Epitaxial Growth of High Dielectric Contrast Three-Dimensional Photonic Crystals, *Adv Mater*, 13 (2001) 721-724.
- [153] S.-K. Lee, G.-R. Yi, S.-M. Yang, High-speed fabrication of patterned colloidal photonic structures in centrifugal microfluidic chips, *Lab on a Chip*, 6 (2006) 1171-1177.
- [154] G. Pan, R. Kesavamoorthy, S.A. Asher, Nanosecond Switchable Polymerized Crystalline Colloidal Array Bragg Diffracting Materials, *Journal of the American Chemical Society*, 120 (1998) 6525-6530.
- [155] C.E. Reese, C.D. Guerrero, J.M. Weissman, K. Lee, S.A. Asher, Synthesis of Highly Charged, Monodisperse Polystyrene Colloidal Particles for the Fabrication of Photonic Crystals, *Journal of Colloid and Interface Science*, 232 (2000) 76-80.
- [156] M.F.L. De Volder, D.O. Vidaud, E.R. Meshot, S. Tawfick, A. John Hart, Self-similar organization of arrays of individual carbon nanotubes and carbon nanotube micropillars, *Microelectronic Engineering*, 87 (2010) 1233-1238.
- [157] E. Oh, J. Byun, B. Lee, S. Kim, D. Kim, J. Yoon, Y. Hong, Modulus-Gradient Conductive Core-Shell Structures Formed by Magnetic Self-Assembling and Printing Processes for Highly Stretchable Via Applications, *Advanced Electronic Materials*, (2017) 1600517-n/a.
- [158] V. Malik, A.V. Petukhov, L. He, Y. Yin, M. Schmidt, Colloidal Crystallization and Structural Changes in Suspensions of Silica/Magnetite Core-Shell Nanoparticles, *Langmuir*, 28 (2012) 14777-14783.

- [159] P. Vach, Actuation of Iron Oxide-Based Nanostructures by External Magnetic Fields, *Iron Oxides*, Wiley-VCH Verlag GmbH & Co. KGaA2016, pp. 523-544.
- [160] J. Kim, S.E. Chung, S.-E. Choi, H. Lee, J. Kim, S. Kwon, Programming magnetic anisotropy in polymeric microactuators, *Nat Mater*, 10 (2011) 747-752.
- [161] L. Ye, B. Terry, O.T. Mefford, C. Rinaldi, T.M. Crawford, All-nanoparticle concave diffraction grating fabricated by self-assembly onto magnetically-recorded templates, *Opt. Express*, 21 (2013) 1066-1075.
- [162] L. He, Y. Hu, H. Kim, J. Ge, S. Kwon, Y. Yin, Magnetic Assembly of Nonmagnetic Particles into Photonic Crystal Structures, *Nano Lett*, 10 (2010) 4708-4714.
- [163] M.D. Krebs, R.M. Erb, B.B. Yellen, B. Samanta, A. Bajaj, V.M. Rotello, E. Alsberg, Formation of Ordered Cellular Structures in Suspension via Label-Free Negative Magnetophoresis, *Nano Lett*, 9 (2009) 1812-1817.
- [164] G. Huang, M. Li, Q. Yang, Y. Li, H. Liu, H. Yang, F. Xu, Magnetically Actuated Droplet Manipulation and Its Potential Biomedical Applications, *ACS Applied Materials & Interfaces*, 9 (2017) 1155-1166.
- [165] A. Nelson, Q. Dai, Magnetically Responsive Self-Assembled Composite Materials, *Supramolecular Chemistry*, John Wiley & Sons, Ltd2012.
- [166] A.-S. Robbes, F. Cousin, F. Meneau, F. Dalmas, F. Boué, J. Jestin, Nanocomposite Materials with Controlled Anisotropic Reinforcement Triggered by Magnetic Self-Assembly, *Macromolecules*, 44 (2011) 8858-8865.

- [167] R.M. Erb, R. Libanori, N. Rothfuchs, A.R. Studart, Composites Reinforced in Three Dimensions by Using Low Magnetic Fields, *Science*, 335 (2012) 199.
- [168] K. Wang, C. Yi, X. Hu, C. Liu, Y. Sun, J. Hou, Y. Li, J. Zheng, S. Chuang, A. Karim, X. Gong, Enhanced Performance of Polymer Solar Cells using PEDOT:PSS Doped with Fe₃O₄ Magnetic Nanoparticles Aligned by an External Magnetostatic Field as an Anode Buffer Layer, *ACS Applied Materials & Interfaces*, 6 (2014) 13201-13208.
- [169] A.N. Shipway, E. Katz, I. Willner, Nanoparticle Arrays on Surfaces for Electronic, Optical, and Sensor Applications, *ChemPhysChem*, 1 (2000) 18-52.
- [170] P.D. Duncan, P.J. Camp, Structure and dynamics in a monolayer of dipolar spheres, *The Journal of Chemical Physics*, 121 (2004) 11322-11331.
- [171] J. Ge, L. He, J. Goebel, Y. Yin, Assembly of Magnetically Tunable Photonic Crystals in Nonpolar Solvents, *Journal of the American Chemical Society*, 131 (2009) 3484-3486.
- [172] J. Ge, Y. Hu, T. Zhang, T. Huynh, Y. Yin, Self-Assembly and Field-Responsive Optical Diffractions of Superparamagnetic Colloids, *Langmuir*, 24 (2008) 3671-3680.
- [173] H. Takahashi, D. Nagao, K. Watanabe, H. Ishii, M. Konno, Magnetic Field Aligned Assembly of Nonmagnetic Composite Dumbbells in Nanoparticle-Based Aqueous Ferrofluid, *Langmuir*, 31 (2015) 5590-5595.
- [174] H. Wang, Q.-W. Chen, L.-X. Sun, H.-p. Qi, X. Yang, S. Zhou, J. Xiong, Magnetic-Field-Induced Formation of One-Dimensional Magnetite Nanochains, *Langmuir*, 25 (2009) 7135-7139.

- [175] Y. Zhang, L. Sun, Y. Fu, Z.C. Huang, X.J. Bai, Y. Zhai, J. Du, H.R. Zhai, The Shape Anisotropy in the Magnetic Field-Assisted Self-Assembly Chain-like Structure of Magnetite, *The Journal of Physical Chemistry C*, 113 (2009) 8152-8157.
- [176] S. Kralj, D. Makovec, Magnetic Assembly of Superparamagnetic Iron Oxide Nanoparticle Clusters into Nanochains and Nanobundles, *ACS Nano*, 9 (2015) 9700-9707.
- [177] L. He, Y. Hu, X. Han, Y. Lu, Z. Lu, Y. Yin, Assembly and Photonic Properties of Superparamagnetic Colloids in Complex Magnetic Fields, *Langmuir*, 27 (2011) 13444-13450.
- [178] Y. Yang, L. Gao, G.P. Lopez, B.B. Yellen, Tunable Assembly of Colloidal Crystal Alloys Using Magnetic Nanoparticle Fluids, *ACS Nano*, 7 (2013) 2705-2716.
- [179] Y. Hu, L. He, Y. Yin, Magnetically Responsive Photonic Nanochains, *Angewandte Chemie International Edition*, 50 (2011) 3747-3750.
- [180] M. Wang, L. He, Y. Yin, Magnetic field guided colloidal assembly, *Materials Today*, 16 (2013) 110-116.
- [181] D. Li, S. Banon, S.L. Biswal, Bending dynamics of DNA-linked colloidal particle chains, *Soft Matter*, 6 (2010) 4197-4204.
- [182] J. Lim, D.X. Tan, F. Lanni, R.D. Tilton, S.A. Majetich, Optical imaging and magnetophoresis of nanorods, *Journal of Magnetism and Magnetic Materials*, 321 (2009) 1557-1562.
- [183] L. He, M. Wang, Q. Zhang, Y. Lu, Y. Yin, Magnetic Assembly and Patterning of General Nanoscale Materials through Nonmagnetic Templates, *Nano Lett*, 13 (2013) 264-271.

- [184] J.D. Love, On the van der Waals force between two spheres or a sphere and a wall, *Journal of the Chemical Society, Faraday Transactions 2: Molecular and Chemical Physics*, 73 (1977) 669-688.
- [185] J.N. Israelachvili, Chapter 13 - Van der Waals Forces between Particles and Surfaces, *Intermolecular and Surface Forces (Third Edition)*, Academic Press, San Diego, 2011, pp. 253-289.
- [186] E.G. Araujo, J. Schneider, K. Verbeken, G. Pasquarella, Y. Houbaert, Dimensional effects on magnetic properties of Fe–Si steels due to laser and mechanical cutting, *IEEE Transactions on Magnetics*, 46 (2010) 213-216.
- [187] M. Emura, F.J.G. Landgraf, W. Ross, J.R. Barreta, The influence of cutting technique on the magnetic properties of electrical steels, *Journal of Magnetism and Magnetic Materials*, 254–255 (2003) 358-360.